université PARIS-SACLAY

ONERA
THE FRENCH AEROSPACE LAB

ÉCOLE POLYTECHNIQUE
UNIVERSITÉ PARIS-SACLAY

PLAS@PAR
Plasmas à Paris

NNT : 2019SACLX013

Thèse de doctorat

# Electric contacts subject to high currents: Fundamental processes and application to the interaction between lightning and aeronautic structures

Thèse de doctorat de l'Université Paris-Saclay
préparée à l'Ecole Polytechnique

Ecole doctorale n°572 Ecole Doctorale Ondes et Matière (EDOM)
Spécialité de doctorat : Physique

Thèse présentée et soutenue à Palaiseau, le 15 Avril 2019, par

**JEAN-BAPTISTE LAYLY**

Composition du Jury :

| | |
|---|---|
| Jean Paillol<br>Professeur, CNRS (SIAME) | Président/Rapporteur |
| Philippe Testé<br>Chargé de recherche, CNRS (GEEPS) | Rapporteur |
| Fabien Tholin<br>Ingénieur de recherche, ONERA (FPA) | Examinateur |
| Laurent Chemartin<br>Ingénieur de recherche, SuperGrid Institute | Examinateur |
| Aurore Risacher<br>Ingénieur de recherche, IRT Saint-Exupéry | Examinateur |
| Anne Bourdon<br>Directeur de recherche, CNRS (LPP) | Directeur de thèse |

# Remerciements

Me voilà arrivé au moment le plus agréable de cette thèse, celui de remercier les personnes qui ont contribué à ce que j'arrive à déposer, un beau jour, la version finale de ce manuscrit. Cette occasion officielle de remercier celles et ceux qui m'ont aidé à traverser les moments difficiles , ou à apprécier les bons, m'a souvent donné l'envie de sauter directement à cette étape. Le plus délicat fût de me restreindre à effectuer un tri, afin de ne pas assommer le lecteur par une trop longue liste. De nombreuses personnes ont donc été omises, puisqu'il faut bien faire un choix, mais l'échantillon choisi est tout à fait représentatif de la chance que j'estime avoir eue jusqu'ici. Cette liste reste longue et suit par ailleurs un plan chronologique assez ennuyeux, quoique peu classique puisque l'encadrement ainsi que les membres du jury de thèse ne seront de fait mentionnés qu'à la toute fin. Le lecteur pourra se référer directement à la partie qui l'intéresse, la première correspondant aux vingt-cinq années précédant cette thèse, et la seconde à celles du doctorat.

Je remercie évidemment en premier lieu ma famille, dont je suis fier à bien des égards. Une famille de fortes têtes qui ne se comprennent pas toujours, mais qui ont des qualités exceptionnelles et des personnalités remarquables, dont j'essaie de prendre le meilleur. Mon père, ma mère, mes frères et ma sœur, je sais très bien ce que je dois à chacun d'entre-vous. Je n'ai jamais manqué ni d'amour, ni d'attention, ni d'exemple à suivre. Je remercie ma mère, pour les sacrifices que cela représente d'avoir élevé quatre enfants, pour avoir les pieds sur terre tout en cultivant une excentricité dont j'ai compris le caractère précieux en grandissant. Cela fait cliché, mais bien entendu pour ses bons plats aussi, car avoir découvert tard que ses pâtes n'étaient en fait jamais "al dente" ne remet pas tout en question. Je remercie mon père, pour avoir toujours pris le temps de m'apporter des réponses, sur tous les questionnements que je pouvais avoir, que j'ai encore souvent. Pour avoir toujours fait le maximum pour m'offrir le meilleur, quitte à se mettre en difficulté, et pour m'avoir montré un exemple de bonté et de ténacité. Je remercie mes frères et ma sœur, pour m'avoir accueilli en bon petit dernier, pour m'avoir apporté une enfance bien plus tranquille que la leur, sans jalousie. Jean-Louis, pour m'avoir fait découvrir la vie de haut en me portant sur ses épaules, pour m'avoir appris à lire mon premier mot, pour être le grand-frère solide. Florent, pour sa générosité, pour avoir toujours été un exemple montrant que douceur et virilité ne sont pas contradictoires, pour être rassurant.

Laure, pour son dynamisme, son amour et sa franchise, pour avoir été comme une seconde mère quand j'étais enfant, pour me jouer de la flûte le soir quand je ne dormais pas, et pour tellement d'autres petites choses. Tous les enfants n'ont pas la chance d'avoir un environnement aussi riche.

Je voudrais ensuite exprimer ma reconnaissance profonde envers le système scolaire, et envers toutes les personnes bienveillantes que j'ai rencontrées dans ce cadre depuis l'école maternelle. J'ai des souvenirs et des raisons de remercier quasiment chaque enseignant que j'ai eu, la plupart ayant été a minima de bons professeurs, d'autres des mentors malgré eux. Je dois en grande partie mon émancipation à toutes ces interactions et ces marques de respect. J'ai certainement été chanceux dans les établissements que j'ai fréquentés, dans la période où j'ai grandi, et ne peux qu'espérer qu'un maximum de jeunes des générations futures aient accès à des conditions aussi bonnes.

Le bien être et l'équilibre de ces années furent aussi alimentés par de belles amitiés, et je pense devoir énormément à ces quelques personnes sans qui il m'aurait manqué un point d'appui crucial à des moments où la personnalité se construit. Je pense à Vincent et sa famille qui m'ont "adopté" au primaire. À Hadrien, dont l'arrivée au collège a coïncidé avec la fin de ma période d'ado dans le doute et qui a été une amitié sans faille au lycée et par la suite. Aux camarades de prépa, avec qui la communion et l'émulation était si intense que je ne pourrais me contenter de ne citer que quelques noms. À ma tante Cathy et mon oncle Jean, qui ont toujours eu une présence rassurante et qui, à ce moment là en particulier, ont contribué à me procurer un environnement sain pour passer les concours. Aux membres de la famille Rousseau, qui m'ont très généreusement accueilli à Paris pour les oraux, puis plus tard lors de mon retour à la capitale, pour me lancer dans la thèse. Aux bons copains de l'école, Alex, Mickaël, Marc, Paul, Alexandre, avec qui j'ai partagé tant de joyeuses aventures, et qui ont représenté un socle autour duquel j'ai pu m'épanouir sans trop me perdre. À Nicolas, rencontré à cette même occasion, qui est sans doute la personne la plus intelligente et altruiste que je connaisse et dont l'amitié a été aussi précieuse qu'inattendue. À Pierre, qui a été un bon ami pendant les années de thèses, et qui m'a apporté un grand support moral et logistique. Sans l'aléa de ces rencontres, tout aurait pu être différent, qui sait.

Je remercie les personnes qui m'ont permis d'effectuer des stages intéressants, et dans des contextes scientifiques et humains épanouissants. Mes encadrants de stage, Lionel Chailan, Abdel Dehbi, Jean-Marc Martinez, qui ont été des modèles et m'ont inspiré pour la suite. Didier Vola, qui m'a grandement aidé à faire le lien entre ces stages. Je remercie chaudement les collègues qui m'ont accueilli pour le premier stage au LETR, une première expérience professionnelle qui fut un plaisir. Je remercie aussi toutes les personnes que j'ai connues pendant mon stage à ITER, et qui m'ont aidé à prendre de la hauteur sur un certain nombre de sujets.

I particularly thank the PSI group, my coworkers, and the guesthousers. I feel you

all deserve a special paragraph because I owe you the will to pursue a scientific career, meeting you at a time when I was a bit lost. This has been a wonderful experience, maybe still the best four months of my life, as you probably know. I've met there so many fun, interesting and open people from all countries that it has changed everything, and keeps giving me an ideal to pursue as a life and work environment.

During the months at PSI, I also met Chiara, whose kindness and dedication struck me. Thank you for sharing my life for the last five years, for being a balance that brings me calm and happiness, and for, most of the times, laughing at my jokes. I doubt I would even have considered doing a PhD if I didn't have this figure of heart and strength. Voglio anche ringraziare la tua famiglia, per essere così accogliente. Con loro e con gli amici di Montalbano, ho trovato un rifugio che mi ha salvato ogni volta che mi sembrava di impazzire Parigi. Ho scoperto com'è avere una grande famiglia che ancora si riunisce per ogni occasione, avere una nonna che ti fa ridere, e il piacere di parlare un po' in dialetto.

C'est grâce à toutes ces personnes si, arrivant à la fin de mon cursus d'ingénieur, j'ai eu envie de poursuivre un peu l'aventure en me lançant dans une thèse, malgré toutes les horreurs que l'on peut entendre sur le sujet (long, déprimant, inutile, voir professionnellement handicapant). Un peu par hasard, j'ai un jour appelé mon futur encadrant, Fabien Tholin pour obtenir des renseignements sur ce sujet intrigant. Sa pédagogie et ses connaissances m'ont immédiatement fasciné, comme elles n'ont cessé de le faire par la suite. Je remercie Plas@Par pour le cofinancement qui m'a permis de commencer en milieu d'année, et Fabien et Brigitte qui ont bataillé pour que que cela puisse se faire. J'ai immédiatement senti que j'étais bien tombé, et je remercie très chaleureusement toute l'équipe FPA pour m'avoir aussi bien accueilli. Je n'y ai rencontré que des gens passionnés et sérieux dans ce qu'ils faisaient, mais qui prenaient toujours le temps de discuter si le besoin s'en faisait sentir.

Merci à Philippe, pour ses mises en garde chaleureuses et clairvoyantes. À mes co-bureau François et Clément, qui ont aimablement subi mon humeur oscillante pendant les quelques mois compliqués de la thèse. À tous les autres membres de l'équipe FPA, doctorants et permanents, pour toutes leurs marques de sympathie et pour les nombreuses discussions intéressantes. À Julien, qui m'a souvent accueilli pour prendre un verre, et qui pouvait à tout moment reprendre sa casquette de physicien pour écouter mes problèmes de thésard et me glisser quelques conseils.

Je réitère mes remerciements envers Fabien, toujours disponible et à l'écoute. Je suis convaincu que je ne pouvais pas mieux tomber pour cet encadrement. Merci à Anne Bourdon qui a dirigé cette thèse, pour la fluidité de nos échanges, pour sa réactivité, pour sa présence rassurante. Enfin, réunir le jury de thèse pour la soutenance a été très facile, chacun ayant pris ses dispositions pour lire le manuscrit et faire le déplacement à la première date proposée. Je remercie les deux rapporteurs, Jean Paillol et Philippe Testé,

pour les rapports très détaillés, ainsi qu'Aurore Risacher et Laurent Chemartin pour leur lecture assidue et pour les remarques et questions pertinentes.

Pour résumer, je remercie tout ce beau monde pour le temps consacré à aider un jeune homme dans son évolution. Il est assez remarquable que des personnes qui courent après les heures pour répondre à toutes les sollicitations, qui se battent pour pouvoir avancer eux-même scientifiquement, fassent autant de place aux nouveaux venus.

Jean-Baptiste Layly

# Contents

# Introduction

Lightning is a natural hazardous event that strikes a civil aircraft once per 1500 hours of flight on average. The corresponding high and impulsive currents that may flow along the structure of the aircraft can generate physical constraints with major consequences regarding safety. In particular, when a fastened assembly is crossed by a lightning current, important electric fields and Joule power densities may give birth to a variety of discharge phenomena. These discharges are particularly critical in fuel tanks, and different lightning protection technologies and certification procedures are employed to face the sparking risk.

The technologies used to prevent or confine discharges in assemblies increase the weight, the operating cost and deteriorate the performances of an aircraft. There is therefore a need for reliable designs and prediction capabilities for further optimisation of protections.

The ignition mechanism for such discharges in assemblies is believed to be a consequence of the lightning current circulation through the interfaces between the different parts. These contacts induce an electric resistance, called *contact resistance*, that concentrates most of the voltage difference and Joule power in very small volumes. Moreover, it has been observed that at high current levels the contact resistances may vary on very short time-scales, which may have important consequences on the current distribution in the assemblies, and in the large scale aeronautic structures.

The physical reasons for the non-linearity of the contact resistances, and the related discharge phenomena that have been observed are still open questions that have gained a growing interest in the community of lightning strikes to aircraft. At Onera, unit FPA has a long experience on this subject, and the non-linear response of aeronautic assemblies to lightning strikes have been experimentally studied for years.

From a numerical point of view, unit FPA makes use of constant contact resistances in 3D finite volume models. However, taking into account their non-linear evolution and predicting the discharge ignition is a very complex challenge that requires studying into details the physics in the contacts at the microscopic scale. A relevant approach is then to derive a simple and fast non-linear contact model that could be used as an interface model in 3D simulations, and that could bring new insights into the dynamics of assemblies subject to lightning strikes conditions. The goal of this PhD project is to propose such a model. The challenging issues are the following:

- The micro-geometry of the contacts may be very complex, involving 3D fractal geometries and very different spatial scales.
- The physics of contacts under high current conditions involve very different and coupled physical phenomena, such as electrical, thermal and mechanical processes.
- The developed model has to be simple enough to be coupled with large scale simulations of assemblies or aeronautic structures.
- Occurrence of discharge phenomena should be addressed by the model with output parameters useful to define sparking thresholds in assemblies and evaluate the constraints induced by such discharge.
- The model should rely on available input data for contacts in assemblies. These data are limited and a model requiring for example an exact description of the surfaces' micro-geometry would be hardly usable for practical applications.

The modelling strategy relies on a simplified description of a contact micro-geometry, inspired by the numerous studies performed on contact resistances in the literature. Models that are used in other fields have to be extended and exceeded to the particular physics of high and transient lightning currents.

Chapter 1 is dedicated to a general overview of lightning and atmospheric electricity, before introducing briefly the context of lightning strikes to aircraft and lightning protection. The particular threat related to sparking in aeronautic assemblies is presented, and a discussion is conducted on the main experimental observations concerning electric contacts under lightning currents. A general overview about the electric contact science is presented, and the fundamental concept of "a-spot" is introduced. Then the particular physics taking place in contacts subject to high current values is discussed, and two different widely known processes are emphasized: the electro-migration, and the electronic emission.

Chapter 2 is dedicated to the numerical study of a single a-spot contact. 2D axisymmetric electrostatic simulations are performed, and a geometric simplification for a-spots is suggested. 2D thermo-electric simulations are then conducted to study into details the dynamics of an a-spot subject to lightning current values. Important patterns in the evolution of the a-spot, as the temperature increases and vaporization takes place, are reported. A simple 0D thermo-electric model that gathers the relevant pieces of information and turn them into hypotheses is proposed. This model is then compared with the 2D simulation results. Finally, the thermo-electric model is enriched with a mechanical model to take into account the tightening forces in a contact.

Chapter 3 deals with contacts with many a-spots: "multi-spot contacts". The interaction mechanisms between the different a-spots in a contact are emphasized. 3D

electrostatic simulations are performed to study the electrostatic coupling between the a-spots. Then electrodynamic and mechanical interactions are considered, and finally a simple interaction model is retained. An example of the physical complexity taking place in multi-spot contacts is illustrated considering a contact with two micro-peaks.

Chapter 4 raises the modelling of a realistic multi-spot contact. A Gaussian statistical model for a surface micro-geometry is presented, and the influence of a tightening force on the contact resistance is emphasized. Then, the dynamics of a realistic contact with a large number of a-spots subject to a D-wave current is considered. Two different cases are given attention: The case of a contact with constant tightening distance, and the case of a contact with constant tightening force. A parametric study is conducted for both cases to quantify the effect of the micro-geometry on the contact dynamics.

Chapter 5 addresses the modelling of the plasma discharges generated by the vaporization of a-spots in a contact. A simple plasma model is presented, that relies on a plasma expansion model in confined media, and a Quotidian Equation Of State (QEOS) with a conductivity model to compute the plasma properties. Then, the plasma model is used on a single a-pot contact with a constant confining pressure. The complex redistribution of the lightning current from the a-spot to the plasma during vaporization is examined, as well as the evolution of the plasma properties. Finally, plasma discharges in a constant confinement volume, representative of the internal gaps of an aeronautic assembly, have been considered. A parametric study is conducted on the initial contact resistance, and the final volume of vaporized metal, plasma energy, and plasma pressure are looked at.

# Chapter 1

# Overview of lightning strike to aircraft and sparking threat

In this chapter, we present a general overview of the processes leading to a lightning strike and its interaction with an aircraft. We then discuss the certification procedures related to lightning stroke that aircraft manufacturers have to comply with, concerning particularly the risk of sparking in fuel tanks areas. The key problematic of the dynamics of contact resistances in aeronautical assemblies under lightning stroke conditions is introduced. Finally, a state of the art is conducted on the electrical contact science as an introduction to the models and methods of this study.

## 1.1 Overview of lightning strike to aircraft

### 1.1.1 Lightning and atmospheric electricity

Clouds can be considered as deviations from the normal conditions of the classical stratification of the atmosphere regarding the properties of the air, such as temperature, pressure and humidity. In the classical atmosphere model, the standard conditions define these time-averaged properties as functions of the altitude. The gradients observed are a consequence of the long term sources that are basically gravity, the radiation received from the sun and geothermal activity. Local events such as cloud formation are more or less violent consequences of perturbations of this equilibrium.

For instance a *cumulonimbus* cloud, the most common form of thunderclouds, can be formed when a sufficiently warm and moist parcel of air happens to encounter a cold and dry mass of air. Due to the buoyancy forces, the hot air rises-up and brings the water vapour in altitude into colder and colder regions. When the temperature is sufficiently small, the condensation of the vapor releases the latent heat of vaporisation of the water into the air, heating up and accelerating even more the ascending wind [1]. This tremendous energy release of several GW is the main source of energy in such a cloud

and causes very important gust of wind and turbulences [2]. As the humid air continues to rise, the decreasing air temperature may reach the freezing point of water and droplets may develop into ice crystals. Simply put, the smallest ones may be light enough to be convected upward by the ascending wind, while the largest ones may be too heavy and start to fall down, resulting in precipitations (rain or hail). As a consequence, numerous collisions between the so-called hydrometeors take place into the cloud, leading to charge exchange and charging [3].

At first order, due to this complex collisional and charging dynamics, heavy hydro-meteors (for example hailstones) acquire on average a negative charge, mainly located at the bottom of the cloud, while light hydro-meteors (for example small ice crystals) convected upward acquire on average a positive charge. Then, part of the energy released by the condensation of vapour into the cloud is converted into electrostatic energy through charge separation due to collisions and gravity. The formation of different charge pools and an important electric-field of the ordre $10^5\,\mathrm{V\,m^{-1}}$ inside the cloud may appear a few tens of minutes after the beginning of the precipitations [4]. From an electrostatic point of view, the resulting polarization of the cumulonimbus cloud can be approximated by an electric dipole, or a large loaded capacitor, with a total charge of around 100 C, a maximum voltage of the order 100 MV and arround $10^{10}$ J of electrostatic energy [5]. In this context, natural lightnings are the discharge phenomena taking place in the atmosphere to unload the capacitor formed by the cloud, and recombine the electric charges .

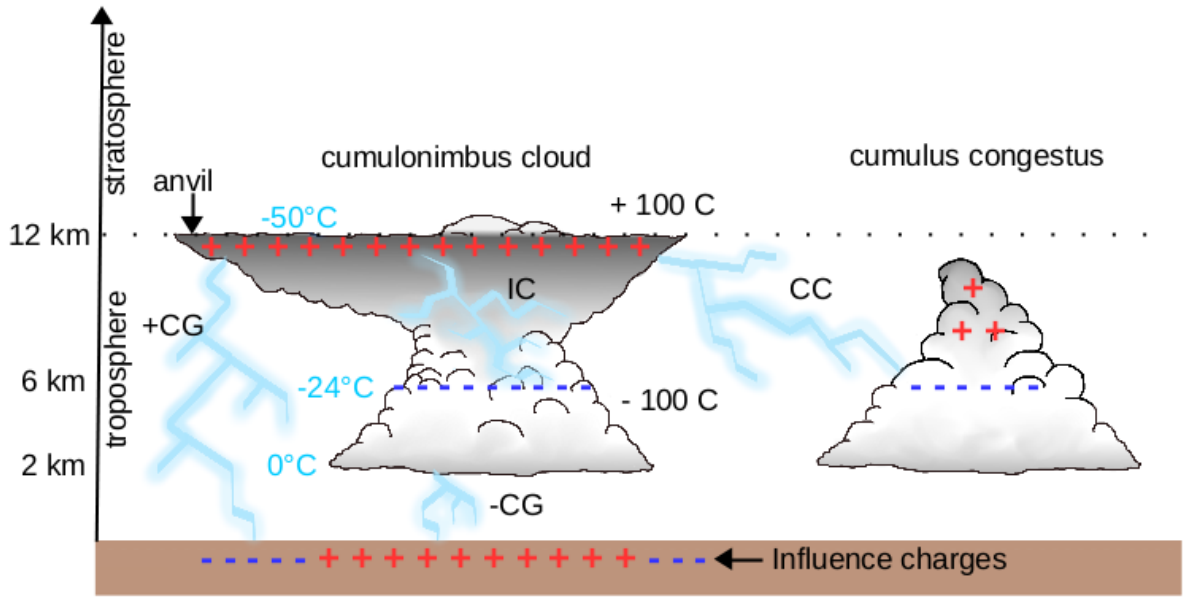


Figure 1.1: Illustration of four types of lightning flashes.

Most common flashes occur between two charge pools of a single cloud, and are called

*intra-cloud lightnings (IC)*, as represented on Figure 1.1. As the electric field of a cumulonimbus can extend in the atmosphere far from the cloud, flashes may happen between two different clouds, and are in that case designated by *inter-cloud lightnings (CC)*.

An important consequence of the polarization of the cloud is a positive electrostatic induction of the underlying ground close to the base, and a negative electrostatic induction of the ground under the anvil (see Figure 1.1). As a consequence, *cloud-to-ground lightnings (CG)* may ignite, that are classified in two categories regarding the polarity of the transported charges. Around 90 % of them come from negatively charged regions of the base of the cloud and are called *negative cloud-to-ground lightnings (-CG)*. The remaining 10 % are called *positive cloud-to-ground lightnings (+CG)*.

As there are more negative cloud-to-ground lightnings than positive ones, the overall current conservation means other current flow occur elsewhere. Interestingly, thunderclouds are part of the so-called “global electric circuit" [6]: as there is electric induction with the ground, there is also electric induction between the positively charged anvil and the upper ionosphere, at more than 100 km of altitude, as represented on Figure 1.2. This high altitude electric field benefit from the low air density to give birth to a wide variety of discharges above the clouds, like elves, sprites, blue jets, and upward superbolts [7], that generate a net current of about 1 A from a typical thundercloud to the ionosphere. Because there are always on average 1000 cumulonimbus on Earth, a current of around 1 kA is flowing in the ionosphere, which potential may reach 300 kV. The global circuit is then closed by the very small current density ($\simeq 10^{-12}\,\mathrm{A\,m^{-2}}$) flowing from the ionosphere to the ground, thanks to the “fair-weather electric-field" ($\simeq 120\,\mathrm{V\,m^{-1}}$), which is present everywhere on the globe far away from thunderstorms [8].

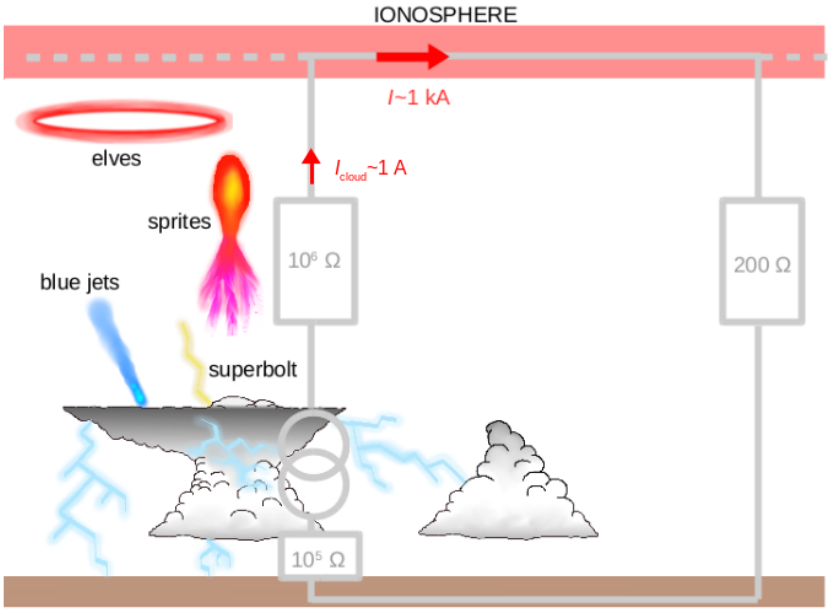


Figure 1.2: Illustration of four types of lightning flashes.

The electric-field of a cumulonimbus cloud is much smaller than the typical breakdown field of air at atmospheric pressure ($\simeq 3.6\,\mathrm{MV\,m^{-1}}$). Even considering the decreasing breakdown field due to altitude and decreasing air density, or due to the presence of precipitations, the breakdown field scaled to the sea level is always higher than $4 \times 10^5\,\mathrm{V\,m^{-1}}$ [9]. For this simple reason, as mentioned by the author of [10], the initiation mechanism of lightning is still an open question, puzzling the community for more than half a century.

Briefly put, there are essentially two theories being discussed. In both theories, lightning always starts with a propagating leader phase, growing from a branching streamer discharge, itself ignited in a place of strong electric-field enhancement, where it could locally exceed the breakdown threshold.

In the first theory, the field enhancement is provided by hydro-meteors, such as water droplets or ice crystals, whose electric conductivity or dielectric properties allow for a large point effect and field enhancement.

The second theory relies on a conductive plasma volume created in the air by the so-called runaway breakdown mechanism. This type of breakdown may appear far below the breakdown field, due to a shower of runaway electrons provided by an energetic cosmic ray. Then, the core of this plasma would have enough conductivity and life-time before recombination to enhance the electric field and ignite a streamer discharge [11][12].

Recently, hybrid scenario have been considered [10], but a consensual point is that ignition of natural lightning always need a local enhancement of the field, so that ionization can take place giving birth to a plasma seed.

Once the plasma is ignited in the high-field region, streamer discharges may start to propagate, following the mechanism described on Figure 1.3: The initial plasma region acts as a conductor that locally enhances the electric field. This field induces a drift motion of the ions and the electrons in the plasma in opposite directions, resulting in the plasma polarization. While the field is screened inside the conductive plasma, it is strongly enhanced at the plasma-air interfaces due to the space-charge and point-effect. Then ionization takes place where the field is above the breakdown field of air $E_{\mathrm{br}}$. A new plasma is created, and due to drift fluxes the high field region is propagated further again.

Such streamer discharges are not able to propagate very far from the high field regions close to the droplet, due to the plasma recombination in the channel. For a lightning to trigger, complex electro-thermal phenomena in the plasma, such as thermal ionization mechanisms, have to take place in order to maintain a high enough conductivity in the plasma despite the low electric-field, and sustain an important potential in the discharge's head to propagate. The appearance of a thermal-ionization regime makes it possible for the discharge to propagate on very long distances of km size, and is representative of a streamer-to-leader transition. Then the first step of a lightning discharge is associated

with the propagation of a positive leader, in the direction of the thundercloud electric field to a negatively charged region, and also of a negative leader, propagating in the opposite direction, towards a positively charged region. Such a situation is represented on Figure 1.4 in the case of a cloud-to-ground lightning.

The bi-directional propagation speed is estimated to approximately $10^5\,\mathrm{m\,s^{-1}}$ for both negative and positive leaders [13], and consists in a step by step displacement, due to the complex thermalization and chemical evolution of the plasma channel [14]. The leader phase lasts a few milliseconds, and the step by step propagation induces a sequence of pulses between 1 and 10 kA at several kHz.

When the negative leader reaches the ground, it has left a conductive channel between the cloud and the ground. Then a fast redistribution of the field and charge displacement from the ground to the cloud takes place, known as the first *return stroke*. During this phase, usually the most visible of a lightning flash,the current may reach several thousands of amperes within a few microseconds. The temperature inside the plasma channel may typically reach 30 000 K for a current of 100 kA, even if far more extreme but rare scenario have been accounted for in the litterature, with current values up to 500 kA [15], and temperatures of a few hundred of thousands of Kelvin [16].

The return stroke is generally followed by a more stable current, known as *continuous phase*, with a current in the order of a few hundreds of amperes but a duration of hundreds of milliseconds. Several other re-stroke with short and high pulsed current phases may occur during, and even after this continuous phase [17].

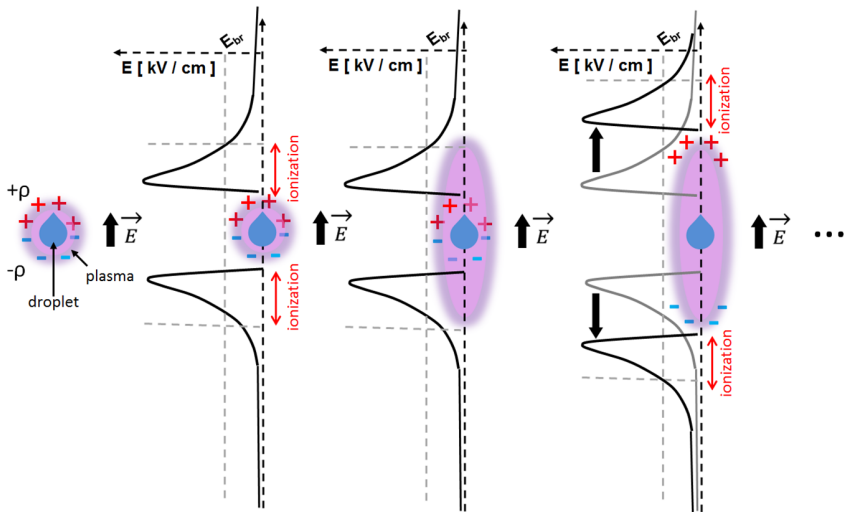


Figure 1.3: Ignition of a positive and a negative streamer from the enhanced field regions around a droplet.

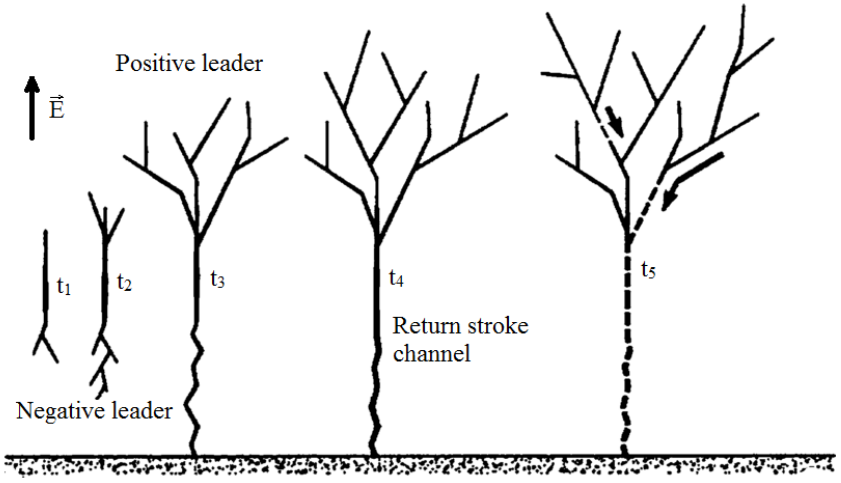


Figure 1.4: Development of a bi-directional, bi-polar lightning 'tree' made of positive leaders above and negative leaders below for a negative ground lightning (taken from [18]). The different instants $t_i$ illustrate the progression of the leaders.

### 1.1.2 Development of a lightning strike to aircraft

In the following study, the usual denomination of *lightning strike* will refer to a lightning flash that involves an object on the ground or in the atmosphere [17], such as an aircraft. Naturally, lightning strikes are mostly due to *CG* flashes for the case of ground infrastructures, but also in the field of aeronautics. Indeed, aircraft are mostly struck by lightning during the take-off and landing phases, because cruising aircraft can usually choose their path to avoid crossing dangerous thunderclouds. Therefore, even if *IC* flashes are the most observed in the atmosphere, *-CG* is the predominant type of flashes of interest regarding aircraft protection.

The average probability of a civil aircraft to be struck lies between once per 1000 or 10 000 hours of flight [19] [20]. This frequency depends on different parameters such as the local climate, the type of aircraft and the flight routine. One could think of such event to be the hazardous result of the interception of a lighting flash by the course of a plane, but this scenario only represents 10 % of lightning strikes to aircraft. Most of the time, it is the presence of the aircraft that triggers a lightning flash. As for natural lightning discharges, triggered lightning development involves at the beginning the formation of a small plasma around a sharp part, that geometrically increases the background electric-field to values higher than the breakdown threshold. In this case, the field enhancement is not provided by a small hydrometeor, but for example by the sharp winglets, noze or tail of an airliner as shown on Figure 1.5, showing a numerical simulation of the electric field around an aircraft [21].

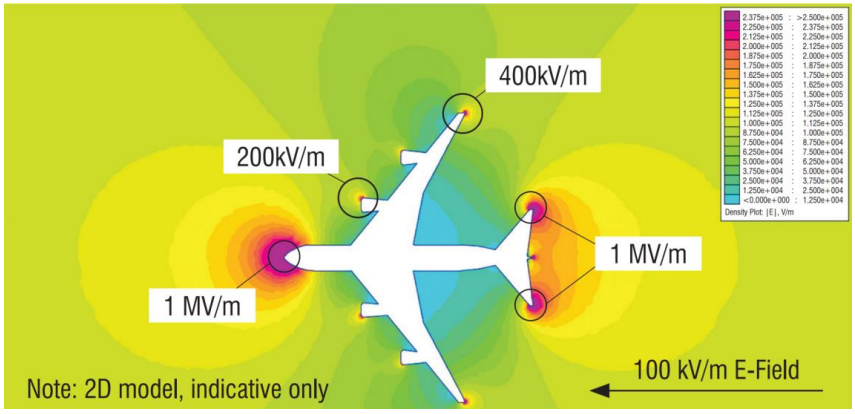


Figure 1.5: Indicative 2D electrostatic model of an aircraft in a 100 kV m$^{-1}$ ambient field calculated by Morgan et al. [21].

Figure 1.6 shows the two different processes of aircraft lightning initiation. In both cases (intercepted and triggered lightning), a positive leader develops from the aircraft which becomes negatively charged. A consequence is the development, a few millisecond later, of a negative leader propagating in the opposite direction. In the case of an intercepted lightning, the positive leader connects with the *-CG* leader, whereas the aircraft leaders propagate in opposite direction until the path connects the cloud to the ground. The result is that the aircraft is part of the lightning current path: The lightning current therefore crosses the aircraft from an entry point to an exit point, that are called “attachment points".

Since the speed of the aircraft is of the order of 100 m s$^{-1}$ and the lightning flash duration is of the order of 100 µs, the aircraft can move about 10 m or more during the strike. The arc attachment points are then likely to be swept backwards along the vehicle, since the lightning channel tends to remain stationary relative to the surrounding air. [22]. This motion of the lightning attachment point, known as the *swept stroke* phenomenon, is illustrated on Figure 1.7.

Figure 1.8 shows the typical current waveform of a lightning stroke to an aircraft, that could be obtained during in-flight measurements. The first bursts observed are characteristic of the leader step by step propagation. Then, first and subsequent return stroke up to 200 kA may occur, that are characteristic of the pulsed arc phases of a lightning stroke. The continuing current phase is clearly visible, with a much lower current intensity but a much larger duration.

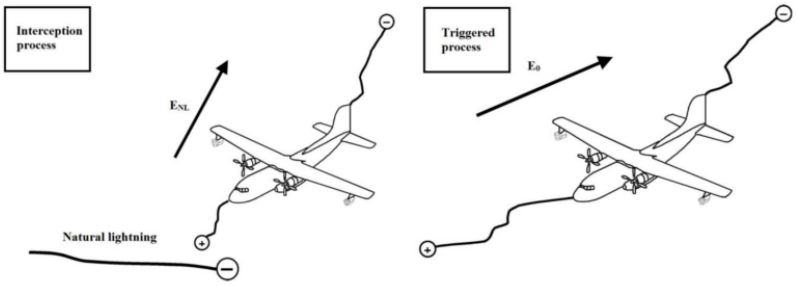


Figure 1.6: The two different processes that lead to a lightning strike to an aircraft through a bi-directional leader process. (a) The interception by the aircraft of a natural lightning discharge. (b) The aircraft itself triggers the lightning discharge. Taken from [23].

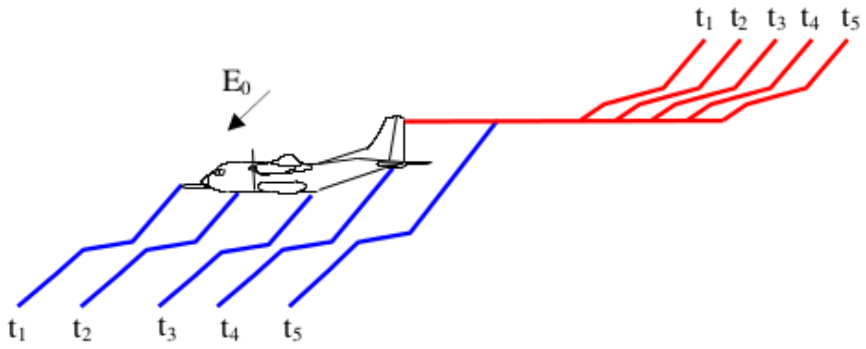


Figure 1.7: Illustration of the swept stroke process: The swept is represented in the frame of reference of the aircraft for different times $t^i$. Taken from [24].

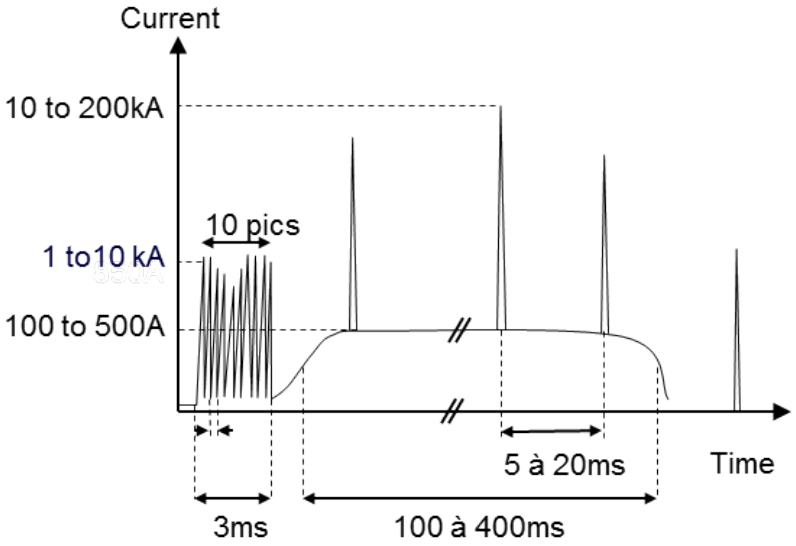


Figure 1.8: Typicall lightning current waveform that can be obtained from in-flight measurements. Taken from [25].

### 1.1.3 Effects of lightning strikes to aircraft

Once the lightning arc is initiated, the electric current may flow in the conducting parts of the aircraft, on its external surface, referred to as the “skin" of the aircraft in the following, but also in the inner parts, in order to connect the entry and exit attachment points. Then the damaging effects of lightning strikes to aircraft are sorted in two categories:

- *Indirect effects* are those resulting from the interaction between the electromagnetic field, generated by the strong and impulsive currents illustrated on Figure 1.8, and the electrical devices in the aircraft.
- *Direct effects* refer to the physical damage caused to structures and external devices by the lightning arc attachment to the fuselage. Such damage may be the consequence of three kind of physical constraints: themal, mechanical, and electric constraints.

Thermal constraints result from two distinct mechanisms: Joule effect, that induces a volumetric heating in every place where the lightning current may flow, and thermal fluxes from the hot air plasma to the materials at the attachment points of the lightning arc. Joule effect can lead to important thermal damage deep in the core of the materials, and is responsible for the explosive vaporization of thin conductors, such as the lightning protections made of a thin metallic layer or fabric at the top of the aeronautic skins (Alu-mesh, Copper-foil). At the attachment points, the Joule power is maximum due to the high current density, and cumulates with the thermal fluxes from the plasma. The main contributions to the total thermal fluxes are the radiative transfers between the hot air plasma and the materials, the thermal conduction due to the important thermal gradients, and last but not least the energy fluxe due the surface recombination of ions from the plasma on the materials at the cathodic attachment point.

The mechanical constraints are also maximum close to the arc root, due to the volume Laplace forces, the high pressure in the plasma and the shock-wave during the pulsed arc phase. Far from the arc root, only the Laplace forces remain but the fast decrease of the current density and the magnetic field with current diffusion in the structure strongly mitigates this effect with distance.

Electric constraints are related to the possible electrical breakdown of materials subject to important electric-fields due to the lightning current circulation. It may be the case for example between the different plies in a stratified composite material. The high electric-fields that may appear in assemblies may also give birth to plasma discharges. An example are the so-called “edge-glow" discharges that may appear on the edge of composite materials [26]. In this PhD project, a particular attention is given to the possibility of electrical breakdown in the air when the lightning current crosses a mechanical contact between several structural parts.

All these constraints may cumulate with each other, resulting in complex damage that may be difficult to predict, prevent or even detect. Figure 1.9 shows an example of damage on the radom of an aircraft due to a lightning arc attachment.

Figure 1.9: Effect of the swept stroke displacement of a lightning arc attachment on the radom of an RNZAF Orion. Taken from [27].

### 1.1.4 Sparking risk

The consequences of the passing of the lightning current would be minimal if the structure of the aircraft was perfectly conductive. The amount of heat dissipated by Joule effect and the electric-fields generated are all the more important as the materials are resistive. The aluminium, that has been widely used in aeronautic construction for its specific mechanical properties, happens to be a good material regarding the sustainability to lightning strikes. A drawback of the increasing use of composite materials is that, although they have better mechanical properties than aluminium, their anisotropic and much lower conductivity values represent a new challenge regarding direct effects and lightning protection.

Besides, even when the aluminium is predominant in the structure, an aircraft is not a single-body conductor but rather an assembly of pieces, and all the mechanical interfaces connecting the different parts induce electrical resistances the lightning current may have to cross. These resistances, referred to as “contact resistance" in the following, induce high voltage drops on short distances, high electric fields, and important Joule power densities that may ignite different discharge phenomena. Some of the most constraining contact resistances in aeronautic structures are related to the fastened assemblies between the skin of the aircraft, where the lightning current is expected to flow, and the underlying structural parts such as spars or ribs on a wing. In those fastened assemblies, the parts are joined together with a large variety of fasteners, made most of the time of a screw, a nut, and possible nut-locking technologies, washers and rivets. The Figure 1.10 shows an

example of a typical fastened assembly between the skin of the aircraft and a rib.

The different discharges that have been observed on such assemblies in the lightning stroke community are represented: The edge-glow discharge on the edge of the composite rib, but also the spark discharge and the outgasing phenomena that may take place on the bottom part of the assembly, close to the nut. Spark discharges and outgasing phenomena are highly related to the electric-field and the Joule effect in the contacts between the screw, the nut, the skin and the rib. On Figure 1.10 the current injection in the assembly is a consequence of the current flowing in the skin. The arc root may in this case be quite far from the fastener, meaning that those discharge could appear almost anywhere in the aircraft structure. This current injection situation is called “conduction" in the community, while the opposite situation, when the arc root is directly attached to the head of the screw is called “attachment", as represented on Figure 1.11.

An example of the electric field distribution in an fastened assembly for an attachment case is represented on Figure 1.12: It is a sliced view of the electric-field computed in an 3D geometry with *Code_Saturne*, the EDF CFD (Computational Fluid Dynamics) software [28]. It can be clearly seen that the field is maximum in the air in the vicinity of all the interfaces between the different parts, where contact resistances have been manually added. The high field regions may lead to sparking discharges at the bottom of the fastener, as shown by the close view.

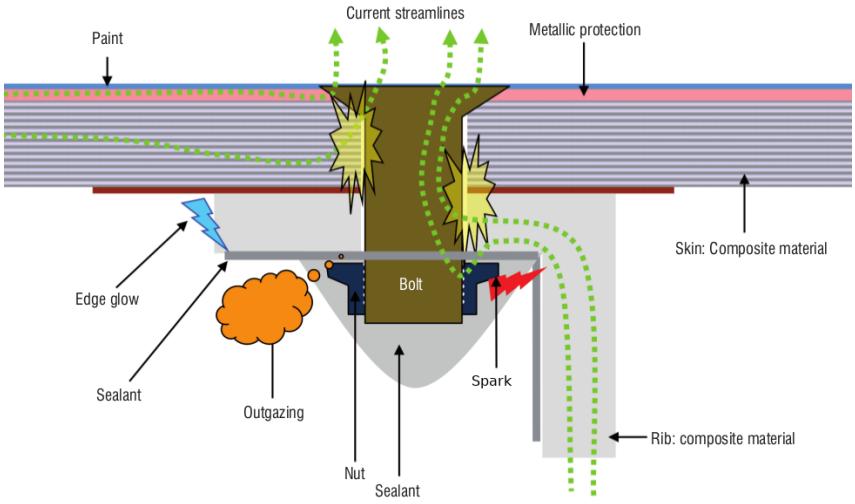


Figure 1.10: Schematic drawing of the different mechanisms that occur during sparking phenomenon. Taken from [29].

For obvious reasons, it is crucial to avoid the occurrence of such sparking or outgasing discharges if the bottom part of a fastener is located in a fuel tank. Discharges in fuel tanks would not necessarily lead to disastrous aftermaths, because the medium must be in the right conditions of pressure and air supply to ignite. To insure maximal security,

aircraft manufacturers look for fastener designs and certification processes that limit this discharge risk as much as possible.

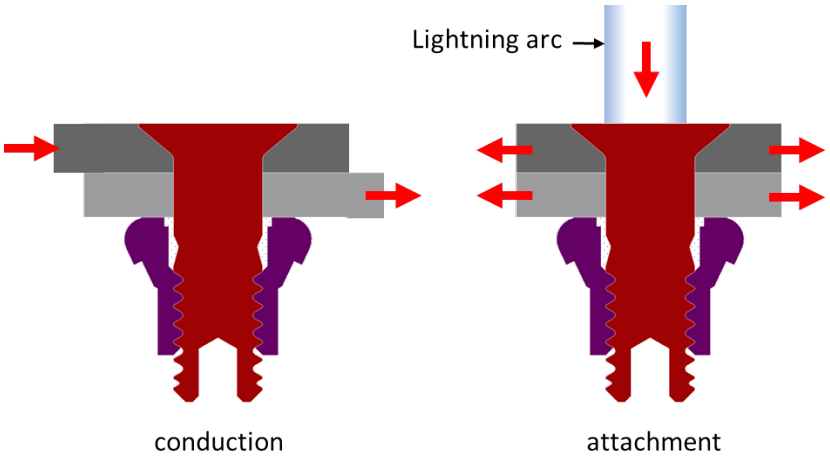


Figure 1.11: Sparking in aeronautic fastened assemblies may result from two distinct situations regarding current injection: “conduction" and “attachment".

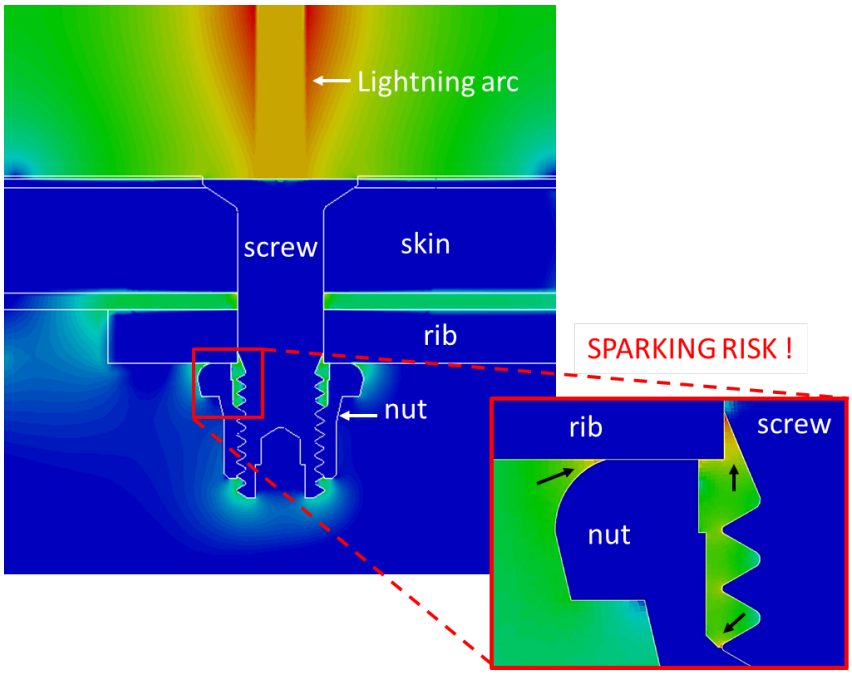


Figure 1.12: Sliced view of the 3D electric-field (arbitrary unit) distribution in a fastener in an attachment situation. The black arrows show the regions where the electric-field is the highest, here at the interfaces between rib, nut and screw.

## 1.2 Aircraft protection

Lightning strikes on aircraft are random but potentially dangerous. They occur on average once a year on a civil aircraft, usually with minimal consequences. However aircraft constructors have the responsability to protect them against the worst cases scenarii. To cover the widest range of reasonable cases, committees such as EUROCAE (European Organization for Civil Aviation Equipment) and SAE (Society of Automotive Engineers), establish normative conditions that materials must be able to sustain ([30]).

### 1.2.1 Normalized waves and aircraft zoning

Not all surfaces of an aircraft need to be designed to survive the same lightning threat. Indeed the lightning flash usually initiates on sharp areas, and is then swept backwards (cf Figure 1.7. ), towards areas that are in the path of the sweeping channel. Only some areas, at the rear of the aircraft, may receive the full energy of a flash, because the lightning arc can hang-on to them for the total flash duration. On the other hand, other areas will only experience a fraction of a lightning flash.

The proportion of the flash endured by any particular point therefore depends on the probability of initial attachment, sweeping and hanging on the skin of the aircraft. In order to optimize lightning protection and set the basis of systematic certification processes, standardized lightning current waveforms are defined together with lightning strike zones.

The lightning current waveforms are defined by a composition of current components. These standardized components are not intended to replicate specific lightning events, but are rather meant to correspond to upper bounds regarding the effects of lightning on aircraft. The main relevant parameters of a lightning strike regarding direct or indirect effects are the peak current amplitude, the action integral and the time duration. Standardized components are defined by combinations of extreme cases of these characteristics that may be observed on aircraft. Figure 1.13 illustrates four components of the current waveform with their corresponding maximum current level (kA), time duration (ms), action integral ($A^2 s$) and transferred charge (C).

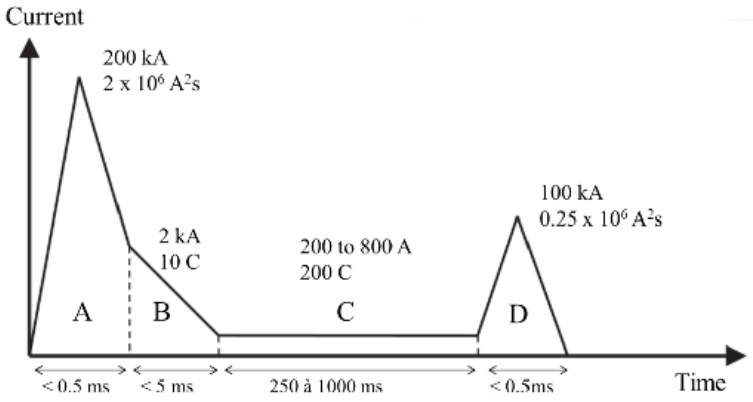


Figure 1.13: Ideal lightning current waveform. Taken from [22].

Although meant as extreme boundaries, each component is representative of one of the phases of a lightning strike presented in section 1.1.1. The A-component relates to the first return stroke, and the D-component reproduces the subsequent strokes. The B-component is associated to the transition from the impulsive stroke currents to the continuing current, which is represented by the C-component. The different characteristics of the components may have diverse effects on the aircraft. For example a component with a great action integral would correspond to great thermal effects due to Joule heating in resistive materials, whereas impulsive components will lead to important electromagnetic effects.

The time of attachment of the lightning arc on a single point, refered to as “dwell-time", may range from 1 to 50 ms if the channel can be swept backward [22]. Dwell times of 1 to 5 ms are typical of lightning attachments to unpainted metal surfaces. Even such short attachment durations are sufficient to experience full impulsive A or D components, as well as the continuity component B. Dwell times on surfaces covered with especially thick or high dielectric strength coatings may rather range from 20 to 50 ms, durations that allows to experience AB or DB, followed by a small fraction of a C-component. In any case, if sweeping takes place the arc cannot stay attached long enough for a single point to endure a full C-component. The denomination C* is then used for a shorter C-component associated to the a longest possible dwell-time. Only some areas at the rear of the aicraft may hang-on long enough to endure several impulsive components or a complete C-component. From these considerations, the SAE devided an aircraft in several zones that may endure similar sequences of wave components [31]. An example of such lightning zoning applied to a civil aircraft is represented on Figure 1.14.

The zones are defined with two labels (a number and a letter). The first label indicates the cause of the presence of the arc: attachment (zone 1), sweeping (zone 2), or neither of them (zone 3). Areas of Zone 1 are the only ones that can endure an A-component, representative of a first return stroke. Zone 2 may endure all other components. Zone

3 is considered protected from the lightning attachment, because these areas are neither initiating a lightning flash nor in the path of a sweeping arc ignited in a Zone 1 area. They may however endure conductive currents going from the entry point to the exit point, but these currents should be much lower due to current diffusion in the structure. The second label is associated to three letters (A, B and C) to describe the ability of the arc to sweep (zone A) or to dwell at the same location (B). The association of the two labels defines specific zones and the waveform components they should be able to endure:

**Zone 1A :** First Return Stroke Zone: ABC*-components.

**Zone 1B :** First Return Stroke Zone with Long Hang-On: ABCD-components.

**Zone 1C :** Transition Zone for First Return Stroke: AhBC*-components (Ah-component is a reduced A-component).

**Zone 2A :** Swept Stroke Zone: DBC* component.

**Zone 2B :** Swept Stroke Zone with Long Hang-On: DBC-components.

**Zone 3 :** Current Conduction Zone: Any attachment of the lightning channel is unlikely, but those portions may conduct a substantial amount of electrical current between the attachment points.

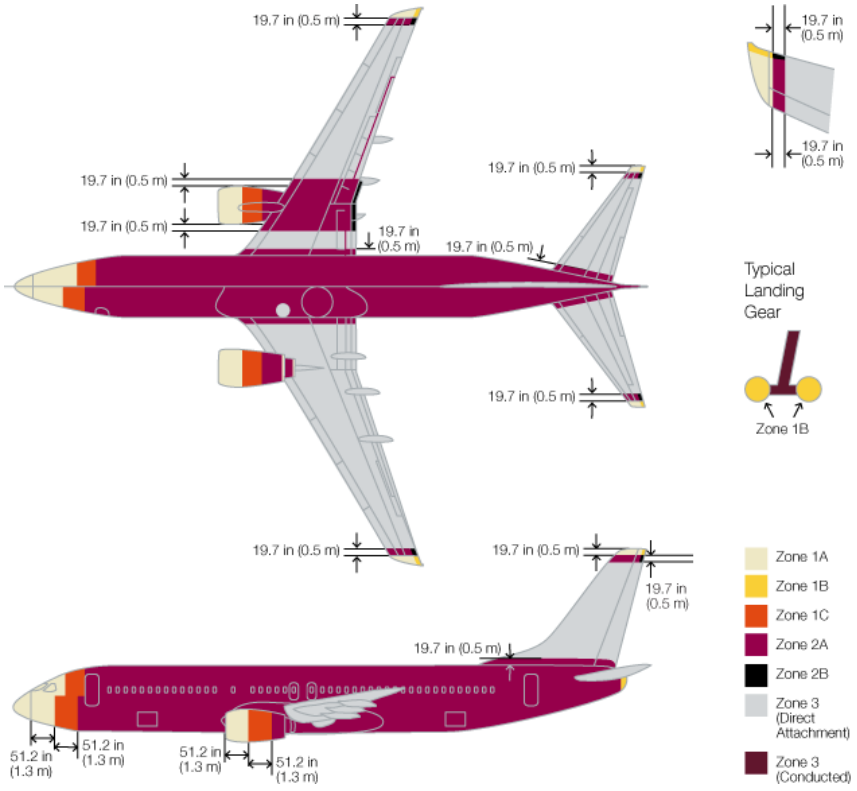


Figure 1.14: Example of lightning zoning applied to a Boeing airliner. Taken from [32].

The normalized waves represented on Figure 1.13 together with the zoning of aircraft give a baseline of currents that aeronautical structures should be able to sustain. The certification of aircraft impose to prove that materials and assemblies of each zone have an accceptable behavior when crossed by the corresponding normalized wave components [33]. For that purpose, large testing facilities that can generate artificial discharges on structures and samples, with imposed normative current waveforms, may be used. For instance, in Toulouse the DGA-TA (DGA-Techniques Aéronautiques) center has, at manufacturers disposal, the Super-Dicom and the Emma benches that can deliver normative current waveforms and intensities up to 300 kA on large aeronautic structures or models.

For each zone, experimental tests may reveal the necessity to add lightning protections in some particular places. Lightning protections cover a wide range of technological solutions. As mentioned previously, some thin conductors like mesh or foils may be added on the surface of the skin of the aircraft, most of the time under the paint layer, to prevent damage on materials and the diffusion of the current in the underlying structures. In the context of discharges in fastened assemblies, an efficient protection is to add a lot of sealant around each contact to prevent electrical breakdown or outgasing phenomena. An other technology makes use of a metallic or dielectric nut-cap around the nut to confine the potential discharges and prevent their propagation in fuel tanks for example. However, all these lightning protections increase the cost, the weight, the maintenance and the possible source of failure of aircraft. To design efficient protections, or avoid them, it is then necessary to have a better understanding of the lightning direct effects. Among them, the interaction of a lightning arc with materials and the ignition of plasma discharges in assemblies may be the most difficult issues. For this reason, experimental and numerical studies are conducted in the community to improve the understanding on direct effects. This PhD project is part of this thematics, in the continuity of many studies performed at Onera in unit FPA.

### 1.2.2 Experimental and numerical studies at Onera

At Onera, unit FPA has developed a small research capacitive bench, GRIFON (*Générateur de Recherche sur l'Impact du Foudroiement de l'ONera*), to study into details the fundamental processes in aeronautic structures subject to lightning stroke, using state of the art diagnostics. For instance, GRIFON can generate a 10 cm long plasma arc with a D-wave current [34] on sample materials or assemblies that are placed in between the two electrodes.

In particular, as part of the fundamental studies on the sparking risk in fastened assemblies, Figure 1.15 shows an aeronautical assembly that has been tested on GRIFON in a conduction configuration. An important discharge can be observed on the right part of Figure 1.15, as well as the voltage probes that are used to measure the contact

resistance between the head of a screw and the composite skin.

One of the most important observation performed during such experimental studies is that the contact resistance may vary significantly, on microsecond time-scales, during the wave. Figure 1.16 shows an example of the variation of the contact resistance obtained on a composite-metal contact subject to a D-wave current. These fast and non-linear variations of the contact resistance by orders of magnitude are difficult to measure due to the very short time-scales. However, the variation of the contact resistance is a reliable and reproducible result that can also be obtained on metal-metal contacts in assemblies. They also appear to be directly related to the possible occurrence of sparking and outgasing phenomena.

From a numerical point of view, unit FPA have been using 3D finite volume simulations to solve the current distribution, the electric field, and the temperature evolution due to Joule heating in assemblies. However, the contact resistances are assumed constant in those simulations, which is a strong limitation given the experimental observations. Moreover, it is very difficult to derive a reliable criteria that could detect the conditions favourable to the ignition of a discharge. Then, there is a need for a variable contact resistance model that is fast enough to be coupled as an interface model with 3D finite volume simulations, an that could help predicting the ignition of discharges. One of the main goal of this PhD project is to study into details the physical processes that may lead to the resistance variations in metal-metal contacts and the occurrence of plasma discharges.

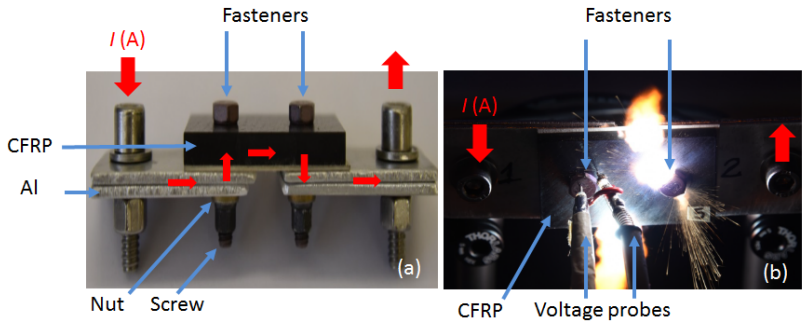


Figure 1.15: (a) Side view of the fastened assembly under test: The current (red arrows) flows from the aluminium skin to the multilayer CFRP (Carbon Fibre Reinforced Polymer), going through the nuts and the screws. (b) Top view of the experimental setup: voltage probes are used to measure the evolution of the contact resistance between the screw and the CFRP. Courtesy of Rafael Sousa Martins.

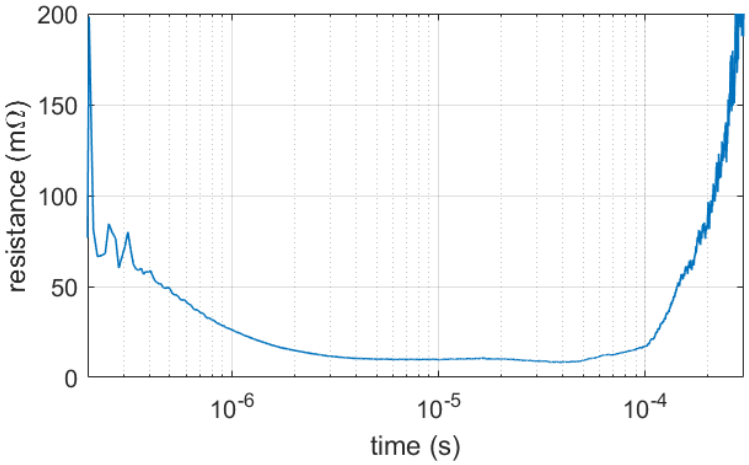


Figure 1.16: Evolution of a contact resistance measured thanks to the voltage probes of Figure 1.15(b). Courtesy of Rafael Sousa Martins.

## 1.3 Overview of contact resistance theories

### 1.3.1 Brief history on electrical contacts science

The electrical contacts have been a critical matter since the early stages of the development of electricity and electrical circuits, but were not necessarily well understood or well investigated. Initially, the range of currents carried by electrical contacts was limited, from some fractions of an ampere to perhaps of few hundreds of amperes. The range of currents involved has greatly increased with new technologies, going from micro-amperes in micro-electronics technologies up to mega-amperes in high power devices and switches. With the improvements of measuring tools and with the development of new solid matter theories came better knowledge on electrical contacts. Since the 1940s, a considerable amount of knowledge has been accumulated in electrical contact science. In 1952, the ASTM (American Society for Testing Materials) published the bibliography and abstracts on electrical contacts from 1835 to 1951 [35], and continued to do so until 1965. The recording of abstracts regarding electrical contacts was then continued by the Holm Conference Organization until nowadays [36]. However, only a few comprehensive books have been written on the subject. In 1940, Windred published *Electrical Contacts* [37], that treated the subject into details. Ragnar Holm published his first book in 1941, in German, and continued to update his work until the publication of the widely cited book *Electric Contacts: Theory and Application* in 1967 [38], reprinted several times until 2000. A more recent book, *Electrical Contacts: Principles and Applications* [39], the fruit of the collaboration of many authors and edited by Paul G. Slade, is a very helpful tool to understand a broad variety of aspects regarding contact resistances.

### 1.3.2 Definitions and terminology

The contact resistance between two conducting surfaces is very well introduced by Holm [38]. The term *electric contact* refers to the junction, mechanically tightenable or releasable, between two conductors, when this junction can carry an electric current from one conductor to the other.

Experimentally, a resistance between two points can be measured by placing probes in contact with these points, imposing a small current to go from one probe to the other, and measuring the voltage drop between the probes. The resistance is then defined by the ratio between the voltage drop and the current. The use of small continuous currents insure the linearity of electrical conduction laws, such that this ratio is independent on the current level. In the case of a single body conductor of constant section such as a cylinder, the resistance experimentally measured is proportional to the distance between the probes.

However when the current has to go through an interface, an additional component

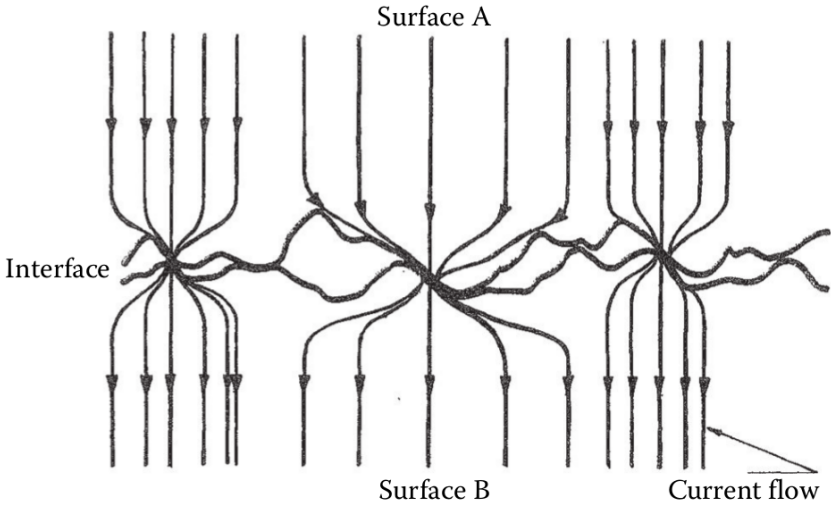


Figure 1.17: Schematic diagram of a bulk electrical interfac. Taken from [39].

of the resistance is measured, and it is observed that the biggest voltage gradients in a contact are situated at the close vicinity of the interface between the contact members. This additional resistance is not completely independent on the distance between the probes, but converges to a fixed value as the distance is increased and border effects can be neglected. This value is naturally called *contact resistance*, and can be seen as the extra resistance only imputable to the interface between the contact members.

Indeed, such interface represents an obstacle to a current passing from a conductor to the other, even if the conductors are made of the same material. The main reason for this contact resistance lies in the fact that the conductors' surfaces are by nature highly irregular at small scales, in general at the order of the micrometer, and the real contact area is only a small fraction of the apparent surface. Therefore the current has to go through the micro-peaks of the two mating surfaces as illustrated in Figure 1.17.

The geometry of the conduction micro-peaks of the contact depends on the surface state of conductors, but also on the load $P$ that presses the contact members together. A contact interface is usually divided into three zones:

- The apparent area of the contact $A_a$.
- The load bearing area of the contact $A_b$.
- The conducting area $A_c$: so called a-spots.

Because of the unevenness, the contact members touch each other in areas that are often plastically deformed, their sum being $A_b$ by definition. They may not all participate equally to bear the load, but the sum of the mechanical reactions must be oppositely equal to the load $P$ if the mechanical equilibrium is assumed. Furthermore the load bearing areas may not all be participating equallly to the current conduction, because some parts

can be covered by insulating layers, representative of the thin metal oxide layer, coating on the surfaces in contact or simply paint layers.

It can appear somehow arbitrary to devide $A_b$ between conductive and insulated areas, because the reality is highly dispersed and there is a continous range between the extreme cases of complete insulation or perfect conduction. Nevertheless the conductive area, $A_c$ is often described as the fraction of $A_b$ allowing current flow [38] [40], and the corresponding microscopic areas of metallic conduction are widely called *a-spots*, suggesting to model them by circular sections of radius $a$. One should keep in mind that theses areas are still subject to the possible presence of insulating layers. Figure 1.18 shows a schematics of the repartition of the areas $A_b$ and $A_c$ in a contact.

Although it is in practice nearly impossible to have a precise knowledge of these areas, $A_b$ can be guessed with a good amount of precision if we assume that all the bearing spots have reached the plasticity stress level. In that case, the bearing area would follow Equation 1.1, where $\sigma_y$ (Pa) is the yield strength of the material. Even if some spots are reacting elastically or if creep deformation has taken place, this assumption gives a good order of magnitude for $A_b$.

$$A_b = \frac{P}{\sigma_y} \tag{1.1}$$

The ratio between $A_c$ and $A_b$ is much more difficult to asses, because film layers are subject to mechanical damage in the presence of tightening forces or mechanical insertion and there is a lot of uncertainty concerning their thickness and even their presence.

What can be said is that usually, one may find $A_c < A_b \ll A_a$. Therefore, the current going from a contact member to the other will face resistance because it is constricted through a much smaller section than the apparent section of the bodies, and because it is sometimes forced to go through insulating layers or even through the air if no conducting solid path is available.

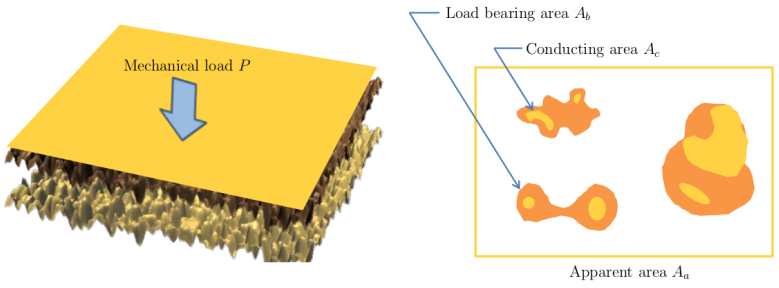


Figure 1.18: Apparent contact surface $A_a$, load-bearing area $A_b$ containing conducting spots $A_c$, the so-called a-spots. Taken from [41].

### 1.3.3 Holm's formula for a flat circular a-spot

In order to calculate the resistance of a conductor in static state, one usually assumes Ohm's law that requires the current vector to be proportional the electric field, that is the gradient of the potential function.

For a straight conductor of constant section, symmetry arguments make it easy to deduce the structure of equipotential surfaces. The current conservation is easily integrated in order to find a relation between to total current flowing through the conductor and the potential at its boundaries. The resistance of a conductor of section $S$, length $l$ and conductivity $\sigma$ is classically given by $\mathrm{R} = \frac{l}{S\sigma}$.

In the case of a constriction of the current lines as represented on Figure 1.17, the mathematical solution is much more complex. Using Smythe mathematical development, Holm's show in [38] that for a perfectly flat, circular and isolated a-spot of radius $a$, an analytical formula can be obtained, widely known in the literature as Holm's formula 1.2.

$$R_{\mathrm{c}} = \frac{1}{2a\sigma} \tag{1.2}$$

The mathematical steps that lead to this formula are presented in Appendix A. The ideas and the method of this development can be interesting in order to fully apprehend the multiple phenomena that will be observed in this thesis:

- Concentration of the current lines at the periphery of the a-spots
- Joule distribution in a non-flat a-spot
- Interaction of the current lines in a cluster of a-spots

To the author's knowledge, Holm's formula and method are used as a baseline model by most studies in the field of electrical contacts. However, the hypotheses made to obtain this formula are too restrictive for a wide range of applications. Studies often aim to enlarge Holm's method in order to model other aspects that do not appear in the case of a single and flat a-spot between two homogeneous conductors. This is the spirit that lead this thesis, driven by the need to asses phenomena that may occur at the microscopic scale of contacts subject to very high and impulsive currents.

### 1.3.4 Electric contacts subject to large currents

In the a-spots, the current density, the Joule effect and the electric field can be orders of magnitude higher than in the bulk material, and many physical phenomena occurring at this microscopic scale are of crucial importance for a wide range of industrial applications and research fields, such as the micro-electronics industry [41] [42] [43] , high current connectors, switching devices, breakers technologies [44], railguns [45], or spot-welding process [46].

The main differences between the many applications involving electric contacts rely in the nature of the materials, the surface treatment, the mechanical load on the contact and especially the current density level. Studies on electric contacts have been widely conducted in the Micro-Electro-Mechanical-System (MEMS) community, involving contacts subject to relatively small current density levels up to a few amperes, but during millions or billions of cycles of a few microseconds [47]. The performances of those systems strongly depend on their ability to sustain such large numbers of operating cycles with a constant electrical behaviour. The degradation and aging of these contacts is generally thought to be a consequence of a-spots failure, as heating and electromigration slowly degrade them until a usually fast breakdown [48]. On the other hand, applications related to welding, rail-guns, high current technologies and lightning stroke involve much higher current densities during much smaller time-scales, and the constraining physical phenomena may be very different. During the pulsed arc phase of a lightning stroke, the current can be as high as 200 kA on microsecond time-scales.

The resulting current levels in aeronautic assemblies are then higher than in most of the other high current applications, and there is a need for modelling strategies regarding the contact response to such current levels and time-scales, and regarding the ignition probability of critical energetic discharges. However, the phenomena occurring in contacts under high currents and related discharge phenomena are extremely complex due to the many physical processes involved. The response of the many a-spots ensuring the current flow in the contact is a result at high intensity of a strong electric, thermal, and mechanical coupling. Moreover, the contact response depends on the details of the surface micro-geometry that may lead to very different initial a-spots distributions.

Before addressing these physical aspects into details, it is important to evaluate the importance, in the context of lightning stroke, of two physical phenomena that are widely taken into account or conjured in the study of electric contacts for other kinds of applications. The electro-migration, that is responsible for the failure of most MEMS, and electronic emission in contacts subject to important voltage differences.

### Electromigration

Electro-migration is a diffusion motion of the metallic ions in a metal subject to an important current density. This motion is related to the drag force applied on ions due to the so-called “electron-wind", and the resulting electron-ion collisions. This transport process is very complex to model or to estimate analytically, since it relies on the presence of defects in the metal, such as nano-voids, or grain boundaries. However, such a diffusion process should take place on characteristic time-scales much larger than the typical duration of the pulsed arc phase of a lightning stroke.

A widely known approach to this problem is the Black formula [49], that makes it possible to compute the $MTTF$, “Mean Time To Failure", for a given current density

$j$ ($\mathrm{A\,m^{-2}}$), and a given temperature $T$ (K):

$$MTTF = Aj^{-n}e^{E_a/k_B T} \tag{1.3}$$

In Equation (1.3), $k_B$ ($\mathrm{J\,K^{-1}}$) is the Boltzman constant, $E_a$ (J) is an activation energy, and $n$ a parameter of the model. Both $E_a$ and $n$ depend on the materials and the micro-structure considered. An upper value for $j$ is obtained for example considering a D-wave current (100 kA) flowing in an a-spot with radius $a = 50\,\mu\mathrm{m}$, which gives $j \simeq 10^{13}\ \mathrm{A\,m^{-2}}$. Taking for example the values reported in [49], and a temperature of 1000 K, the lowest value obtained is of the order 3 µs, while it can be hours at 300 K. Then it seems that electro-migration is really a long-time process and that it is not relevant to consider it in the context of contacts subject to the pulsed arc phase of a lightning stroke, lasting from a few µs to 1 ms.

### Electronic emission

If the potential difference in a contact is large enough, the important electric-field may induce electronic emission from the metal and a significant current may flow between the parts, in parallel to the a-spots. To evaluate this effect, the widely known Schottky thermoionic and Fowler-Nordheim field emissions can be computed [50]. These widely used emission formulas have a limited validity range, and they should be used cautiously [51].

The material dependence is related to the work function of the material, which is the energy needed to extract an electron from the metal to the vacuum. The lowest the work function, the highest is the current that can be extracted from the metal. Schottky emission increases with both the metal temperature and the electric-field. At zero electric-field, it reduces to the Richardson emission. Fowler-Nordheim emission depends on the electric-field only, and is related to the tunnelling of electrons from the solid metal to the vacuum.

In order to have an upper estimate, a work function of 4 eV has been considered, together with a metal temperature of 1500 K. Schottky and Fowler-Nordheim emissions have been computed for a contact with a thickness of 10 µm and a voltage drop ranging from 1 V to 10 kV, which represent electric-fields in the range $10^5$ to $10^9\,\mathrm{V\,m^{-1}}$. The highest value is a quite unlikely upper estimate, but even with such a field the electronic emission seems rather low.

In the literature, a boost parameter $\beta$ is often added to increase the field. It should represent the electric-field enhancement due to micro-peaks on a given surface. A reasonable value is $\beta = 10$, meaning that the maximum field that can possibly be encountered in a contact is ten times the average field given by the voltage difference divided by the gap. Figure 1.19 shows the Schottky emission (thin continuous lines) and Fowler-Nordheim

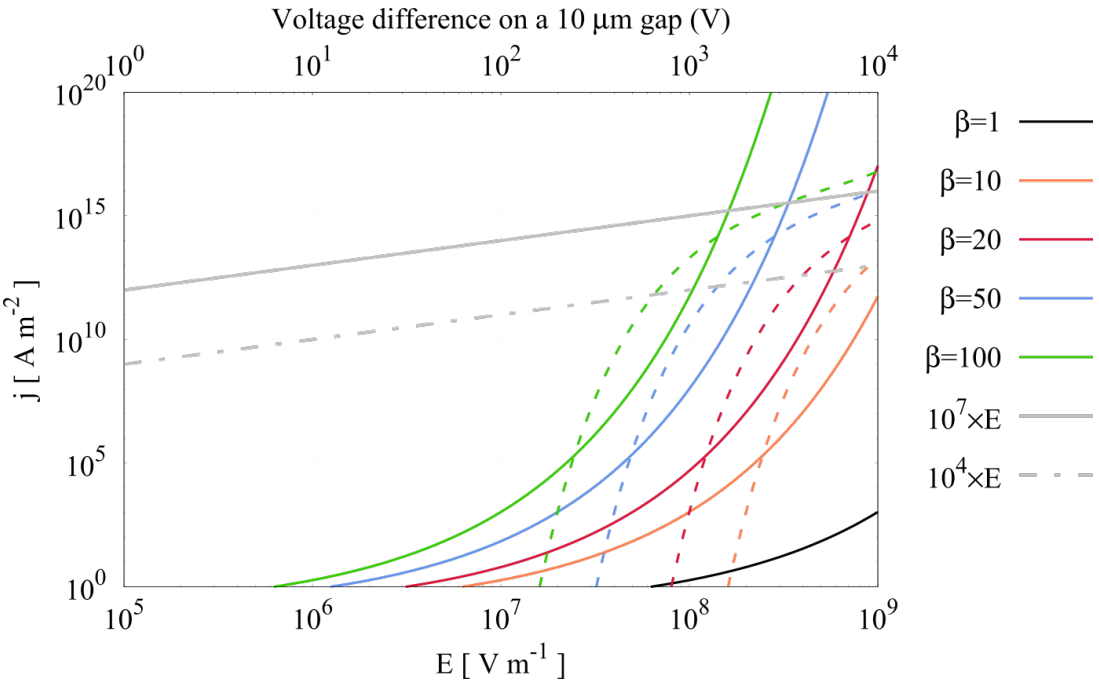


Figure 1.19: Schottky (continuous lines) and Fowler-Nordheim emissions (dashed lines) in a contact for boost parameters ranging from $\beta = 1$ to $\beta = 100$. Gray lines correspond to the conduction current densities in the a-spots for $\sigma = 10^4$ and $10^7\,\mathrm{S\,m^{-1}}$.

emission (thin dotted line) for beta ranging from $\beta = 1$ to $\beta = 100$. The electronic emission is compared to the current flowing by conduction in the contact, in the case of a metal-metal contact ($\sigma = 10^7\ \mathrm{S\,m^{-1}}$), and in the case of a carbon-metal or carbon-carbon contact ($\sigma = 10^4\ \mathrm{S\,m^{-1}}$). It can be clearly seen that the current density due to electronic emission is much lower by orders of magnitude than conduction currents for metal-metal contacts.

One could argue that considering the total current flowing in the contact, electronic emission currents could benefit from a much larger surface than conduction currents because $A_c \ll A_a$. However, the high field regions corresponding to $\beta > 1$ are related to small fractions of the apparent contact area, and in the case $\beta = 1$ the emission is so small than even with $A_c/A_a = 10^{-6}$ the current due to electronic emission seems negligible. Then it seems quite reasonable to ignore electronic emission in metal-metal contacts. For contacts involving carbon parts, the situation could be discussed since in this case the conductive current densities are much smaller and because carbon fibers may probably generate large $\beta$ values.

# Chapter 2

# Multiphysical modeling of single a-spot contacts

In aeronautic assemblies, some electric contacts may be related to the presence of defects. In this case, the electric contacts may consist in a single a-spot ensuring the current flow. It can be the case when considering alignment defects between non-interfering screws and bores, or defects in the insulating layers in contacts between parts with surface treatment or oxide layers. Contacts with very few or even a single a-spot can also be present between screws and bolts, in ball bearings, or in ball joints for example. Before dealing with contacts with many a-spots, it is then useful for applications and for better understanding to first focus on single a-spot contacts. For this purpose, a simple 0D a-spot model is developed in this section based on geometric simplifications and 2D finite volume simulations. This model has to take into account the complex electric, thermal and mechanical coupling that controls the dynamics of the a-spot under lightning stroke conditions.

## 2.1 Geometric simplifications

In realistic electric contacts, the geometry of the a-spots may be very complex and may differ significantly from one spot to another, regarding both shape and size. Moreover, there is no hope to fully characterize these micro-geometric details in any practical way, and geometric simplifications are then necessary. In this study, we assume that a-spots have a cylindrical geometry, characterized by a radius $a$ (m) and a thickness (or height) $l$ (m) as shown on Figure 2.1. Obviously, this simplification should be discussed. In many studies, the contacts' micro-geometry is even further simplified assuming perfectly flat circular contacts ($l$=0 m).

A film layer, representative of the thin metal oxide layer or coating on the surfaces in contact is often added as in [52]. This film resistance is difficult to address since electron

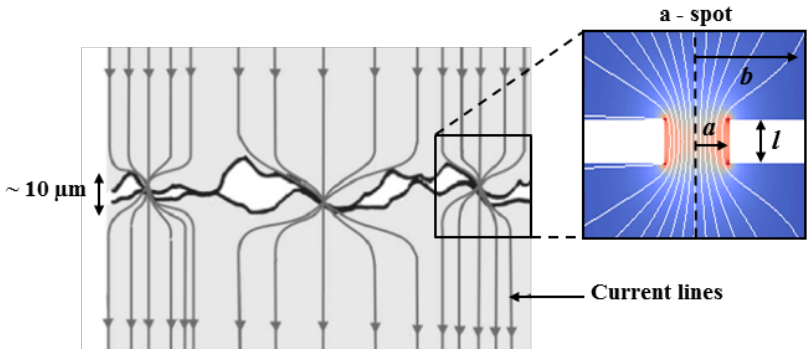


Figure 2.1: Schematics of an electric contact between two surfaces on a microscopic scale [39]: three a-spots represented.

transport in such thin insulating layers is very complex and may require taking into account tunnel effect, ballistic transport or electric breakdown on nanometer scales ([39], [52], [53]). To the author knowledge, most of the contact models addressing the presence of a film layer reduce it to a film resistance, rarely tackling the complex transport, electrical and mechanical phenomena taking place inside.

The presented model could be easily modified to take into account such a constant, passive film resistance in the cylindrical a-spot. In this case the only influence expected is on the current distribution in a multi-spot contact, but that would be equivalent to increase the averaged thickness of the a-spots ($l$). The influence of this geometric parameter on a multi-spot contact has been studied in Chapter 4.

Moreover, film layers are subject to mechanical damage in the presence of tightening forces or mechanical insertion and there is a lot of uncertainty concerning their thickness and even their presence in a-spots. Then the choice has been made in this study to consider as a first step pure metallic contacts without any film layer.

On the other hand, in order to correctly model the mechanical behavior of electric contacts, and more precisely the decreasing electric resistance with tightening force, it seemed necessary to keep information concerning their height, as in the spherical asperity models [40] [54]. Sphere models for a-spots could be more realistic than cylindrical models, but also bring much more complexity regarding multi-physics modelling, since mechanical, thermal and electric fields may be highly non-uniform in this case. The cylindrical approximation can be seen as an intermediate between perfectly flat contacts and spherical a-spots, and a good compromise between simplicity and refinement to take into account the most important physical processes.

Another argument in favour of the cylindrical a-spot approximation is that such a shape is likely for contacts subject to high tightening forces: It has been shown by mechanical finite element simulations in [55] that the deformation under high compression of two mating spheres may locally produce a cylindrical shape, as shown on Figure 2.2. The

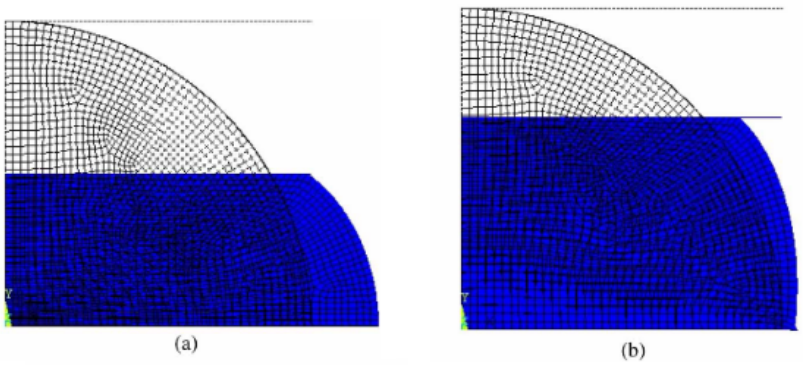


Figure 2.2: Representation of the FEM mesh and the deformed geometry of loaded spheres for each case: (a) deformable base and (b) rigid base. Taken from [56].

cylindrical a-spot model is then probably more accurate at high tightening forces than at very small loads.

In the following of this chapter, it has also been assumed that a-spots have a radius and a thickness of the same order of magnitude. It will be shown in Chapter 4 that this hypothesis is quite reasonable as long as the mechanical tightening force on the contact is not so high that a large plastic deformation regime is obtained in the a-spots. The chosen size of the single a-spot considered in this first study must not be seen as a realistic measurement, but was chosen so that the initial resistance of a contact be close to what is observed in practice.The motivation of this first chapter remains to increase our understanding of contacts and to develop a model that is suited for the study of more realistic surfaces.

Despite the geometric uncertainties, this work has been partly motivated by the hypothesis that in the case of realistic contacts with many a-spots in parallel, regularities in the high current dynamics will appear that will be function of macroscopic, available parameters, like the initial contact resistance, the tightening force, the materials and surface roughness, and that it will barely depends on the micro-geometric details and assumptions.

## 2.2 2D thermoelectric simulations

A-spots in aeronautic contacts under lightning stroke conditions may be subject to a Joule heating large enough to heat the solid materials up to the boiling point on microsecond time-scales. The current density distribution, Joule heating, and related thermal phenomena are then very important regarding the contact dynamics at high intensity.

A permanent-regime solution for the temperature field in a flat circular a-spot has been obtained in [38], following the so-called $\varphi - \theta$ relation, where the equipotential lines

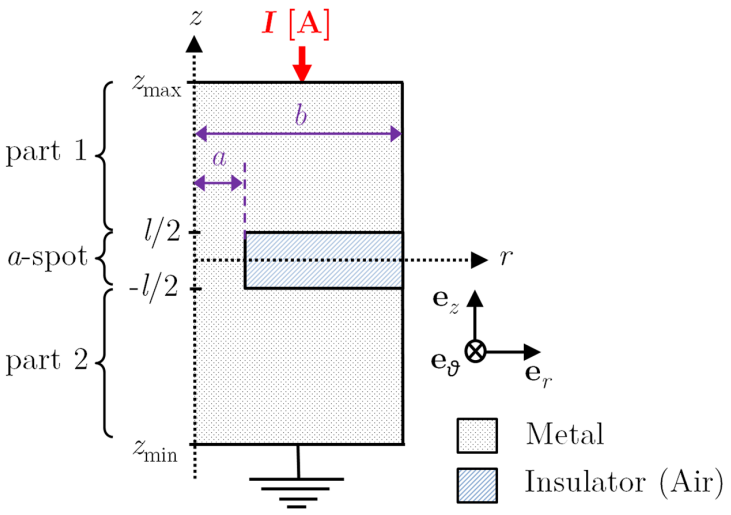


Figure 2.3: Representation of the single a-spot geometry considered in the 2D axisymmetric simulations.

and isotherms are merged. However, considering the time scales of interest during the pulsed arc phase of lightning stroke (∼1 µs), the thermal permanent regime hypothesis is irrelevant and a more detailed analysis of the unsteady current and temperature evolution in a single a-spot in those particular conditions is required.

For this purpose, 2D axisymmetric thermo-electric finite volume simulations have been performed in the cylindrical coordinate system $(r, \theta, z)$. The geometry consists in two conductive metallic parts separated by an insulating gap, which is most of the time filled with air in the context of aeronautic contacts. A single cylindrical a-spot, with a thickness $l$ and a radius $a$, connects these two parts as represented on Figure 2.3. The mesh is made of quads with geometric progressions in $r$ and $z$ directions in order to correctly discretize the a-spot, where very important thermal and potential gradients are expected.

Neumann boundary conditions are imposed at $r = 0\,\text{mm}$ to represent the axis, and $r = b$ to represent the border of the conductive volume. Indeed, no thermal or electron fluxes can cross these borders. On the top ($z = z_{max}$) and bottom ($z = z_{min}$) bondary conditions,the temperature is set to 300 K thanks to Dirichlet bondary conditions, meaning that the bulk material far from the a-spot is barely affected by Joule effect and thermal fluxes. Dirichlet boundary conditions are also imposed on the electric potential: at the bottom boundary, the electric potential is set to 0 V to represent the ground reference, and the applied voltage on the top boundary is computed at each timestep to ensure a current setpoint.

### 2.2.1 Electrostatic study of a single a-spot

As a first step, finite volume simulations have been performed to gain insight into the current distribution in a-spots, and to study the dependence of the electric resistance

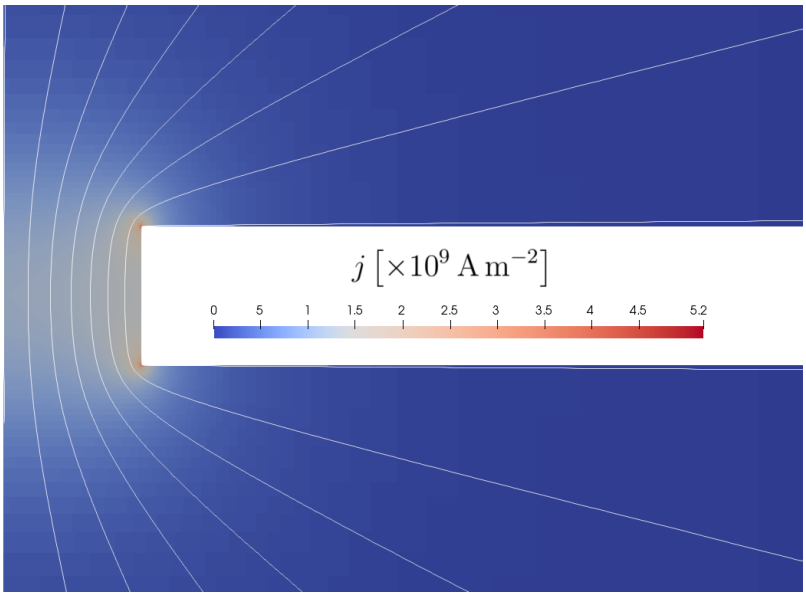


Figure 2.4: 2D axisymmetric simulation of the current density and current lines in a steel cylindrical a-spot subject to a permanent 1 kA current. $\sigma = 10^7\,\mathrm{S\,m^{-1}}$, $a = 500\,\mu\mathrm{m}$, $l = 500\,\mu\mathrm{m}$.

with the geometry. In this case the simulations are purely electrostatic, meaning that no heating dynamics or time-dependant phenomena are accounted for. The only equation solved in this case is the electrostatic current conservation equation 2.1:

$$\boldsymbol{\nabla} \cdot \boldsymbol{j} = -\boldsymbol{\nabla} \cdot \sigma \boldsymbol{\nabla} \varphi = 0 \tag{2.1}$$

where $\varphi$ (V) is the electric potential, $j$ (A) the current density vector, and $\sigma$ ($\mathrm{S\,m^{-1}}$) the electric conductivity. The current conservation equation is spacially discretized by means of a finite volume scheme, and the resulting sparse linear system is solved thanks to the SuperLU direct solver [57].

The 2D axisymmetric electrostatic simulations have been performed for a steel cylindrical a-spot ($\sigma \sim 10^7\,\mathrm{S\,m^{-1}}$) for different values of its radius and thickness. The constriction of the current lines can be observed on Figure 2.4, for the case of a cylinder of radius $a = 500\,\mu\mathrm{m}$ and thickness $l = 500\,\mu\mathrm{m}$. It can be noticed that the highest current densities take place at the border of the a-spot.

The value of the maximum current density obtained is $5.2 \times 10^9\,\mathrm{A\,m^{-2}}$, whereas the mean current density given by the ratio of the total imposed current to the area of the a-spot gives $1.27 \times 10^9\,\mathrm{A\,m^{-2}}$. This is in adequation with Holm's theory [38] that predicts a singular norm $j$ of the current density vector $\boldsymbol{j}$ ($\mathrm{A\,m^{-2}}$) at the rim ($r = a$) of a flat cylindrical constriction, accordingly to equation 2.2:

$$j(r) = \frac{I}{2 \cdot \pi \cdot a} \frac{1}{\sqrt{a^2 - r^2}} \tag{2.2}$$

where $I$ (A) is the total current flowing in the constriction and $r$ (m) is the distance from the symmetry axis. The current density profiles at $z = \pm\, l/2$ are very similar to the distribution given by Equation 2.2, which is representative of a current constriction. On the other hand, at the middle of the a-spot (z=0 mm), the current density is much more uniform due to the current diffusion in the cylinder. For a sufficiently large thickness, the current density would progressively transit from a constriction current distribution (at $z = \pm\, l/2$) to a uniform current distribution. For this reason, the total resistance of a cylindrical a-spot is not straightforward and no simple analytic formula would provide it as a function of $a$ and $l$ for the general case.

However, it has been observed that for a wide range of $a$ and $l$ parameters, representative of realistic a-spots in contacts, the resistance of a cylindrical a-spot may be very well approximated by the association in series of two terms: A cylindrical resistance $R_{\mathrm{cyl}}$ ($\Omega$), and a constriction resistance $R_{\mathrm{Holm}}$. The former is given by Equation 2.3, where $\sigma_{\mathrm{a}}$ ($\mathrm{S\,m^{-1}}$) is the electric conductivity of the a-spot material. The latter is related to the resistance of the bulk material as the current lines converge to the a-spot, and can be approximated by Holm's Equation 2.4, where $\sigma_{\mathrm{b}}$ is the electric conductivity of the bulk material.

$$R_{\mathrm{cyl}} = \frac{l}{\sigma_{\mathrm{a}} \cdot \pi \cdot a^2} \tag{2.3}$$

$$R_{\mathrm{Holm}} = \frac{1}{2 \cdot \sigma_{\mathrm{b}} \cdot a} \tag{2.4}$$

$$R_c = R_{\mathrm{cyl}} + R_{\mathrm{Holm}} \tag{2.5}$$

Then, the analytical formula considered in this study, for the resistance of a contact made of a single cylindrical a-spot, is given by Equation 2.5. The validity of this formula relies on two main hypothesis. Firstly Holm's formula for the constriction resistance is only valid if $a \ll b$, where $b$ is the size of the conductive domain. Secondly, the cylindrical term can be approximated by Equation 2.3 only if the a-spot is "not too flat", meaning that $l$ and $a$ are of the same order of magnitude, such that the current have "enough place" to diffuse from a constricted to a uniform distribution. The first condition is very well satisfied for contacts in aeronautic assemblies, but it should be kept in mind when considering new geometries. The second hypothesis is not very constraining, because very flat a-spots are unlikely, and even in this particular case the constriction term quickly dominates the cylindrical one. This could explain why formula 2.5 has been found to be precise enough for many different sets of $a$ and $l$ parameters.

For example, Figure 2.5 represents the total electric resistance for a-spots of thickness $l = 500\,\mu\mathrm{m}$ and with a radius $a$ varying in the range $100\,\mu\mathrm{m}$ to $600\,\mu\mathrm{m}$. The electric resistance calculated with Holm's formula $R_{\mathrm{Holm}}$ is represented with a black dashed curve

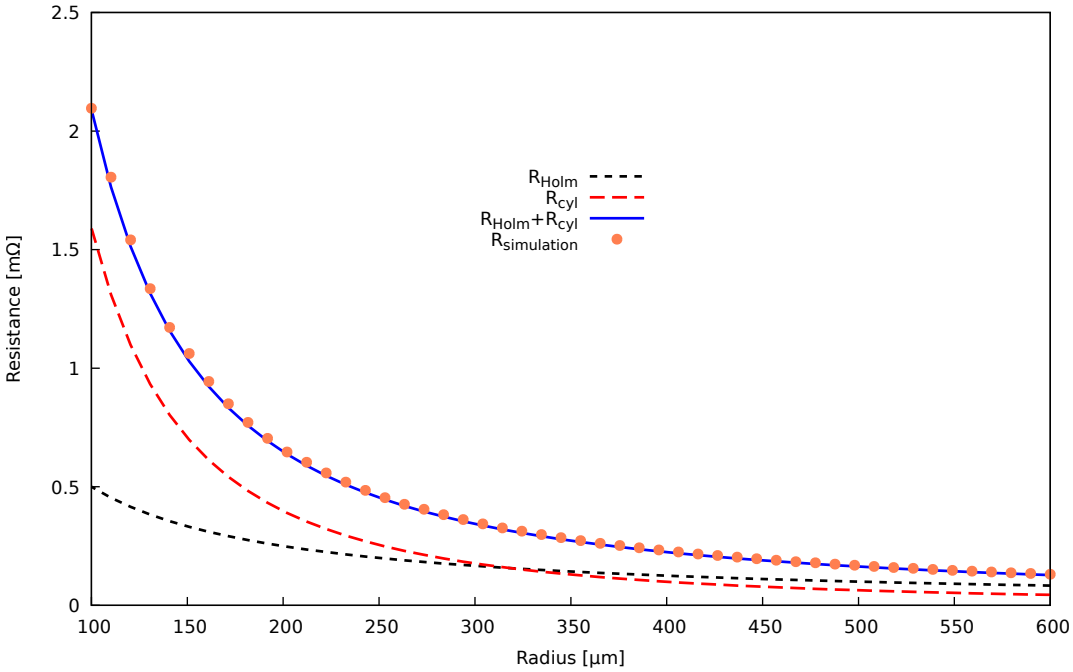


Figure 2.5: Resistance of a steel a-spot at 300 K as a function of its radius a: 2D-axisymetric simulations ($R_{\text{simulation}}$) and Holm's theory. $l = 500\,\mu\text{m}$, $\sigma = 10^7\,\text{S}\,\text{m}^{-1}$

along with the cylindrical term $R_{\text{cyl}}$ (red dashed curve). It can be observed that the sum of these two components, represented with a blue line, fits exactly the 2D axisymmetric simulations results (orange dotted line). It appears that the simple formula 2.5 remains always very satisfying for the resistance of the a-spot for such geometries.

Naturally, with a fixed thickness, the resistance of the contact decreases with the radius since the section of the a-spot increases. $R_{\text{cyl}}$ being proportional to $a^{-2}$, while $R_{\text{Holm}}$ is proportional to $a^{-1}$, its contribution to the total resistance $R_c$ for a given thickness $l$ is dominant for small radii, while for large radii the constriction resistance dominates.

We can conclude from this electrostatic study that Equation 2.5 gives a very good estimation of the contact resistance related to this geometry. Moreover, given the uncertainties on the microgeometry and the strong simplification considering cylindrical a-spots, a more detailed formula would bring unnecessary complexity to the model. Besides, this simple analysis validates the fact that the contribution of the thickness of the a-spot to the total resistance may be of the same order of magnitude and may even dominate the constriction term. This gives confidence in the fact that it should not be neglected in the context of aeronautic contacts, as it is often the case in many models in the literature.

### 2.2.2 Thermo-electric coupling

The current density distributions observed in the electrostatic simulations induces a highly non-uniform Joule heating and a temperature field that obeys the Fourier's conduction

law. With Joule heating, the specific internal energy of the material increases, which modifies the local properties such as the electric and thermal conductivities. The non-uniform distribution of material properties then modifies the current, the Joule heating, and the thermal conduction fluxes, as compared to the case of a uniform conductivity of Figure 2.4. During this electro-thermal dynamics, the temperature may reach the boiling or the melting points of the metal, leading to phase transitions and drastic changes in the material properties. Predicting this complex coupling between the current, the temperature, and the varying material properties is a challenging issue that has been adressed during this PhD by developping a 2D thermo-electric solver. This section is dedicated to the description of this solver, and to the most important simulation results obtained for the thermo-electric response of a single a-spot. Based on these results, the 0D electrostatic model previously described is enriched to take into account the observed vaporization dynamics.

**Solving of the coupled thermo-electric temporal evolution**

To solve the coupled electro-thermal phenomena in an a-spot subject to a lightning current, an explicit temporal scheme has been considered to successively solve the current distribution in the materials, and then the thermal phenomena related to Joule heating: At the beginning of each time-step, the volume internal energy $e$ ($\mathrm{J\,m^{-3}}$) is supposed to be known from initial conditions or previous time-steps in each cell of the simulation domain. The temperature field, the transport properties, such as electric and thermal conductivities, the thermal capacity, and the phases volume fractions are updated based on tabulated data. Then, the electrostatic current conservation equation with Seebeck effect 2.6 is solved to compute the potential distribution:

$$\boldsymbol{\nabla} \cdot \boldsymbol{j} = -\boldsymbol{\nabla} \cdot \sigma \left( \boldsymbol{\nabla}\varphi + S\boldsymbol{\nabla}T \right) = 0 \tag{2.6}$$

where $S$ is the Seebeck coefficient ($\mathrm{V\,K^{-1}}$) and $\sigma$ ($\mathrm{S\,m^{-1}}$) the updated electric conductivity evaluated at temperature $T$. During the time-step, the corresponding Joule heating distribution $-\boldsymbol{j} \cdot \boldsymbol{\nabla}(\varphi + TS)$ ($\mathrm{Wm^{-3}}$) is computed and used as a source term in the unsteady energy conservation equation with thermal diffusion 2.7 :

$$\partial_t e = -\boldsymbol{j} \cdot \boldsymbol{\nabla} \left( \varphi + TS \right) + \boldsymbol{\nabla} \cdot \left( \lambda \boldsymbol{\nabla} T \right) \tag{2.7}$$

where $\lambda$ ($\mathrm{W\,m^{-1}\,K^{-1}}$) is the thermal conductivity. Thermal conduction is treated with a semi-implicit temporal scheme and the resulting linear system is solved with the same numerical method as for the electric potential. It has been found that iterative solvers for the resolution of the linear systems coming from the finite volume discretization of 2.6 and 2.7 may lack accuracy and have in some cases difficulties to converge. For this reason, the SuperLU direct solver [57] has been used in all the presented results even if it

is slower compared to iterative solvers due to the need to factorize the matrices at each timestep.

This explicit coupling between electrical and thermal phenomena makes it possible to compute the evolution of the temperature as well as phase transitions provided that the time-step is small enough. In this study, the time-step $\Delta t$ considered is the minimum between the thermal diffusion time-step, and a time-step ensuring that the volume internal energy will never increase by more than 1 % during iterations:

$$\Delta t = \min\left(\frac{\Delta x^2}{2D},\ 0.01\frac{e}{\partial_t e}\right) \tag{2.8}$$

where $D$ ($\mathrm{m^2\,s^{-1}}$) is the thermal diffusion coefficient. First simulations were performed without taking into account Seebeck fluxes. However, the thermal gradients obtained in the a-spots may be as high as $10^9\,\mathrm{K\,m^{-1}}$. For metals, S is typically of the order $\pm 10^{-6}\,\mathrm{V\,K^{-1}}$, resulting in Seebeck currents of the order $10^{10}\,\mathrm{A\,m^{-2}}$. This Seebeck current value is far from negligible compared to voltage-induced current densities in a-spots lying in the range $10^8\,\mathrm{A\,m^{-2}}$ to $10^{12}\,\mathrm{A\,m^{-2}}$. Therefore this thermo-electric effect has been accounted for, even if it finally seems to have a limited influence on the presented results.

### Material properties dependence with temperature

Once the new volume internal energy $e$ is known from equation 2.7, the temperature field and phase transitions are updated thanks to Equation 2.9:

$$e\ (T) = e_0 + \int_{T_0}^{T} \rho c_v(T)\mathrm{d}T + \rho((Y_l + Y_g)L_\mathrm{f} + Y_g L_v) \tag{2.9}$$

This equation relates $e$ to the temperature and the mass fractions $Y_l$ and $Y_g$ of the liquid and gaseous phases respectively. $T_0$ (K) is the room temperature, $e_0$ ($\mathrm{J\,m^{-3}}$) the volume internal energy at $T_0$, $\rho$ ($\mathrm{kg\,m^{-3}}$) the mass density, $c_v$ ($\mathrm{J\,kg^{-1}\,K^{-1}}$) the specific thermal capacity at constant volume, and $L_f$ and $L_v$ ($\mathrm{J\,kg^{-1}}$) the fusion and vaporization latent specific heat.

The temperature dependent thermal capacity and thermal and electric conductivities of the solid metal up to the melting point have been obtained from references [58] and [59].

The transport properties in the biphasic regions are complex to address. Indeed, the averaged conductivity in a cell for a phase mixture strongly depends on the spatial distribution of their boundary inside the cell. Since this sub-cell phase distribution is not solved by the numerical method, it should be modelled based on physical assumptions. According to [60], if one assumes that vapor (resp. liquid) consists of spherical bubbles in the liquid (resp. solid), which is a “foam-like structure" of the two phases at the sub-cell

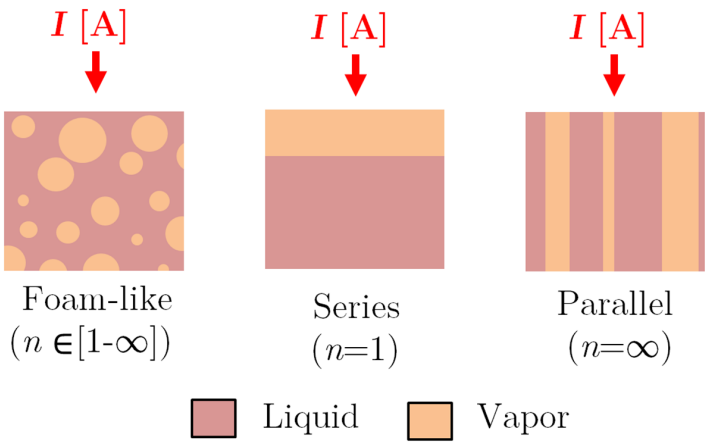


Figure 2.6: Sub-cell phase boudary distribution in a bi-phasic liquid-vapor region. Influence of the $n$ parameter of Equation 2.10 [60].

scale, then the electric conductivity is given by Equation 2.10

$$\sigma_{12} = \sigma_1 \left( 1 + \frac{\alpha_2}{\frac{\alpha_1}{n} - \frac{\sigma_1}{\sigma_1 - \sigma_2}} \right) \tag{2.10}$$

taken from [61], and where $\sigma_1$ is the electric conductivity of the liquid (resp. solid), $\sigma_2$ the conductivity of the vapor (resp. liquid), $\alpha_i$ the volume fraction of phase $i$ and $n$ is a tuning parameter. For the special case $n = 1$, Equation 2.10 gives a conductivity equivalent to a “pancake structure", where the two phases are attached in series, as represented on Figure 2.6. For the special case $n = \infty$, the two phases are attached in parallel. Intermediate values for $n$ correspond to more complex equivalent circuit models of two phases. In [60], the values $n = 3$ and $n = \infty$ are considered for cooper in the biphasic liquid-vapor region, depending on the equation of state of interest. The gazeous phase may have a conductivity orders of magnitude lower than the liquid phase. For this reason, the case $n = 1$ is much more resistive than for $n = \infty$. Then, the conductivity of the cell may collapse dramatically even for a very small volume fraction of vapor. In the case of a foam-like structure, this behaviour is quite unphysical. On the other hand, the parallel structure allows the current to flow exclusively inside the liquid while completely avoiding the much more resistive vapor phase. The resulting conductivity varies smoothly with the volume fraction of vapor, which seems to be much more physical for a foam structure.

In the following of this work, the parallel structure has been considered, and the electric conductivity in the biphasic region between phase 1 and phase 2 is given by Equation (2.11).

$$\sigma_{12} = \alpha_1 \sigma_1 + \alpha_2 \sigma_2 \tag{2.11}$$

Such an hypothesis is reasonnable for foam-like structures and volume fractions of

liquid larger than $\simeq$ 0.5. It is known however that such a medium may be subject to a percolation threashold if the volume fraction of liquid get too low, associated to a fast collapse of the electric conductivity to values similar to the series structure [62][63]. However, it will be shown in the following that the vaporization dynamics of the a-spot is extremely fast as soon as the boiling point is reached and a significant amount of vapor has been produced. In this context the detailed properties of the mixture for large volume fractions of vapor is not expected to significantly change the presented results.

### Metallic vapour modelling

It has been observed that the electric conductivity decrease with the temperature for solid and liquid state is of primary importance to accurately predict the current distribution. However, the conductivity of the metallic vapor state is difficult to estimate since in the hypothesis of isochoric heating the pressure may reach thousands of bars, which would imply a fast expansion, followed by a density decrease and a metal-insulator transition in the vapor, far beyond the scope of this study [64] [65].

As a first step, it has been assumed that the metallic vapor density decreases fast enough so that its conductivity would always be smaller than $10^4\,\mathrm{S\,m^{-1}}$. This conductivity value represents an upper value for fully ionized iron or any metallic plasma for temperatures of a few thousands of K between atmospheric pressure and hundreds of bars [66]. Even with this overestimated vapour conductivity, it remains much smaller than the conductivity of the solid phase ($\sim 10^7\,\mathrm{S\,m^{-1}}$), and it has been observed that no significant current flows through the gaseous phase. Then, the vaporization of the metal can be seen as a very fast decrease of the metal conductivity where it takes place.

### A-spot subject to a D-wave

The finite-volume thermo-electric model has been used to perform 2D axisymmetric simulations on different geometries and a-spot shapes. However, in this section, the choice has been made to focus on the vaporization of a particular cylindrical a-spot, which is reprensentative of the complex dynamics observed in most simulated cases. An a-spot of thickness $l = 400\,\mu\mathrm{m}$, and a radius $a = 400\,\mu\mathrm{m}$ has been considered.

The mesh is 420 cells in $z$ direction and 400 cells in the $r$ direction for a total of 168 000 cells. A geometric progression with a 1.12 ratio is used in both directions resulting in rectangular cells with a minimum size of $0.5\,\mu\mathrm{m}$.

The applied current is a normative bi-exponential D-wave current waveform. The current value at any time is given by Equation 2.12

$$I(t) = A\left(exp\left(-\alpha t\right) - exp\left(-\beta t\right)\right) \tag{2.12}$$

where $A = 109405$, $\alpha = 22708$, $\beta = 1294530$. As shown on Figure 2.7, the current

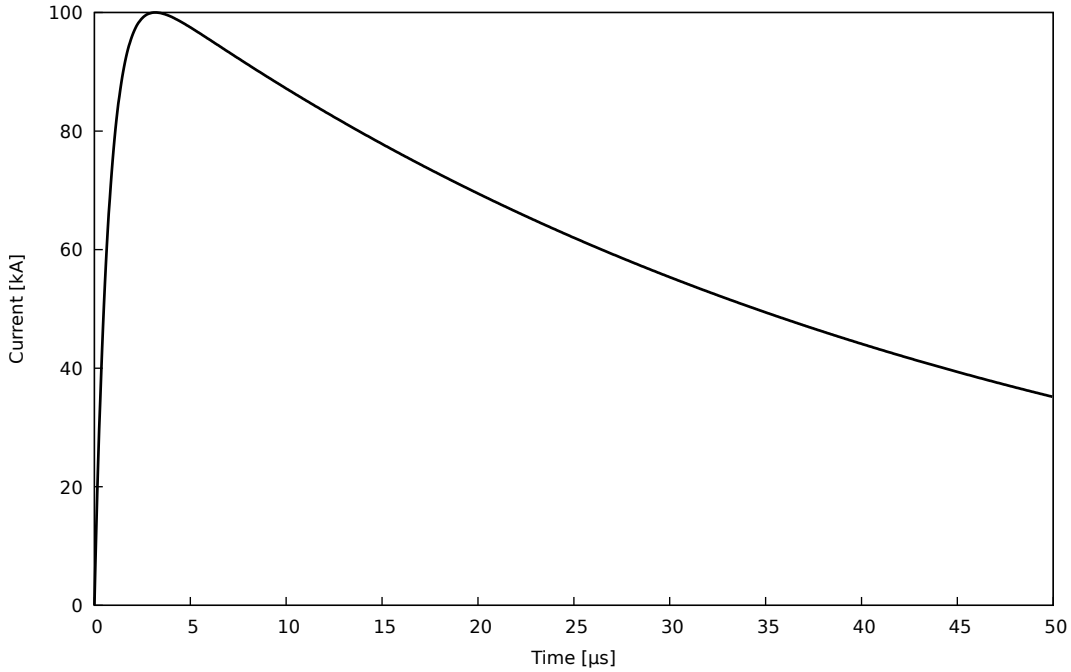


Figure 2.7: Evolution of the current value of a D-wave used in the simulations.

increases almost linnearly in the first microseconds, then reaches a maximum of 100 kA at $t = 3.6\,\mu s$ [30].

Figure 2.8 shows the temperature distribution and the current density lines at different times to illustrate the heating dynamics and the melting of the a-spot.

A black line, identified by a black arrow, tracks the points where the metal temperature has reached the melting point and where the bi-phasic solid-liquid region begins. Another black line (red arrow), tracks the end of the solid-liquid region, where the metal is fully liquid and the temperature starts to be higher than the melting point. All the melting dynamics take place at the very beginning of the D-wave ($t < 0.5\,\mu s, I < 50\,kA$), for which the lightning current is rising almost linearly starting from 0 A, as shown on Figure 2.9 (thin black line).

At t=370 ns, it can be seen on Figure 2.8 that the temperature field is quite homogeneous in the a-spot, but that a fusion front ignites in the corners of the a-spot. Before melting, two different phenomena may explain the uniform temperature distribution despite this non-homogeneous current density distribution tendency observed in permanent state: the thermal diffusion and the electric conductivity decrease with temperature. The later efficiently prevents the current density to keep flowing in regions with higher Joule effect and temperature, and facilitates the homogenization of the temperature field, whereas thermal diffusion tends to reduce thermal gradients. This homogeneous heating phase lasts for 370 ns, but the following melting dynamics is much faster.

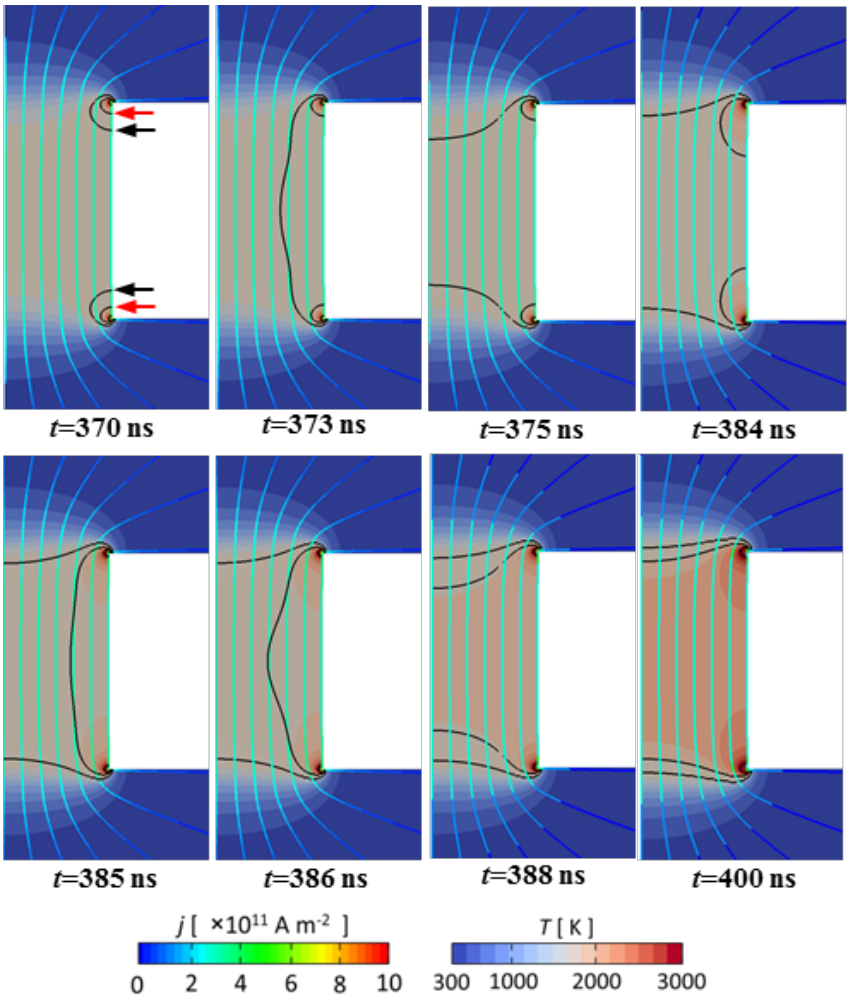


Figure 2.8: Sliced view of the temperature distribution and current density lines in a cylindrical a-spot ($a = 200\,\mu\text{m}, l = 400\,\mu\text{m}$ ) subject to a D-wave during the melting phase. Black curves indicate the limits of the solid-liquid bi-phasic region with pure solid state (black arrow) and with pure liquid state (red arrow).

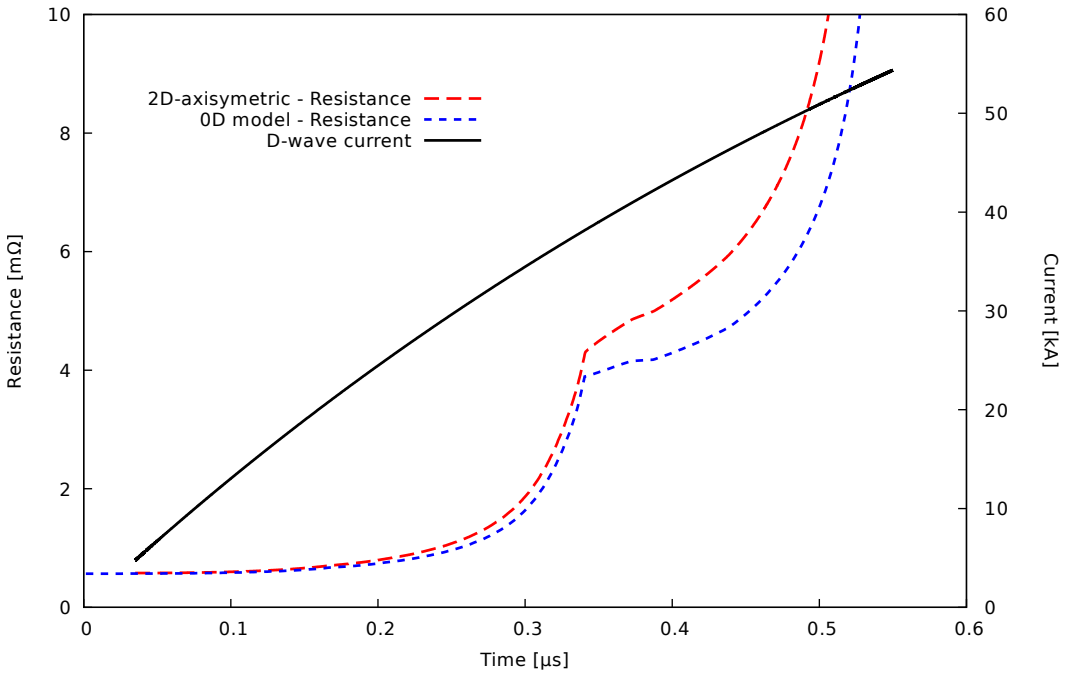


Figure 2.9: Evolution of the electric resistance of an a-spot of thickness $l = 400\,\mu m$ and initial radius of $200\,\mu m$ during the early stage of a D-wave lightning current (thin blue line). Comparison between the 2D-axisymmetric thermo-electric simulations and the 1D analytic model.

In less than 3 ns, the two fusion fronts that started in the corners have merged and the resulting fusion front starts to propagate from the rim of the a-spot to its center. At $t = 384\,ns$, most of the a-spot is in the solid-liquid bi-phase region and the volume of liquid metal is growing from the corners. A liquid front starts to propagate to the center 1 ns later and the a-spot is fully melt at $t = 400\,ns$.

Figure 2.10 shows the following vaporization dynamics of the a-spot. At $t = 425\,ns$, while the a-spot is entirely liquid, the metal starts to boil in the corners of the a-spot, where the beginning of the bi-phasic liquid-vapour region is delimited by black curves highlighted by blue arrows. At $t = 441\,ns$, the two boiling fronts starting from the corners merge and form a front at the periphery of the a-spot that propagates to the center. At $t = 443\,ns$, the boiling front as reached the symmetry axis and at $t = 500\,ns$ the a-spot is fully boiling in the bi-phasic liquid-vapour region. At the same time, a vaporization front starts at the corners of the a-spot as shown by the black curves highlighted by green arrows that track the beginning of the fully vaporized metal. These two vaporization fronts propagate directly from the corners to the center in less than 48 ns. Due to the very low conductivity of the vapour, the propagation of the vaporization fronts induces a fast constriction of the current lines.

The highlighted material dynamics have consequences on the contact resistance. During the first 300 ns, the decreasing conductivity of the a-spot with temperature results in

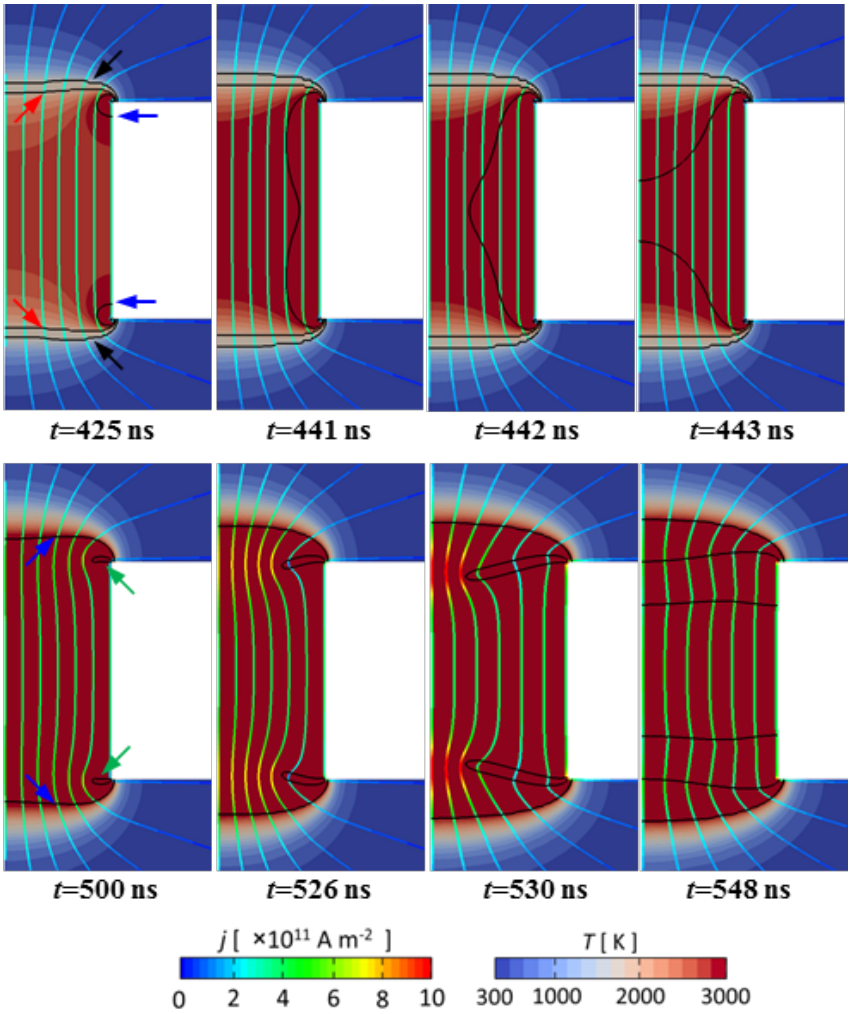


Figure 2.10: Vaporization phase following the melting phase presented in Figure 2.8. Black curves indicate the limits of the biphasic regions: solid-liquid with pure solid and pure liquids (black and red arrows respectively), and liquid-vapour with pure liquid and pure vapour (blue and green arrows respectively).

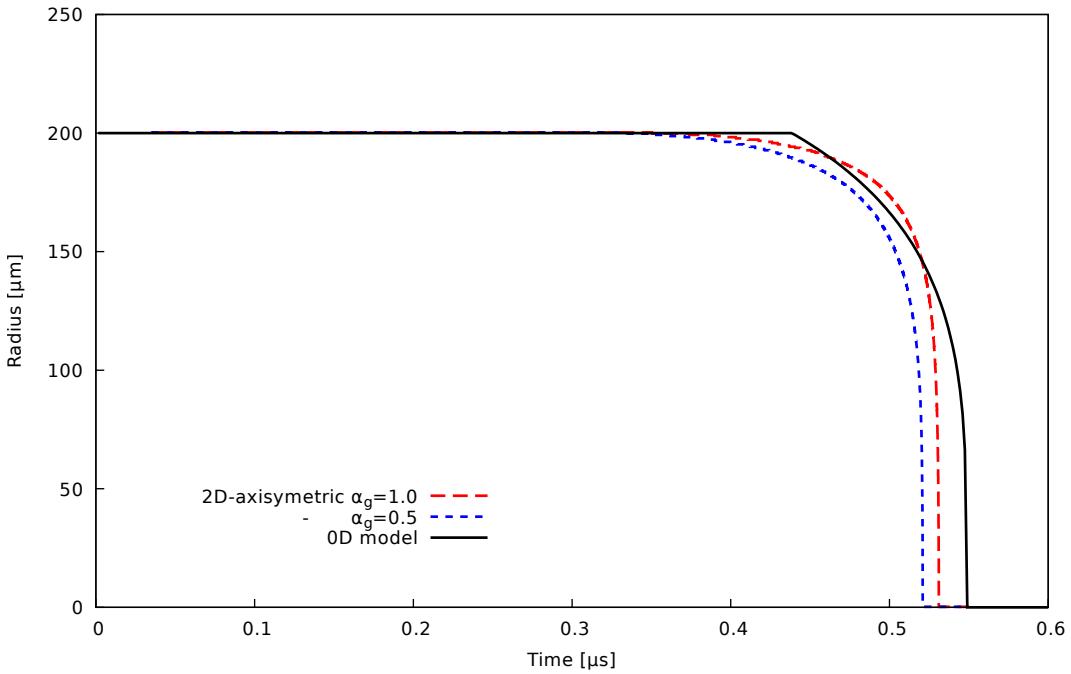


Figure 2.11: Evolution of the radius of a steel a-spot of thickness 400 µm subject to a D-wave current: pseudo-analytic model and 2D simulations.

an increasing resistance as can be seen on Figure 2.9 (red dotted line). Then, the resistance increases more slowly due to the beginning of the fusion dynamics that consumes most of the injected energy in latent heat of fusion, without increasing the temperature and altering the conductivity. However, the total resistance of the a-spot increases exponentially at around $t = 500\,\text{ns}$ with the beginning of the vaporization front. This very fast resistance increase due to the constriction of the current lines can be interpreted as a fast decrease of the conduction radius of the a-spot.

Defining the conduction radius during vaporization is not straightforward due to the highly non-homogeneous current density and vaporization front. To address this uncertainty, two conduction radii have been considered. The first one is defined as the minimum radial position where a fully vaporized metal can be found in the a-spot. Intuitively, it is reasonable to assume that this vapour region locally induces a strong constriction of the current lines that controls the total a-spot resistance. Since the conductivity given by Equation 2.11 in the biphasic liquid-vapour region sharply decreases with the growing volume fraction of metallic vapour $\alpha_g$, a second conduction radius has been defined as the minimal radial position in the a-spot where the volume fraction of vapour is $\alpha_g = 0.5$. This radius gives an lower bound estimate for the conduction radius. These two radii are shown on Figure 2.11 as a function of time.

The red dashed line shows the evolution of the conduction radius defined with the full vaporization criteria ($\alpha_g = 1$), while the blue dotted line shows the evolution of the radius

defined with the half vaporization criteria ($\alpha_g = 0.5$). Consistently with Figure 2.10 and Figure 2.9, at first, these two radii slowly decrease between 400 ns and 500 ns, corresponding to the beginning of the bi-phasic liquid-vapour region. Then, a very fast collapse in less than 50 ns can be observed resulting from the vaporization fronts ignited at the periphery of the a-spot and converging to its center.

This fast collapse of the conduction radius of the a-spot as soon as a vaporization front has ignited on its rim has been observed in many simulations with different shapes and dimensions, and even taking into account additional physical process such as radiative losses. Then it seems to be a quite general dynamics that barely depends on the detailed geometry of the a-spot. The main reason is probably the dominance of the following thermo-electrical instability: The current density and the Joule heating reach their maximum somewhere on the rim of the a-spot due to geometric effects, no matter its precise shape or size. Then a vaporization front propagates from the periphery to the center of the a-spot, resulting in a decreasing conduction radius, and an increasing electrical resistance. This resistance increase due to vaporization cumulates with the increasing current of the D-wave and the temperature decreasing conductivity of the material, leading to an even faster vaporization rate.

## 2.3 0D simplified model

The computational cost needed to perform the 2D axisymmetric simulations presented in the previous section does not allow to consider a parametric study on a realistic 3D surface made of hundreds of a-spots. At first, the modelling strategy under consideration was to run many instances of the sequential 2D thermo-electric solver on many processors, each with a particular a-spot geometry. Then, to model the affiliation of these a-spots to the same contact, parallel instructions would have been implemented to ditribute the total imposed current between the different a-spots.

However, even with this modelling strategy a parametric study would have been computationnaly expensive and the interactions between the a-spots much more complex to implement. For that reason, the possibility to simulate the complex thermo-electric dynamics of an a-spot with a simple and much less computationnaly demanding approach has been investigated.

The main requirement for such an approach is to deliver good qualitative estimates of several parameters of interest: the size of the a-spot, its internal state (temperature, liquid or gaseous volume fractions) and the corresponding electrical resistance. To match these requirements, the 0D electrostatic model of a cylindrical a-spot has been enhanced with a thermo-electric model that relies on hypotheses formulated based on the 2D simulation results.

Besides, it has been found that the mechanical response of the a-spots to a tightening force is of primary importance in the context of aeronautic contacts. Then, a simple mechanical model has been added to the 0D thermo-electric model, and the effect of the tightening force on a single a-spot contact have been emphasized.

### 2.3.1 Thermo-electric model

The thermoelectric 0D model is described in this section, and has been developed based on the 2D thermo-electric numerical simulations previously described. The following hypotheses have been made :

- The a-spot geometry is assumed to be cylindrical, characterized by a radius $a$ and a thickness $l$.
- The total resistance of the a-spot is given by formula 2.5, with a constriction term $R_{\text{Holm}}$, and a cylindrical term $R_{\text{cyl}}$.
- The constriction resistance is given by Holm's formula 2.4, and the cylindrical term by formula 2.3.
- The Joule power dissipated into the a-spot by the current $I(\text{A})$ is given by $R_{\text{cyl}} \cdot I^2$.
- If the temperature of the a-spot $T$ is lower than the boiling point $T_{\text{v}}$, the power is distributed homogeneously and so rises the temperature following Equation 2.13:

$$\pi \cdot \rho \cdot l \cdot a^2 \cdot c_{\text{v}} \cdot \partial_t T = R_{\text{cyl}}(a) \cdot I^2 \tag{2.13}$$

  where $c_{\text{v}}$ ($\text{J}\,\text{kg}^{-1}\,\text{K}^{-1}$) is the specific heat capacity.

- If $T = T_{\text{v}}$ the Joule heating generates a vaporization front going from the a-spot periphery to its center, and the evolution of the a-spot radius is given by the differential Equation 2.14:

$$2\pi \cdot \rho \cdot l \cdot a \cdot \partial_t a = \frac{R_{\text{cyl}}(a) \cdot I^2}{L_{\text{v}}} \tag{2.14}$$

  where $L_{\text{v}}$ ($\text{J}\,\text{kg}^{-1}$) is the specific latent heat of vaporization.

- The metallic vapour has a zero conductivity.
- In the bi-phase regions ($T = T_{\text{f}}$ and $T = T_{\text{v}}$), the electric conductivity is given by Equation 2.11.

The first three hypotheses are similar to the geometric and electrical simplifications used in the 2D simulations. The comparison of the values given by the analytical formulas and the values given by the simulations, presented on Figure 2.5, gives confidence in this electrical simplification.

In the fourth hypothesis of the model, Holm's resistance has been ignored for the Joule heating estimate since it is related to the constriction of the current lines in the bulk material, and does not participate to the temperature increase inside the a-spot, which is only due to the cylindrical resistance. Moreover, 2D numerical simulations have revealed that the Joule heating due to the constriction resistance has a negligible influence compared to the Joule heating inside the a-spot, since no significant temperature increase has been observed in the bulk material. This is consistent with Holm's theory, according to which the Joule heating decreases in $z^{-4}$, where $z$ is the distance from the constriction (see Figure 2.3). Besides, considering the thermal diffusivity of steel $D \simeq 13 \times 10^{-6}\,\mathrm{m^2\,s^{-1}}$ and the characteristic pulsation of a lightning current $\omega \simeq 10^6\,\mathrm{s^{-1}}$, the thermal signal penetration thickness $\delta = \sqrt{\frac{2D}{\omega}}$ is of the order 10 µm. Then thermal losses due to thermal diffusion from the a-spot to the bulk material can be ignored as a first approximation, as shown by the 2D simulations. To summarise, a-spots are considered adiabatically isolated from the bulk material during the time of a lightning stroke.

The fifth hypothesis corresponds to the rather homogeneous temperature increase observed with the 2D axisymmetric simulations until the boiling starts. On the other hand, the sixth hypothesis corresponds to the observation that once the boiling temperature has been reached, the ignition of a vaporisation front occurs very fast. Instead of trying to model the complex front dynamics observed in Figure 2.10, it has been considered that all the power dissipated by Joule heating during this phase was used to vaporize the metal at the periphery of the a-spot.

In Equations 2.13 and 2.14, $R_{\mathrm{cyl}}$ non-linearly depends on the temperature $T$ and the a-spot radius $a$ respectively. Moreover, the material properties $c_{\mathrm{v}}$ and $\sigma$ are also non-linearly temperature dependent. As a consequence, these two non-linear ordinary differential equations cannot be solved analytically and a numerical integration is required. For this purpose, a simple explicit time integration scheme with a Runge-Kutta method or any ODE solver can be employed.

The two last hypotheses are the most questionable since they are related to the electric conductivity in the vapour and in the liquid-vapour biphasic regions. As for the 2D simulations, it has been assumed as a first step that no current flows through the vapour, and that the two phases are well mixed in the bi-phasic region. In Chapter 5 the effect of the vapour will be addressed more precisely, but as a first approximation it has been considered that boiling can be seen as a fast decrease of the conductivity.

Figure 2.9 and Figure 2.11 show respectively the evolution of the resistance and the radius of a 200 µm steel a-spot subject to a D-wave current. The results from this pseudo-

analytic 0D model are compared to the 2D axisymmetric simulation results previously described. Both models predict similar dynamics: the a-spot vaporization occurs very fast, in less than 0.6 µs. This is due to the increase of the resistance as the a-spot is vaporized, and simultaneously to the increase of the current, that results in an increase of the Joule effect and the vaporization rate. The two models seem to predict the beginning of the vaporization at around 0.45 µs, which means at the very beginning of the D-wave. This is a strong indication that when a lightning current is flowing through an assembly with many electric contacts, current redistribution phenomena may take place on very short time-scales.

The differences in the radius evolution between the two models are mainly due to the hypothesis of a vaporization front in the analytical model, that over simplifies the complex vaporization dynamics observed in the 2D simulations. However, considering the uncertainty of the model, and the geometric approximations necessary for the description of realistic contacts, the agreement seems more than enough for this 0D thermo-electric model.

### 2.3.2 Mechanical tightening model

An important phenomenon, not taken into account in the 2D axi-symmetric simulations has to be included in the 0D model for the special case of electric contacts subject to a mechanical load: the mechanical flattening of the a-spot due to the tightening force. This mechanical response is rather complex in general because a-spots can be subject to large mechanical deformations, leading to large modifications of their shape and size. Moreover, due to the fast temperature increase inside an a-spot, the mechanical properties of the material may evolve dramatically. More precisely, it is well known that the Young modulus and the yield strength decrease with temperature for metals and that a fast collapse occurs near the melting point [67].

To simulate the mechanical response of a realistic contact to a varying mechanical load, S. Schoft has considered in [40] that the asperities of the surfaces in a contact have initially, before tightening, a spherical shape. He then used 3D FEM (Finite Element Method) mechanical code to press two spheres against each other until a given separating distance $d$ between the centers of the spheres is obtained, referred to as the tightening separation. Thanks to these mechanical simulations, the physical contact area between the spheres and the mechanical reaction force for a given set of constant material properties have been analytically fit as a function of the radius of the spheres and their separating distance $d$. In [40], those analytical fits have been used to find the proper tightening distance for which the mechanical reaction force is equal to a given tightening load, and then to deduce the a-spots radius and the electrical resistance.

3D FEM mechanical simulations are able to catch precisely the detailed mechanical

response of an a-spot subject to a given load [68], but they still rely on important geometric simplifications. Moreover, the numerical cost of these simulations is way too large to be used in a simple contact model with many a-spots. The strategy adopted by Schoft is restricted to an electro-mechanical coupling, useful to study the dependence of the contact resistance with the tightening force. However, deriving analytical fits that take into account thermal phenomena such as vaporization and temperature dependent conductivities would be much more complex.

### 2.3.3 Mechanical tightening of a cylindrical a-spot

The strategy adopted here is to use a simple mechanical model that is compatible with both electric and thermal phenomena. The main drawback of spherical a-spot models is the large deformations that can be obtained at high tightening force, or when the temperature increases significantly, that may change their shape. For this reason, any model relying on the spherical a-spot hypothesis would fail after a too large mechanical crushing. On the other hand, cylindrical a-spots do not suffer this limitation because the cylindrical geometry is preserved even for large mechanical deformations. The hypothesis of a uniform heating up to the boiling point and then a vaporization front propagating from the periphery to the center also conserves the cylindrical geometry.

As a result, a simple mechanical model for cylindrical a-spots has been derived based on the following hypotheses:

- A quasi-static mechanical equilibrium is assumed at all time: $F = \pi \cdot a^2 \cdot \sigma$, where $F$ (N) is the tightening force, and $\sigma$ (Pa) the mechanical stress.
- The constraint $\sigma$ follows an elastoplastic deformation law characterized by a yield limit $\sigma_y$ (Pa), a Young modulus $E$ (Pa) and a creep exponent $n$.
- The cylindrical shape is maintained during tightening.
- In the elastic region ($\sigma < \sigma_y$), we neglect the effect of the Poisson coefficient and the radius of the cylindrical a-spot is kept constant. The constraint $\sigma$ is given by Hooke's law: $\sigma = E \cdot \epsilon$. The strain $\epsilon$ is simply given by $\epsilon = l/l_0$, where $l_0$ is the initial thickness of the a-spot.
- In the plastic region ($\sigma > \sigma_y$), the volume is conserved: the a-spot radius increases when its thickness decreases due to the tightening force. The constraint increases by creep.

The first hypothesis is questionable since the time-step required in the 2D simulations to catch the thermo-electric evolution is of the order 1 ns. Considering the speed of sound in iron, the mechanical wave displacement would be around 5 µm for such a time-step,

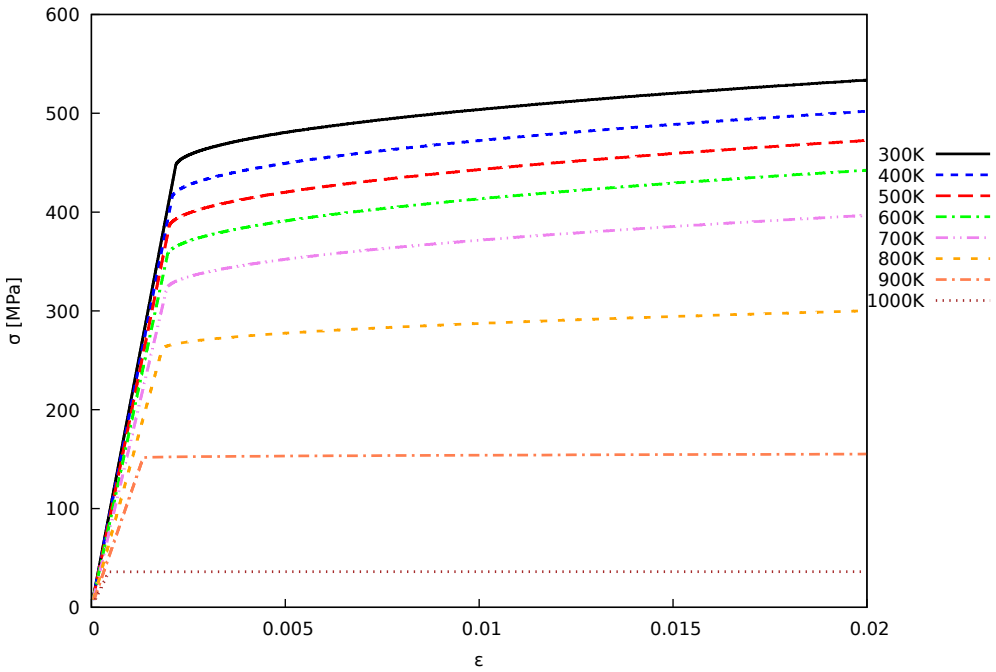


Figure 2.12: Stress-strain profiles obtained when applying an increasing load on a cylinder a-spot, for different temperatures.

which is smaller than the characteristic scales of large a-spots (∼100 µm). However, a mechanical equilibrium every 20 ns is in this case reasonable, which is quite smaller than the characteristic time-scale for the resistance and radius evolution of an a-spot before vaporization (see Figure 2.13). Taking into account out-of-equilibrium mechanical effects, such as inertia effects, finite speed of sound or strain-rate dependent stress in the material would possibly bring some high frequency dynamical effects in some particular cases (large a-spots). It is however not expected to dramatically change the numerical results presented hereinafter, that occur on larger time-scales. In future works, it would be interesting to focus on these aspects into more details, which would require using a fast-dynamics software, and derive simple analytical formulas as in [40]. Such a work is beyond the scope of this study, and given the uncertainties on the geometry, the quasi-static mechanical equilibrium hypothesis seems to be rather reasonable as a first approximation to catch the most important mechanical effects.

The fourth hypothesis is a simplification that does not affect significantly the presented results, since most of the a-spot flattening and radius evolution occurs in the plastic region.

### 2.3.4 Thermo-mechanical coupling

The material properties (Young Modulus, yield strength and plastic creep) are functions of the temperature, following a Johnson-Cook law [69]. The temperature dependant parameters of this law are taken from NIST databases for high resistance steel [70].

Figure 2.12 shows the stress-strain relationship observed when applying an increasing load on a given steel cylinder, for different given temperatures. A typical elastic region is followed by plasticity, where the yield strength increases by creep action. As can be expected, the Yield modulus and yield strength of a metal decrease with increasing temperature.

To couple this simple mechanical model with the thermo-electric 0D model described previously, a new mechanical equilibrium is computed for the a-spot at the end of each time-step, based on the updated mechanical properties to take into account the temperature evolution. The mechanical load is given as an input, and the tightening distance is computed with a dichotomy method in order to reach equality between the tightening force and the material reaction.

## 2.4 Parametrical study

In this part, the 0D a-spot model is used to perform a parametric analysis for a single a-spot contact subject to a D-wave current waveform. The initial radius of the a-spot is emphasized, and two very different situations are considered: contacts in the presence of a tightening force, and contacts with a zero tightening force, which means a constant tightening distance. These two situations should be viewed as limit cases for a wide range of configurations that may be encountered in actual electric contacts in aeronautic assemblies. It is for example possible in practice, that a tightening force exist but linearly decrease with the tightening distance. An other interesting situation may be encountered, where the load is distributed between different parts, or between the a-spots of a contact and an interface insulating layer. In this case the load would be for example exclusively held by the a-spots at the beginning, but as soon as the tightening distance decreases and other parts come into play, the load on the a-spots would diminish and the tightening distance converge to a value where all the load is supported by isolating surfaces.

Given the very different dynamics observed in the two limit cases, it is very important when considering a contact in an assembly, to first examine the geometry and all operating forces, in order to determine in which situation is the contact of interest. For example, the constant tightening force may be representative of a contact between a screw and a bolt, due to the presence of large mechanical constraints. On the other hand, the case with constant separating distance may be representative of a contact induced by an alignment defect between two parts.

A particular attention is made on the initial resistance of the different contacts considered. Indeed, this initial electrical resistance corresponds to the resistance of the contact when the materials are at the room temperature, and when the current is low enough such that no non-linear phenomena take place. This “low-level resistance", can be determined experimentally in a reliable way, for example using a micro-ohmmeter, or imposing

a low current level in the assembly to ensure a negligible Joule heating, and making use of voltage probes. The initial, low-level resistance may be predicted by the 0D thermo-electro-mechanical model given the initial a-spot radius and a given tightening force.

### 2.4.1 Single a-spot contact with constant thickness

A zero tightening force means a constant distance between the two parts in contact, since no gravity or other acceleration sources are considered in this model. In the case of a single a-spot contact, all the injected current flows through the a-spot and the temperature increase can only lead to an increase of the electrical resistance of the contact: As previously shown by 2D simulations, in the case of a 200 µm a-spot (see Figure 2.9), there is first an increase of the resistance due to the conductivity decrease with temperature and then an exponential growth due to the vaporization dynamics that results in the collapse of the a-spot radius.

The 0D model described previously is able to catch the influence of the initial radius as shown on Figure 2.13 and Figure 2.14, that represent the evolution of the radius and electrical resistance of contacts with different initial a-spot radii of $150, 200, 250, 300$ and $350$ µm, but with a total initial resistance of $1\,\mathrm{m\Omega}$ in all the cases. This value was chosen so that it be in the order of magnitude of the resistances measured in aeronautical assemblies.

In order to keep the total resistance unchanged while varying the a-spot radius, it is necessary to change the thickness $l$ of the a-spot (cf. Equations 2.4 to 2.1). Then, for a given contact resistance, a-spots with a larger initial radius also have a larger thickness, and a much larger volume than a-spots with a small radius. The time necessary to reach the boiling point and the total vaporization of an a-spot being proportional to its surface, a-spots with larger radii last longer than a-spots with smaller ones, as shown on Figure 2.13. In fact, the radii evolutions depicted on Figure 2.13 depend on the total injected current, but do not depend on the initial total resistance of the contact: a different contact resistance for these particular a-spot radii would simply lead to a modification of their thickness. However, the ratio between the Joule heating and the volume of an a-spot is independent of its thickness, and so are the temperature evolution and the vaporization dynamics.

Consistently, Figure 2.14 reveals that starting from a same initial resistance, contacts with a smaller a-spot radius sustain much less current than contacts with larger ones, meaning an earlier and faster resistance increase.

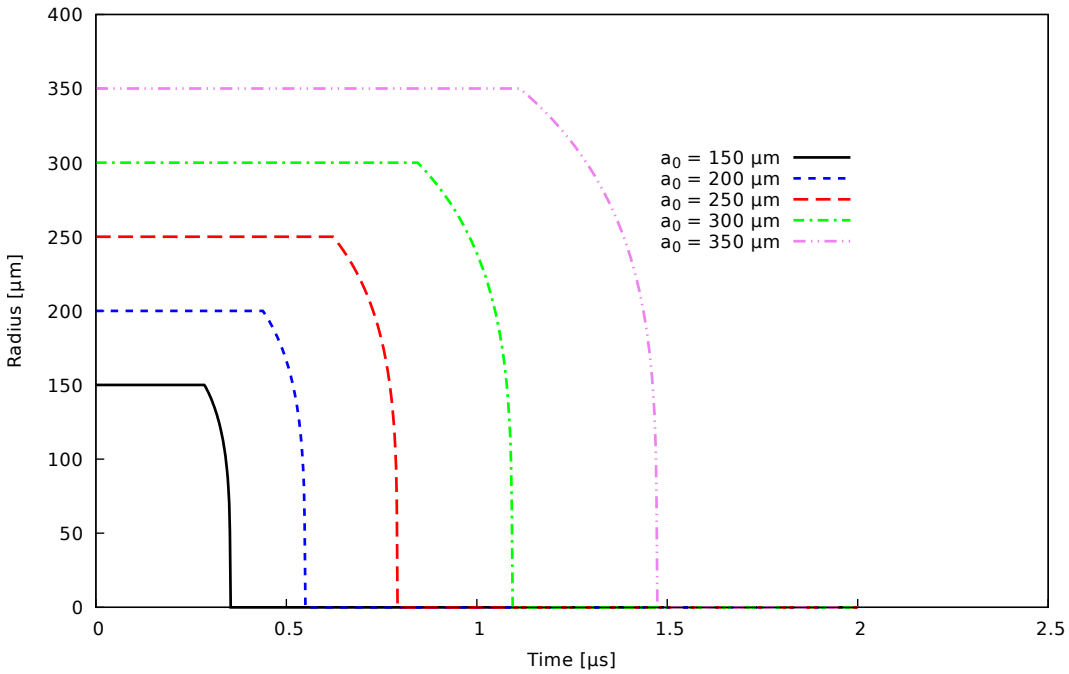


Figure 2.13: Evolution of the radius of a cylindrical steel a-spot subject to a D-wave for different initial a-spot radii $a_0$, assuming their length is constant and leading to the same initial resistance of 1 mΩ.

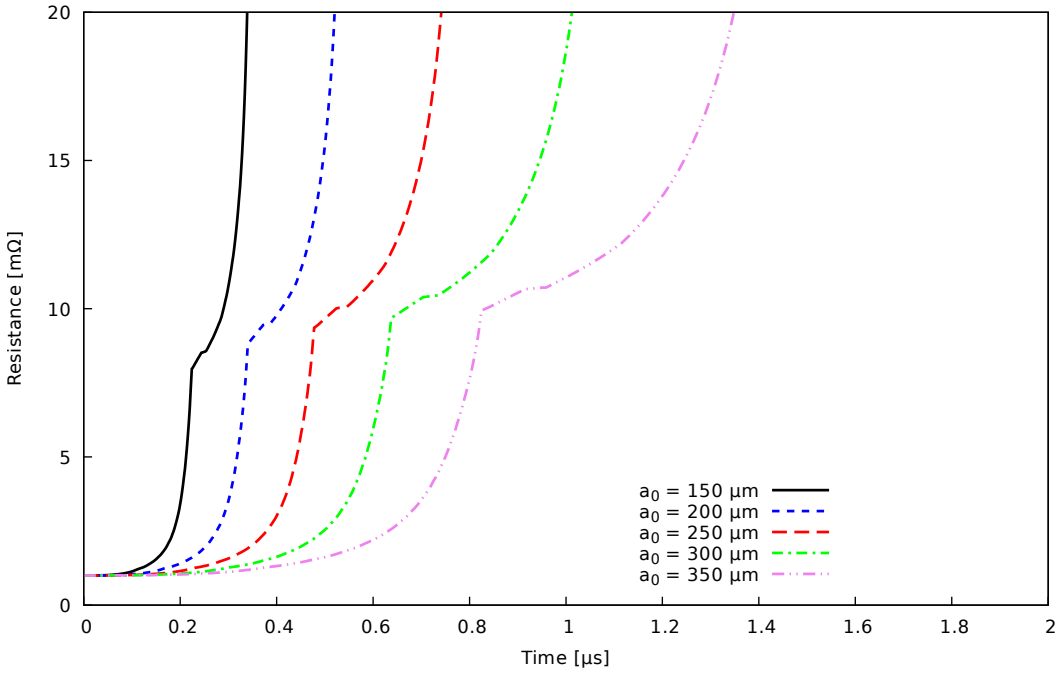


Figure 2.14: Evolution of the resistance of a cylindrical steel a-spot subject to a D-wave for different initial a-spot radii $a_0$, assuming their length is constant and leading to the same initial resistance of 1 mΩ.

### 2.4.2 Single a-spot contact with mechanical load

In this section, we put emphasis on the influence of a tightening force on the response of a single a-spot contact. A fixed a-spot geometry before tightening is considered with a radius of 200 µm and a thickness of 400 µm. Four tightening forces are considered: 1 N, 10 N, 100 N and 1000 N. The latter is well representative of the load that may be present on the fasteners in aeronautic assemblies. Once again, the contact is subject to a D-wave current, but this time, the separating distance between the two parts, which is the thickness of the a-spot, is updated at each time-step to maintain the mechanical equilibrium condition: the reaction force of the a-spot, which is the product of the stress by the a-spot surface, is always equal to the applied load $F$ (N).

The time evolutions of the a-spot radius and thickness in the contact for the different tightening forces are depicted on Figure 2.15 and Figure 2.16 respectively. At $t = 0$ µs, it can be observed that the largest tightening force leads to a larger initial a-spot radius and a smaller a-spot thickness after tightening due to the mechanical crushing: For 1000 N, the radius has evolved from 200 µm to 550 µm and the thickness from 400 µm to 50 µm during tightening, while the geometry remains almost unchanged for the three other cases.

This geometric modification of the a-spot due to tightening leads to different initial contact resistances, as can be observed on Figure 2.17, showing the evolution of the contact resistance for the different loads. At $t = 0$ µs, the well-known decreasing contact resistance with increasing tightening force [40] is observed, with 0.6 mΩ for $F = 1$ N and 0.125 mΩ for $F = 1000$ N.

As the temperature in the a-spot increases due to Joule heating (see Figure 2.18), the Young modulus and the yield strength of the material decrease. As a consequence, the stress in the material decreases with the temperature and the only way to maintain the mechanical equilibrium is to increase either the strain $\epsilon$ or the a-spot radius. In the elastic regime, the radius is kept constant and the increasing strain during crushing allows maintaining the stress and the reaction force constant despite the decreasing Young modulus. In the plastic regime, the decreasing stress is mainly compensated by an increasing a-spot surface.

On Figure 2.15 and Figure 2.16, it can be observed that during the first 0.3 µs the a-spot radius is constant but the thickness of the a-spot decreases which corresponds to the elastic deformation regime. At 0.4 µs, the elastoplastic transition can be clearly observed that results in a fast collapse of the a-spot thickness and a simultaneous increase of the a-spot radius for the 1 N, 10 N, and 100 N cases. This mechanical spreading of the a-spot radius due to the temperature increase has already been observed experimentally in [71] for a single contact spot subject to smaller current levels but during much larger time-scales, and appears to be very important to predict the correct maximum temperature in the materials. For $F = 1000$ N, no significant evolution of the a-spot geometry is

observed: The initial crushing of the a-spot due to the tightening force has decreased the contact resistance so much that Joule heating is not enough in this case to increase the temperature significantly and to generate the collapse of the mechanical properties. Indeed, the maximum temperatures that can be observed on Figure 2.18 at $t = 0.4\,\mu s$ are $1800\,K, 1700\,K, 900\,K$ and $400\,K$ for $F = 1\,N, 10\,N, 100\,N$ and $1000\,N$ respectively. As can be seen on Figure 2.12, the mechanical properties of steel seem to quickly collapse above a critical temperature $T \sim 700\,K$, which is consistent with the observed contact dynamics. For all the simulated cases, it appears that because of the mechanical flattening, the temperature never reaches the vaporization threshold, contrary to the cases with zero tightening force.

For $F = 1000\,N$, the contact resistance is almost constant during the D-wave, while for smaller forces the resistance exhibits an exponential growth until a maximum near the elastoplastic transition always located at $t = 0.4\,\mu s$. The exponential growth is due to the decreasing conductivity with temperature, and is always followed by a fast decrease of the reisistance due to the flattening dynamics of tha a-spot. Interestingly, for the lowest mechanical load, the exponential growth is exactly similar to the growth obtained with a zero tightening force (see Figure 2.14), as long as the temperature stays well below the fusion threshold.

The maximum resistances observed on Figure 2.17 seem higher for smaller tightening forces, and the final resistance values obtained at $t = 1\,\mu s$ are then lower than in the $1000\,N$ case.

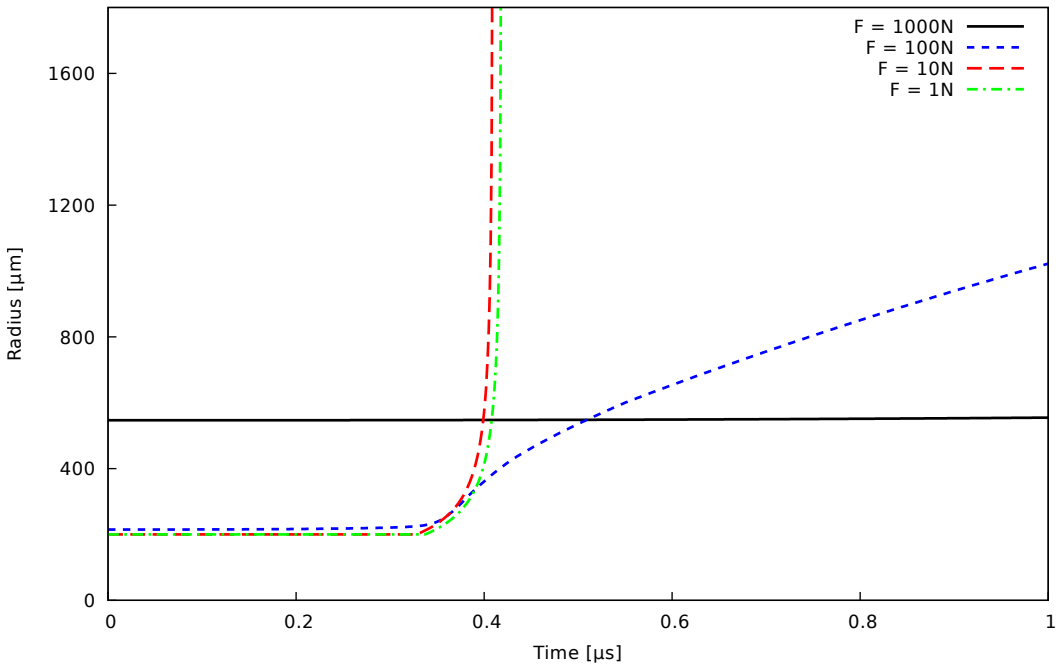


Figure 2.15: Evolution of the radius of a single a-spot contact subject to a D-wave current and four different constant tightening forces. The initial radius before tightening is $a_0 = 200\,\mu\text{m}$ and the thickness $l_0 = 400\,\mu\text{m}$.

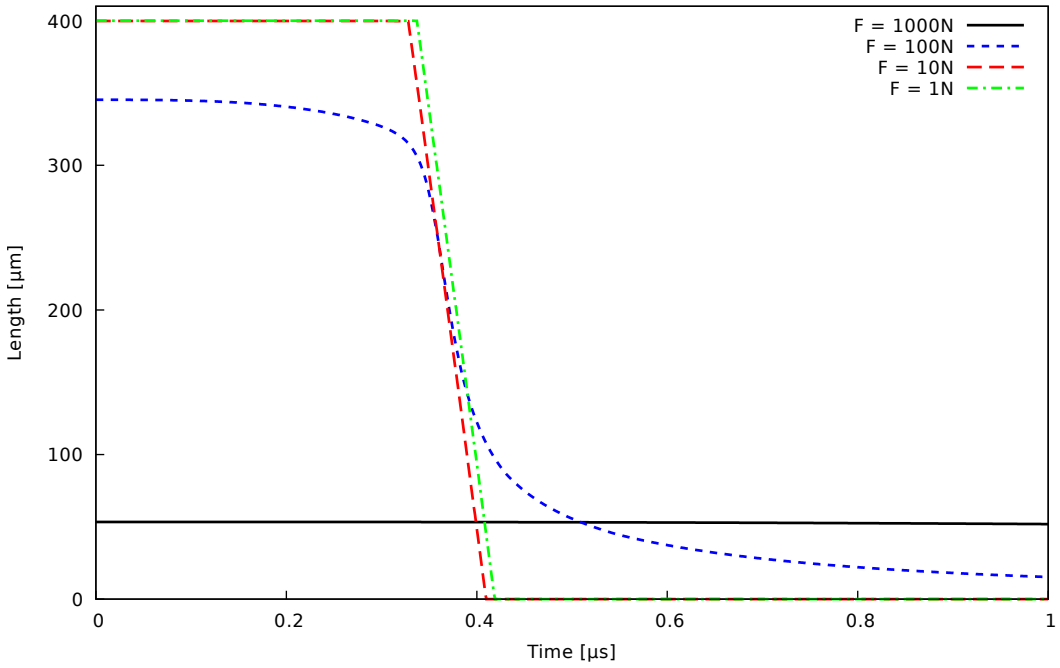


Figure 2.16: Evolution of the thickness of a single a-spot contact subject to a D-wave current and four different constant tightening forces. The initial radius before tightening is $a_0 = 200\,\mu\text{m}$ and the thickness $l_0 = 400\,\mu\text{m}$.

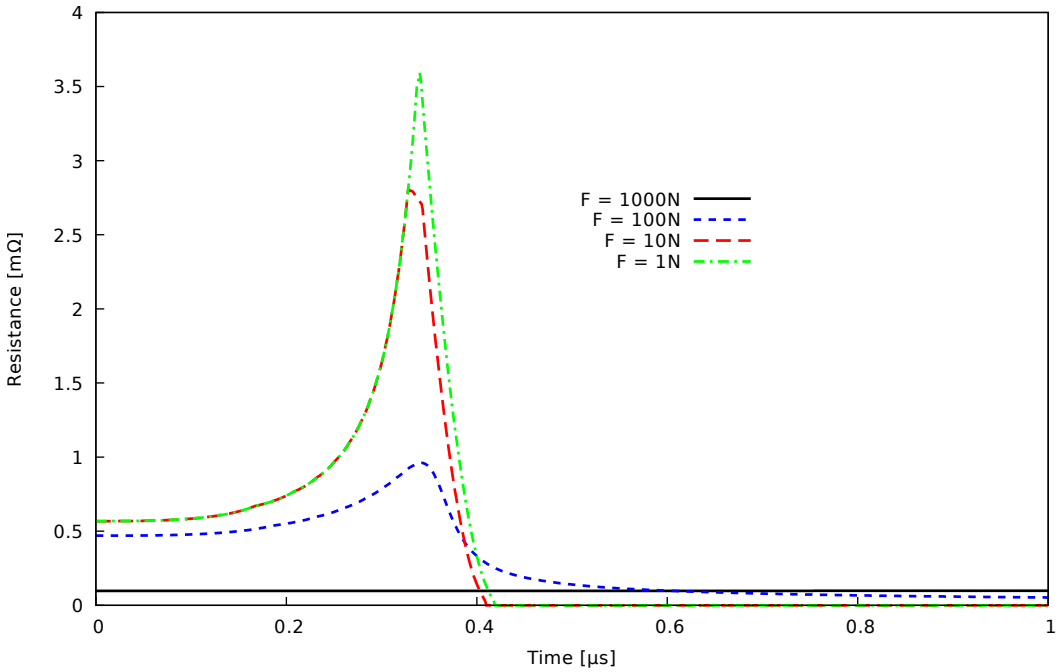


Figure 2.17: Evolution of the resistance of a contact a-spot of initial radius $a_0 = 200\,\mu m$ and thickness $l_0 = 400\,\mu m$ during a D-wave under constant mechanical load.

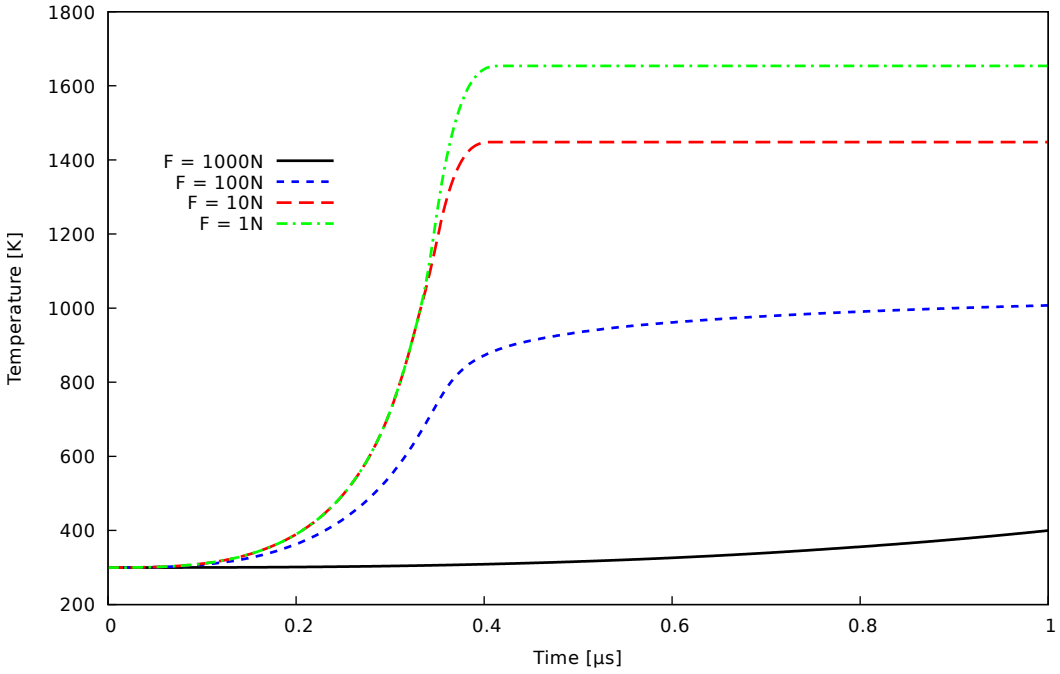


Figure 2.18: Evolution of the temperature in a single a-spot contact subject to a D-wave current and four different constant tightening forces. The initial radius before tightening is $a_0 = 200\,\mu m$ and the thickness $l_0 = 400\,\mu m$.

## 2.5 Conclusion

The 0D a-spot model presented in this study relies on geometric and physical simplifications that make it possible to solve rapidly the complex thermal, electrical and mechanical coupling that controls the evolution of a single a-spot subject to large current values representative of lightening stroke conditions.

For zero tightening forces, the thickness of the a-spot is kept constant, and the 0D model matches the 2D axisymmetric simulation results. In this case, a-spots subject to large currents may be completely vaporized, resulting in a fast increase of the contact resistance as soon as the boiling point is reached.

On the other hand, a tightening force may induce a mechanical flattening of the a-spot that prevents vaporization and lead to a non-monotonous resistance evolution: First, the resistance increases due to the Joule heating and the temperature decreasing conductivity of the material. A maximum resistance is reached when the temperature-dependent mechanical properties of the material start to collapse. This maximum contact resistance is then followed by a fast decrease due to the mechanical crushing of the a-spot, characterized by an increasing a-spot radius and a decreasing thickness.

This simplification of the description of the evolution of a single a-spot subject to a D-wave was aimed at providing a model that can be applied to a large number of a-spots, more representative of a realistic contact. The 0D model proposed was satisfying and efficient enough to consider such parametric studies. However, considering a-spots in parallel brings complex current distribution phenomena as well as mechanical behaviours that need to be assessed. An interaction model is then required, which is the purpose of the next chapter.

# Chapter 3

# Multiphysical modeling of multi-spot contacts

The purpose of this short chapter is to present how the multi-physical model of single a-spot contacts described in the previous chapter can be extended to contacts with several a-spots. This extension is not straightforward because of the different interaction phenomena between the a-spots. Three of them have been considered in this study.

The first one is the electrostatic interaction. The constriction resistance of an a-spot is related to the concentration of the current lines as the current diffuses from the bulk material to the a-spot. For a given voltage drop between the contact members, the total current flowing through a single a-spot decreases with a smaller radius, because of this concentration of the current lines. For two a-spots in parallel and for a given voltage drop, the total current also decreases when the a-spots are close to each other, because the current is distributed between them. Electrostatic interactions induce a local voltage around each of the a-spots that is lower than if they were far from each other, and therefore less current flows in each of them. This effect corresponds to an additional interaction term of the total contact resistance, that needs to be addressed.

The second interaction is related to current redistribution due to electrodynamic effects, such as capacitive currents in the contact, or inductive effects, that may play a significant role during the fast, transient current pulse of lightning stroke.

The third one is related to mechanical effects: if a tightening force is applied on a multi-spot contact, it should equal the sum of the individual loads sustained by each a-spot. Because these a-spots may differ in shape and size, their individual load may differ significantly from one a-spot to another, as well as their flattening dynamics. This may results in redistributions of the applied force, leading to a strong mechanical interaction. Moreover, as the tightening distance decreases, micro-peaks on the surface that were initially too small to interfere with the mating surface may form new a-spots, leading to further current redistributions and interactions with other a-spots.

In this chapter, to address the complexity related to multi-spot contacts, a short theoretical review and 3D electrostatic simulations are first presented to study into details the electrostatic interaction between a-spots. Electrodynamic effects are emphasized, as well as mechanical effects. Then, the selected modelling hypothesis are listed and a simple equivalent circuit model for a multi-spot contact is described. Finally, to examine the multi-spot dynamics in a very simple configuration, a contact with two micro-peaks is presented.

## 3.1 Interactions between a-spots

### 3.1.1 Electrostatic interactions

#### Analytical estimates of the electrostatic interaction term

Following on from the electrostatic analytical model for the resistance of a single a-spot, Holm [38] gives a method to approximate the resistance corresponding to a cluster of $n$ uniformly distributed a-spots, all having a circular shape and the same radius $a$. Moreover, this cluster is supposed to have of radial extension $r$, as represented on Figure 3.1. In this case the resistance of the cluster is given by Equation (3.1)

$$R_{A_r} = \frac{1}{\pi n a \sigma} \arctan \frac{\sqrt{l^2 - a^2}}{a} - 0.3 \frac{\sqrt{l^2 - a^2}}{\sigma n l^2} + \frac{1}{2\sigma r} \tag{3.1}$$

where $l$ is half the average distance between two a-spots. If $l$ is sufficiently large compared to $a$, this formula can be reduced to

$$R_{A_r} = \frac{1}{2na\sigma} + \frac{1}{2\sigma r} \tag{3.2}$$

This formula is interesting, since it can be easily seen that the first term is related to the resistance of $n$ constrictions in parallel, which is the expected resistance in the absence of electrostatic interactions between the current lines in the bulk material. Then the second term is representative of the electrostatic interactions between the a-spots. It corresponds to Holm's formula for the constriction resistance between the bulk material and the cluster of radius $r$, a radius that must be understood as an empirical parameter more than as the reality of a geometry.

Supposing $l \gg a$, the resistance is then approximatively the constriction resistance from the bulk to the the cluster in series with the resistance of $n$ parallel constriction resistances from the cluster to the a-spots. The hypotheses assumed in this approach are questionable, but this method provides an understanding of the origin of the additional interaction resistance.

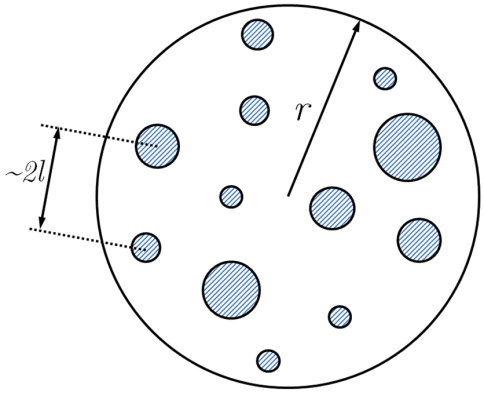


Figure 3.1: Schematic view of a cluster of circular a-spots of radius $r$ and with half average distance between the a-spots $l$

A widely accepted extension of Holm's work is Greenwood's formula (3.3), presented in [72], that estimates the resistance of a contact made of several a-spots in parallel:

$$R_{\mathrm{c}} = \frac{1}{2\sigma \sum a_i} + \frac{1}{\pi\sigma n^2} \sum_{i \neq j} \sum \frac{1}{d_{ij}} \tag{3.3}$$

In this equation $n$ is the number of a-spots, $a_i$ is the radius of the $i^{\mathrm{th}}$ a-spot, and $d_{ij}$ the distance between the centres of the a-spots $i$ and $j$. The first term is simply the resistance obtained by using Holm's formula for the a-spots in parallel. The second term is related to the interference of the current lines when a-spots are close to each other, and depend on the relative distances.

The demonstration of this formula is more sophisticated and more rigorous than the simple method proposed by Holm. Contrary to Holm's formula for a cluster of a-spots (3.2), it does not rely on an empirical radius $r$ and no hypothesis is made on the size of the a-spots.

Greenwood's formula can be viewed as a generalisation of Holm's work. Unfortunately, the precise values of the distances $d_{ij}$ between the a-spots in an actual contact are inaccessible. On the other hand, if the distances $d_{ij}$ are large enough, then the interaction term can be neglected, and the total resistance is then simply the resistances of all the a-spots in parallel. To determine in which conditions such an hypothesis is reasonable, a special effort has been made to study the interaction of several a-spots in 3D.

### 3D electrostatic simulations of several a-spots

The response of a single a-spot to high current levels is closely related to the spatial distribution of the current density and the Joule power. Besides the effect of the interaction of the current lines on the overall resistance, the question arises whether the distribution of current density inside a-spots can be significantly modified by the presence of other a-spots in its neighbourhood. If the a-spots are very distant from each other relatively to

their size, they can be considered as well separated, and the Holm's theory is valid. On the contrary, if they are close enough, the current lines going through them will interfere in the bulk material. To study into more details this purely electrostatic interaction between several a-spots, 3D numerical simulations have been performed with *Code_Saturne* [28], the EDF's open source CFD code, solving the current conservation equation (2.1) with a finite volume method in parallel.

Figure 3.2 shows a sliced view of the current density and the current lines going through two cylindrical aluminium a-spots having the same radius of 200 µm and a thickness $l = 80$ µm. It can be observed that the current lines between the two a-spots are influencing each other, resulting in the additional interaction resistance of Greenwood. Figure 3.3 shows the evolution of the electric resistance as a function of the separating distance between the two a-spots.

It seems clear that as soon as the distance between the a-spots is higher than about 20 times their radii, the resistance as converged to a threshold, meaning that the interaction becomes negligible, consistently with Holm's and Greenwood's models. The same conclusion arises looking at the Joule power distribution: when the distance between the a-spots is small, the current density and the Joule power distributions are modified compared to the axisymmetric distribution of an isolated a-spot, with reinforcements on the outer edge, and a screening effect on the inner edge (see Figure 3.3). This result has also been observed on 4 a-spots simulations, and it could have a significant influence on the thermo-electrical response of the contact if they are close enough. However, this effect on the distribution of current and Joule power quickly disappears with the separating distance: It can be observed on Figure 3.3 that purely axisymmetric Joule-power distributions are recovered when the separating distance is about 5 times the a-spot radius.

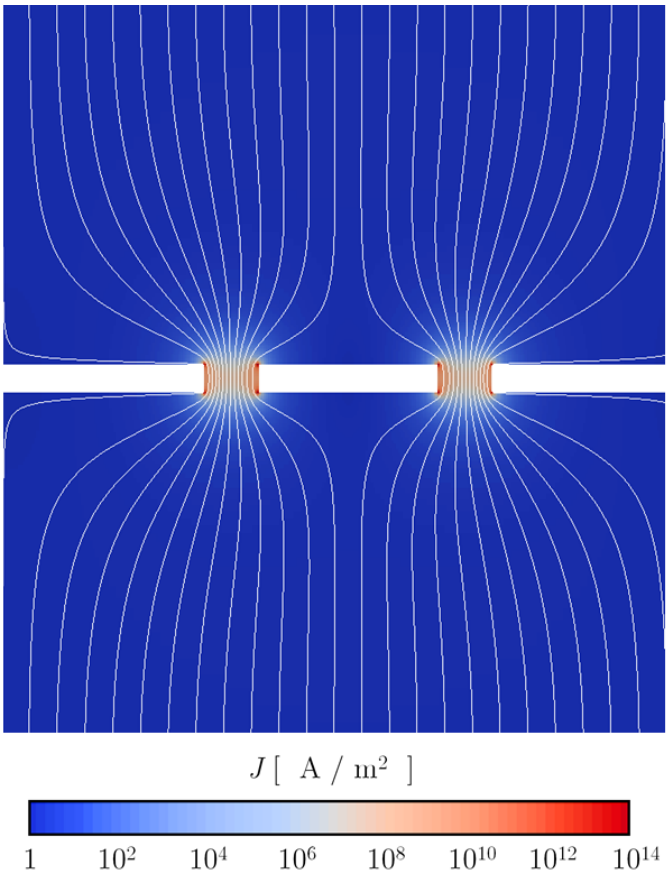


Figure 3.2: Sliced view of the current density profile and the current lines in two a-spots in parallel.

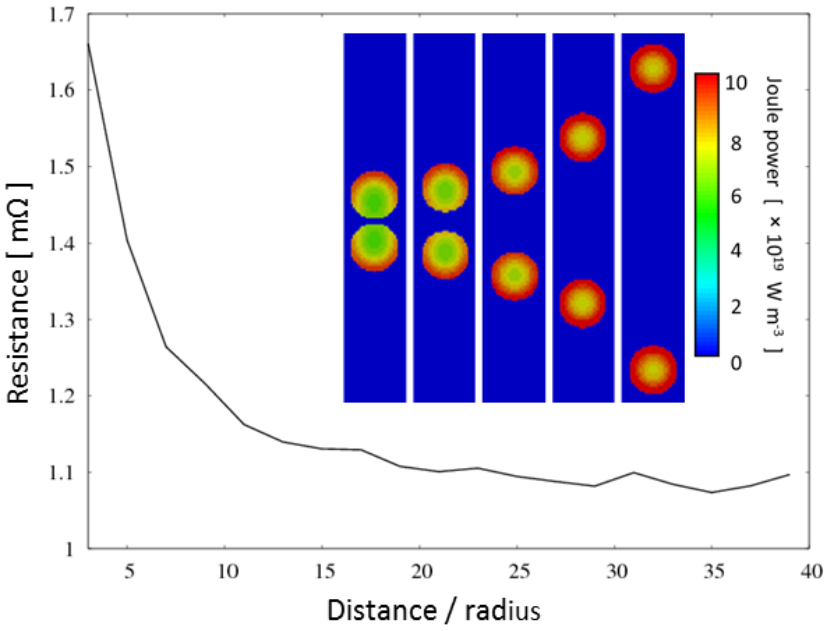


Figure 3.3: Total resistance of a two-spots contact and Joule power distribution as a function of the separating distance.

### 3.1.2 Electrodynamic interactions

If many a-spots of different size are present in a contact, the question arises whether the current distribution between them simply follows a resistive distribution, or whether inductive or capacitive effects may play a role. To evaluate inductive effects, it is useful to compare the typical size of the a-spots to the skin depth $\delta$ (m), given by Equation (3.4)

$$\delta = \sqrt{\frac{1}{\pi\sigma\mu f}} \tag{3.4}$$

where $f$ (Hz) is the frequency, $\mu$ ($\mathrm{H\,m^{-1}}$) the magnetic permeability and $\sigma$ ($\mathrm{S\,m^{-1}}$) the electric conductivity. In the context of the pulsed arc phase of a lightning stroke, the maximum frequency is of the order 1 MHz. For steel ($\sigma = 10^7\ \mathrm{S\,m^{-1}}$), it gives $\delta \simeq 160$ µm. In [73], it is reported from several numerical studies based on FEM (Finite Element Method) simulations that the inductive effect in an a-spot is dominant above a critical radius $a_c = 8\,\delta$. With the skin depth previously calculated, it can be assumed that as long as the radius of the a-spots is smaller than $a_c \simeq 1.3$ mm the inductive effects can be neglected as a first approximation.

The resistive description of the a-spots seems reasonable but should be questioned when considering the current redistributions between the a-spots, especially when the separating distances between them are larger than $a_c$. Moreover, it will be shown in the next chapters that the characteristic redistribution time-scales of the current between the a-spots during a lightning stroke can be of the order 100 ns. In this case $a_c$ is of the order 400 µm, and dealing with large a-spots and large separating distances would require taking into account inductive effects.

An other important electrodynamic effect is the capacitive currents due to the capacitance of the contact. To evaluate the relative importance of these currents, it is useful to compare the total conductive and capacitive currents that may flow in a contact subject to lightning stroke conditions. When an electric-field $E$ ($\mathrm{V\,m^{-1}}$) varies on a time-scale $dt$ (s), the capacitive current density is of the order $\varepsilon_0 E/dt$ ($\mathrm{A\,m^{-2}}$), where $\varepsilon_0$ ($\mathrm{F\,m^{-1}}$) is the vacuum permittivity. In aeronautic contacts subject to lightning stroke conditions, a reasonable value for the maximum electric-field is $E \simeq 10^8\ \mathrm{V\,m^{-1}}$. Considering the fast current redistributions between the a-spots ($dt \simeq 100$ ns), the capacitive current density obtained is of the order $10^4\ \mathrm{A\,m^{-2}}$. This value is much smaller than the typical conductive currents that may be encountered in a-spots, lying in the range $10^8\ \mathrm{A\,m^{-2}}$ to $10^{12}\ \mathrm{A\,m^{-2}}$. However, the capacitive currents may benefit from a much larger surface injection, since the ratio between the apparent surface area and the total section of the a-spots can be as high as $10^6$. Then, comparing the conductive and capacitive currents flowing in a contact amounts to comparing the conductivity of the metal relatively to $10^6\varepsilon_0/dt$. This term is of the order $90\ \mathrm{S\,m^{-1}}$, which means that capacitive currents are always very negligible on the time-scales of interest compared to conductive currents in the a-spots.

### 3.1.3 Mechanical interactions

The mechanical model presented in Section 2.3.2 needs to be adapted to the case of a rough surface with many micro-peaks. As shown by [40], considering the tightening of two rough surfaces is, for symmetry considerations, equivalent to the tightening of one rough surface to a perfectly flat plane. It is assumed in this work that the micro-peaks on a surface are cylinders, such that they may form cylindrical a-spots if they interfere with the mating surface, as represented on Figure 3.4.

Assuming that a mechanical load is imposed on the contact, the dichotomy algorithm on the separating distance previously described for a single a-spot may be employed. The only difference in the case of a multi-spot contact is that for each separating distance a different number of a-spots may be obtained. Each of them may have a different geometry, mechanical load and stress.

The dichotomy stops as soon as the sum of all the mechanical forces supported by the a-spots equals the total tightening force. As it will be seen in the next chapter, with this multi-spot mechanical model, increasing the mechanical load leads to an increasing number of a-spots, and a decreasing contact resistance. Compared to single a-spot contacts, multi-spot contacts are then subject to an important additional effect: the formation of new a-spots as the tightening distance decreases.

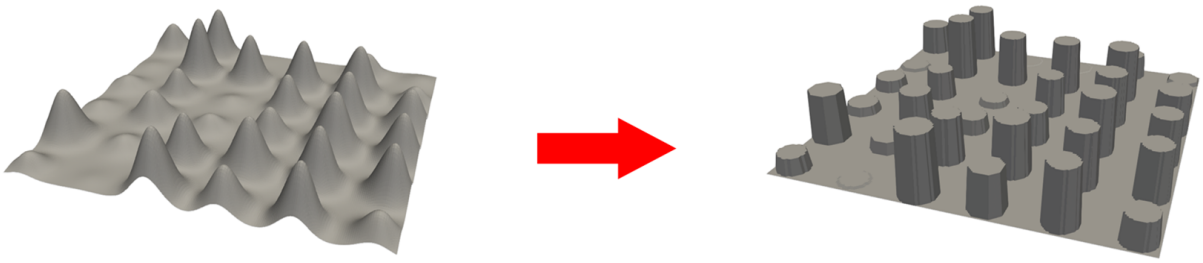

Figure 3.4: Representation of the micro-peaks on a surface. In the presented model, every micro-peak is modelled as a cylinder that may form cylindrical a-spots in the contact.

## 3.2 0D multi-spot model

### 3.2.1 Equivalent circuit model

The theories and the results of the 3D simulations presented in the previous sections clearly show that, if the a-spots are separated by 20 times their radii, the influence of the interaction of the current lines can be neglected. It can be assumed as a first approximation that this condition is realistic for a wide range of applications.

Moreover, it has been observed that if two a-spots are very close to each other, they almost behave as a single a-spot whose section is the sum of the sections of the two a-

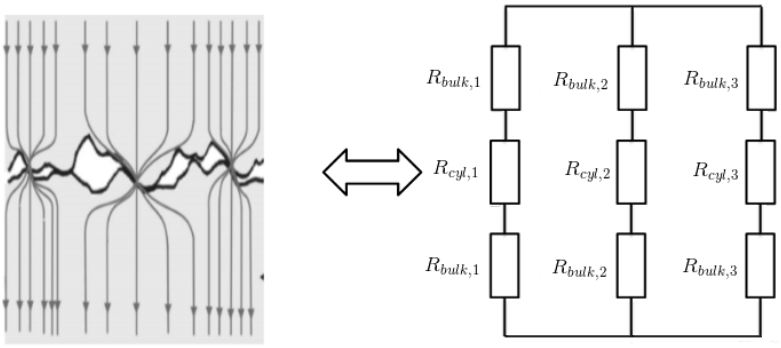


Figure 3.5: Equivalent scheme

spots. Then, neglecting this electrostatic interaction can be interpreted as a geometric simplification that models any packed group of a-spots that are close to each others into a single circular a-spot of equivalent section.

Finally, since there is practically no hope to fully characterize the precise spatial distribution and distances between the a-spots in a realistic contact, trying to take into account these unknown geometric properties would bring either unnecessary complexity or large uncertainties to the model. For these reasons, the choice has been made in the following to neglect the modification of the current density distribution and the additional resistance terms due to the electrostatic interactions between a-spots.

A contact with many a-spots is then equivalent to an electrical circuit where a-spots can be seen as resistances in parallel, as presented in Figure 3.5. The current $I_i$ (A) in the $i^{th}$ a-spot of a contact can be calculated as a function of the total contact resistance $R_\mathrm{c}$ ($\Omega$) and the total imposed current $I$ (A) following Equation (3.5).

As shown previously, capacitive effects can be neglected in contacts and no capacitor has to be included in the circuit model. However, inductive effects may play a significant role in some particular cases with large a-spots or a-spots separated by large distances compared to $\simeq$ 1 mm. In such a case, inductances should be added to the simplified electrical model of Figure 3.5, but the geometric parameters needed to evaluate those inductances would require a precise knowledge of the geometry. To avoid this difficulty, it has been imposed that the contacts under consideration in the next chapters be “small enough" to neglect the inductive redistribution phenomena as a first approximation.

$$I_i = \frac{R_\mathrm{c}}{R_{\mathrm{Holm},i} + R_{\mathrm{cyl},i}} \cdot I \tag{3.5}$$

### 3.2.2 Two a-spots under constant tightening distance

To illustrate the complex interaction between a-spots in a contact, it is useful to first consider the simplest configuration of a contact with two steel a-spots of different sizes.

Figure 3.6 shows the evolution of the radii of two a-spots in a contact with constant tightening distance. One of the a-spot has an initial 200 µm radius and a constant 400 µm length, while the other one has an initial 100 µm radius and a constant 200 µm length, both having the same material properties as the single a-spot studied in Chapter 2.

The observed dynamics is very similar to the case of a single a-spot alone. Interesting is to note that in this case the two a-spots are almost vaporized at the same time, while the current density and the Joule power is higher in the smallest a-spot initially. The explanation relies in the decreasing electric conductivity with the temperature, that induces a faster increase of the resistance of the smallest a-spot. Then a progressive current redistribution takes place from the smallest to the biggest a-spot. As a consequence, the evolution of the total resistance only shows one slope discontinuity (see Figure 3.7), corresponding to the more or less simultaneous moments where both a-spots start to boil. During the vaporization phase, current redistributions may also take place leading to the full vaporization of the two a-spots at the same time.

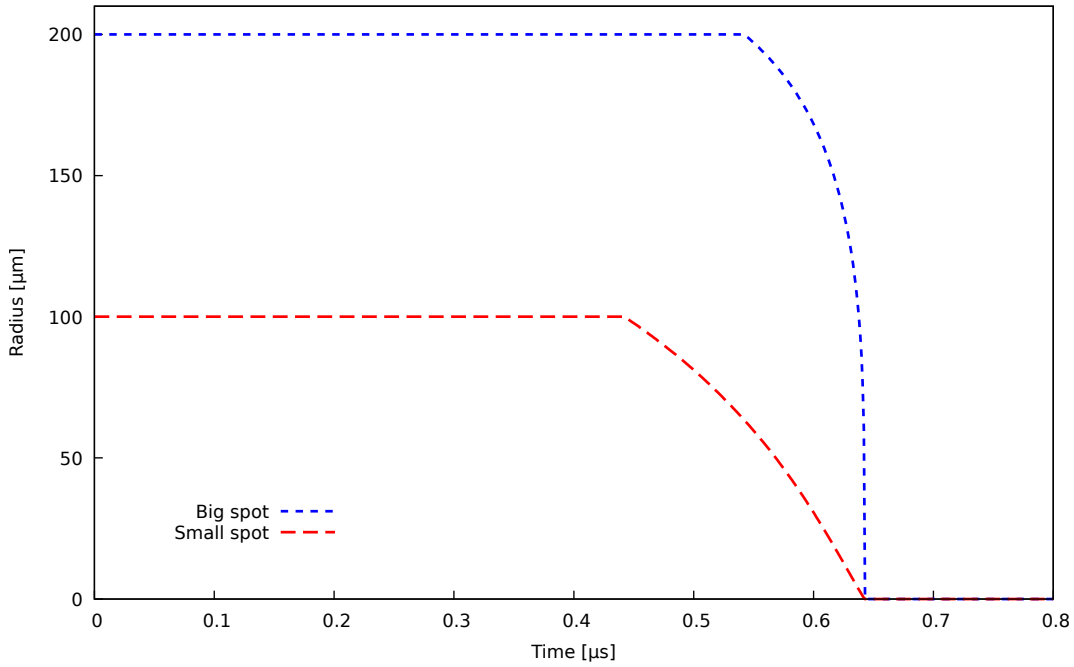


Figure 3.6: Radius of two steel a-spots in parallel subject to a D-wave. The biggest a-spot as an initial 200 µm radius and a constant 400 µm length, while the other has an initial 100 µm radius and a constant 200 µm length.

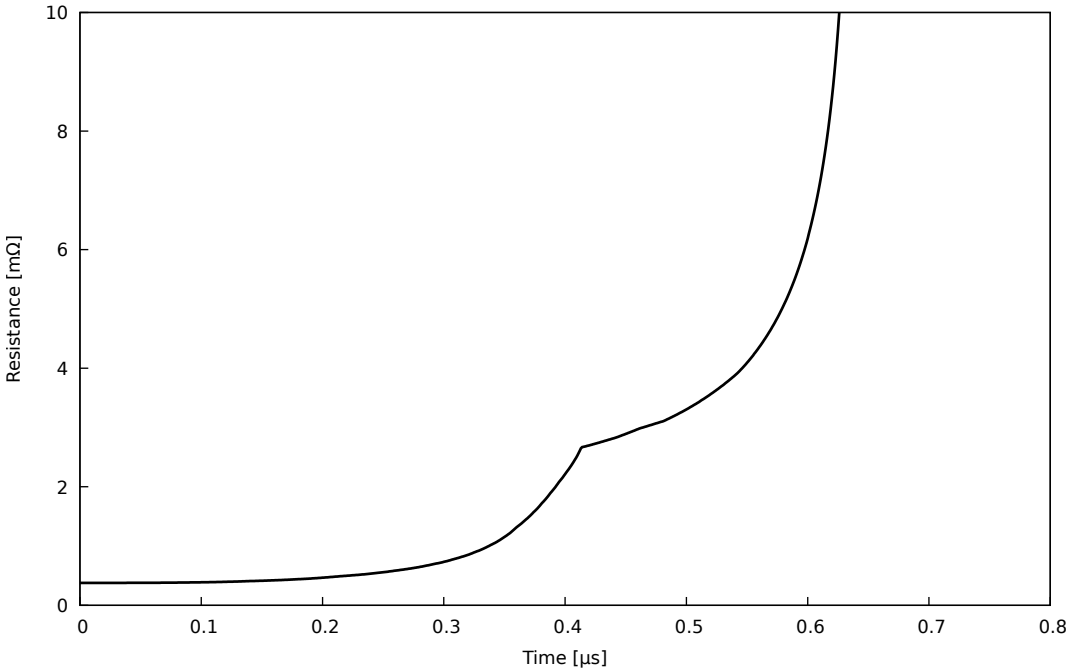


Figure 3.7: Resistance of two a-spots in parallel subject to a D-wave. The biggest a-spot as an initial 200 µm radius and a constant 400 µm length, while the other has an initial 100 µm radius and a constant 200 µm length.

### 3.2.3 Two micro-peaks under constant load

More interesting is the case of a contact with two micro-peaks of different sizes subject to a constant load and a D-wave. In this case, depending on the tightening force and the geometry of the micro-peaks, there can initially be a single a-spot or two a-spots : The biggest micro-peak might hold the mechanical load alone, or be tightened enough so that the second micro-peak be participating to the contact as a second a-spot. Because of the decrease of mechanical properties with temperature, the second micro-peaks can also be reached after some time, even though it is not initially participating to the contact. Therefore, the geometry and the number of a-spots may change during the current wave.

Figure 3.8 shows the evolution of the resistance of such a contact with a constant tightening force of 100 N for different ratios $r = a_2/a_1$, where $a_1$ is the radius of the first, biggest micro-peak and $a_2$ the radius of the second, smallest micro-peak. In the following the biggest micro-peak has always a radius $a_1 = 200\,\mu\text{m}$, and for both peaks their length is equal to their diameter. Results are shown for $r = 0$, 0.6, 0.7, 0.8 and 0.9.

The case $r = 0$ corresponds to a single a-spot contact, with the biggest micro-peak alone. For cases $r = 0$, 0.6, 0.7 and 0.8, the biggest micro-peak is initially alone, but collapses to form a second a-spot later during a D-wave. The contact resistance at $t = 0\,\mu\text{s}$ starts exactly at the same value of $0.47\,\text{m}\Omega$ because until the first micro-peak collapses, the contact situation is exactly the same as case $r = 0$. Conversely, for the case $r = 0.9$,

the initial contact resistance is smaller because the second micro-peak is already forming a second a-spot, since it is higher than the size of the tightened first micro-peak.

At first the resistance for the cases $r = 0.6$, 0.7 and 0.8 increases due to the temperature increase inside the a-spot. Then the collapse of the mechanical properties occurs between 0.3 µs and 0.4 µs, and is followed by a flattening dynamics and a decrease of the contact resistance. This fast collapse of the resistance due to flattening is stopped as soon as the second micro-peak interferes with the mating surface and supports part of the load. This second a-spot is touched sooner when the corresponding micro-peak is larger. Then, part of the current flows through the second a-spot whose temperature increase induces again an increase of the total resistance. Finally, as soon as the mechanical properties in the second a-spot collapse, a new flattening dynamics follows resulting in a fast decrease of the contact resistance. A larger second a-spot leads to a slower temperature increase and a later final mechanical collapse.

For the case $r = 0.9$, the two micro-peaks participate to the electrical conduction and mechanical load since the beginning of the D-wave and the total resistance exhibits a similar non-monotonous evolution as in a single a-spot case, for the same reason that two a-spots under constant load follow the same behaviour as a single a-spot : Current redistribution insures both a-spots increase in temperature almost homogeneously and collapses at the same time.

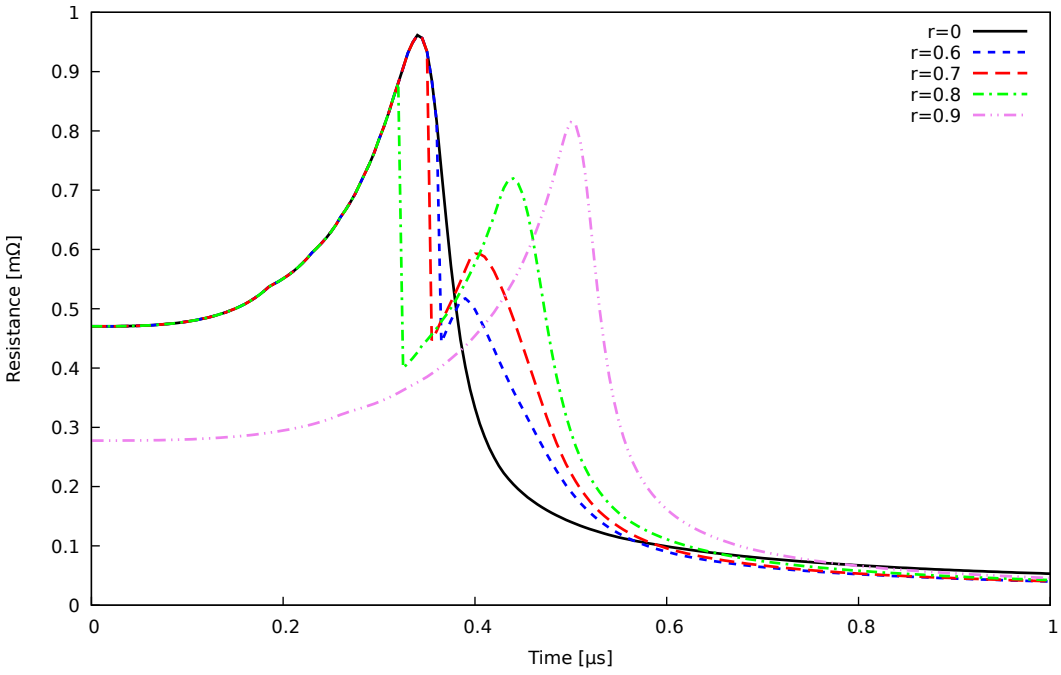


Figure 3.8: Resistance of a contact subject to a D-wave, with two micro-peaks under a constant load $F = 100$ N for different ratios $r$ of the radius of the micro-peaks.

## 3.3 Conclusion

The first section of this chapter aimed at modelling the current distribution through a-spots in parallel. After investigating the possible effects of interaction of the current lines when a-spots are close to each other, the justified choice has been made to neglect these effects in a spirit of simplification.

Following the same method as in Chapter 2 where we considered the two opposite cases of a contact under constant separating distance, and a contact under constant mechanical load, the dynamics of current distributions and the multi-physical coupled behaviour have been observed for the simple case of two a-spots contacts.

Without mechanical load, it appears that even if the a-spots do not have the same size, their temperatures rise and their radii decrease by vaporization together, because of a dynamic current re-distribution.

In the case of a constant mechanical load, the temperature of the first micro-peak in contact rises until its fast mechanical collapse. Contrary to the case of a single a-spot contact, this fall is stopped by the presence of the second micro-peak that starts bearing part of the mechanical load and imposed current.

The evolution of the value of the total resistance of such contacts, which is the main value of interest and the easiest to measure in practice, shows similar patterns than the evolution of a single a-spot contact subject to a D-wave. Only in the case where smaller micro-peaks can be reached to form new a-spots can we directly observe the effect of micro-peaks distribution This effect is besides partly due to the chosen cylindrical model of the a-spots that lead to sharp decline of the total resistance when a new a-spot is formed.

The question arises as to weather such dynamics can be observed for a realistic surface composed of a great number of a-spots, which will be assessed in Chapter 4.

# Chapter 4

# Realistic contact subject to a lightning wave

In this chapter the 0D multi-spot model has been used to study into details the evolution of the resistance and the a-spots distribution in a realistic contact subject to a lightning current. To take into account the complex micro-geometry of a surface, a statistical description is introduced, where the heights of a fixed number of micro-peaks follow a Gaussian probability law. The main advantages of the statistical description considered is its relative simplicity and the fact that it only depends on a small number of parameters that can be obtained from profilometry experiments.

The main goal in this chapter is to gain insight into the influence of surface parameters on the dynamics of realistic contacts subject lightning stroke. To that intend, the micro-peaks distribution of a given interface is assumed to follow a Gaussian distribution that makes it possible to rely on a few measurable roughness parameters, which are presented, for the description of the distribution. This modelling allows to perform an electrostatic confirmation with the study of the contcat resistance as function of the applied mechanical load between two contact members, using a comparison with Schoft's work [40]. Then, a parametric study is performed to asses the importance of roughness parameters on the behaviour of a contact suject to a D-wawe, for both cases of a contact under constant tightening distance and constant tightening load.

## 4.1 Gaussian surface model

The number, the shape and the size of the micro-peaks on a surface may be stochastic and depend on material properties. This initial micro-peak distribution is complex to address, since it depends on the detailed industrial processing of the surface, including machining, surface treatments and mechanical wear in operating conditions. Modelling a realistic surface micro-geometry is still a complex and open problem. A consensual way

to describe a surface roughness is to consider it as a distribution of self-similar patterns of different sizes, as in the fractal surface models [74] [75]. All these models result in a statistical description of the micro-geometry.

From an experimental point of view, different profilometry technologies may be employed to characterize a surface. If the mean of the measurement can differ (laser, solid probe...), the idea is always to measure the fluctuations of the height of the surface. Several ISO norms may be used to define the main parameters of a surface's state. In the ISO 4787 norm, a primary profile is first defined from the measured profile by removing the short wavelength modes, thanks to a low-pass electronic filter [76]. The top of Figure 4.1 shows a schematic of the primary profile of a surface. A root mean square method is then used to define a mean line corresponding to the local mean value of the surface height. This mean line depends on the integration length, that must be long compared to the size of the asperities, but small compared to the macroscopic size of the fluctuations. The waviness is then defined by the height fluctuation of the mean line, or equivalently to the large wavelength modes of the profile trace. The roughness profile is obtained with a high-pass filter, the waviness component being removed from the profile, as presented on the bottom of Figure 4.1. This roughness profile allows to define several parameters reflecting the degree of the fluctuations, corresponding to different moments of the height distribution. For example:

- The mean micro-peak height $R_{\mathrm{a}}$ (m), defined as the arithmetical mean of the absolute values of the profile deviations from the mean line of the roughness profile.
- The root mean square of the height distribution $R_{\mathrm{q}}$ (m) is the root mean square of the profile deviations from the mean line.

$$m = \frac{1}{L}\int_0^L z \, \mathrm{d}x \tag{4.1}$$

$$R_{\mathrm{a}} = \frac{1}{L}\int_0^L |z - m| \, \mathrm{d}x \tag{4.2}$$

$$R_{\mathrm{q}}{}^2 = \frac{1}{L}\int_0^L (z - m)^2 \, \mathrm{d}x \tag{4.3}$$

These two parameters give information on the dispersion of the fluctuations around the mean level of a surface. They are used as macroscopic parameters for a wide range of engineering problems that require to take the microscopic geometry of the surface into account. For example the laws of mechanical friction between two bodies, the laws of friction between a fluid and a wall, or the laws of light emission, reflection or absorption of a surface are often reduced to formulas directly involving $R_{\mathrm{q}}$. In the same way, the main goal of this chapter is to answer the question whether or not, for a given contact

resistance, the roughness parameters of the surfaces may have a strong influence on the dynamics of a multi-spot contact subject to lightning stroke conditions.

For electric contacts, these parameters naturally give insight on the size and the distribution of the potential a-spots. Intuitively, the highest points of the roughness profile can be seen as micro-peaks that may form a-spots. However, considering for example the shape of the roughness profile presented on Figure 4.1, it seems rather difficult to clearly identify what the micro-peaks are on this surface. Indeed, because of the fractal nature of the surface profile, there is a convolution of many summits of different sizes, and it does not seem possible to isolate a micro-peak from the others. In the same way that filtering operations are needed to remove very high or very low wavelength modes, not representative of the surface micro-geometry, some procedure is required to define unequivocally the micro-peaks on a surface. For example in [40], a profile value is considered to be a profile peak if the profile line passes over a given level $c_1$ and afterwards falls short under a level $c_2$, placed around the mean line. Figure 4.2 shows an example of the identification of micro-peaks on a roughness profile according to this methodology.

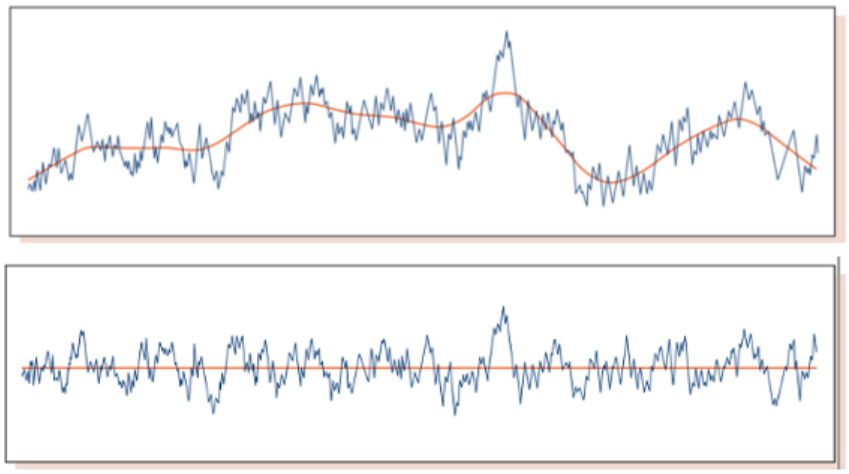

Figure 4.1: Primary profile and mean line (top), and roughness profile with its mean line (bottom). Taken from [76].

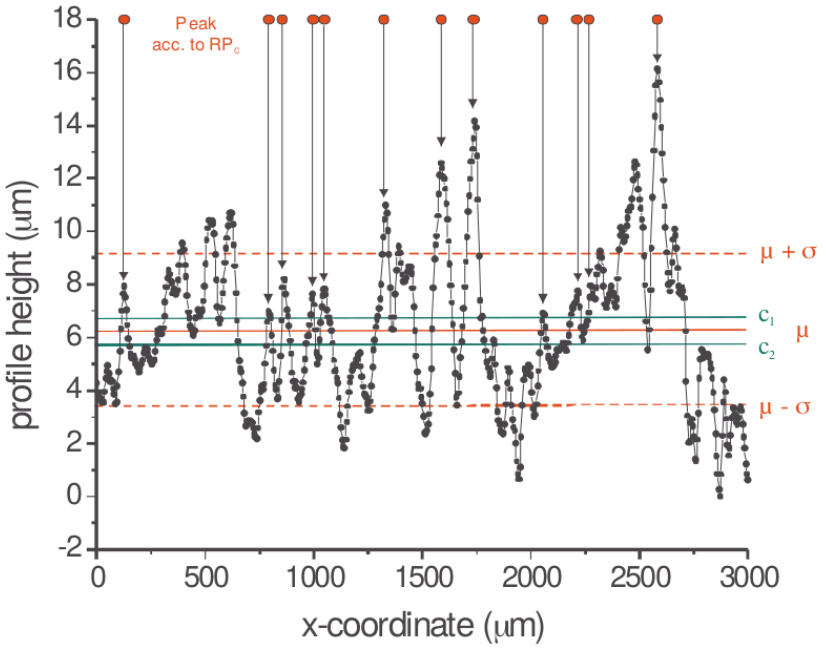


Figure 4.2: 2-dimensional surface trace of brushed Al-busbar joints with profile peaks. Taken from [40].

With this micro-peak identification method, and using laser profilometry, S. Schoft [40] have measured the roughness parameters $R_\mathrm{a}$ and $R_\mathrm{q}$ of an aluminium brushed surface, and the number of summits per unit of surface $N_\mathrm{s}$ ($\mathrm{m}^{-2}$). In this case the measured profile exhibits a height distribution that is close to a Gaussian probability function:

$$\varphi\,(z) = \frac{1}{\sqrt{2\pi}R_\mathrm{q}} \exp\left[-\frac{1}{2}\left(\frac{z - R_\mathrm{a}}{R_\mathrm{q}}\right)^2\right] \tag{4.4}$$

In order to simplify the problem, it is noticed in [40] that the height of the micro-peaks on surfaces are stochastically independent. As a consequence, due to symmetry considerations, the mechanical contact of two surfaces with same roughness parameters $R_\mathrm{a}$ and $R_\mathrm{q}$ is equivalent to the contact between a perfectly flat plane with a single rough surface, with parameters $R'_\mathrm{a} = 2R_\mathrm{a}$ and $R'_\mathrm{q} = \sqrt{2}R_\mathrm{q}$.

To model the micro-geometry of the surfaces in a contact, the choice has been made in this work to keep the same model as in [40], replacing the spherical micro-peaks by cylindrical ones. Then, a surface has a given number of cylindrical micro-peaks per unit surface area $N_\mathrm{s}$, which height distribution follows a Gaussian probability function with parameters $R'_\mathrm{a}$ and $R'_\mathrm{q}$, that are replaced in the following by $R_\mathrm{a}$ and $R_\mathrm{q}$ to avoid heavy notations.

Besides, the hypothesis has been made that the height of a cylindrical micro-peak, $l$, should be proportional to its radius $a$. The aspect ratio $l/(2a)$ may change from one surface to another, but looking at most STM images (Scanning Tunneling Microscop) and

multiscale roughness descriptions performed in the litterature with fractal models [74] [75], a reasonnable assumption is that $l/(2a)$ is close to one. This assumption is justified for physical reasons: very high and narrow micro-peaks barely bear the mechanical constraints compared to wider ones and are prone to mechanical damage. On the other hand, very wide, flat asperities are better representative of large surface fluctuations rather than representative of the micro-peak distribution. The mean ratio $l/(2a)$ of the micro-peaks can be seen as a free parameter of the model, that has been put to one in the rest of this study, meaning that for all the micro-peaks the radius is initially, before any tightening, half the height.

## 4.2 Electrostatic aluminium contact under increasing load

As a first application, the Gaussian surface model has been employed to study the evolution of the low-level resistance of a contact subject to an increasing tightening load. Direct comparisons can be made with Schoft's work, where micro-peaks are modelled by spheres. The contact under consideration has been generated based on Schoft's measurements, with the following surface parameters: $R_\mathrm{a} = 12.6\,\mu\mathrm{m}$, $R_\mathrm{q} = 4.1\,\mu\mathrm{m}$ and a total number of peak $N_\mathrm{s} = 38\,000$. The conducting metal was chosen to be aluminium in order to be as close as possible to Schoft's conditions.

Figure 4.3 reveals an important and non-linear resistance decrease from 7 µΩ to 0.2 µΩ as the tightening force increases from 0 N to 25 kN. It can be clearly seen on Figure 4.4 that this resistance decrease with the tightening force is mainly due to the increasing number of a-spots in the contact. Together with the increasing number of a-spots, the average a-spot radius decreases because the new a-spots appearing correspond to smaller and smaller micro-peaks that where initially not interfering.

Those results are very similar to those obtained by Schoft in similar conditions (see Figure 12 in [40]). However, a significant difference remains for small tightening forces concerning the average a-spot radius. Indeed, accordingly to the Hertzian elastic contact theory, for small loads $F$ (N), the surface of contact between a spherical a-spot and the mating plane surface increases continuously starting from 0, and is proportional to $F^{2/3}$. On the contrary, with cylindrical a-spots, the surface of contact does not change significantly during the elastic deformation regime, and the effect of averaging over smaller a-spots as the load increases induces a decreasing average radius. Then the increasing average a-spot radius observed in the spherical a-spot model for small loads does not appear with the cylindrical a-spot model presented here. Even though simple and very satisfying for important loads, this model should be considered cautiously when considering small loads.

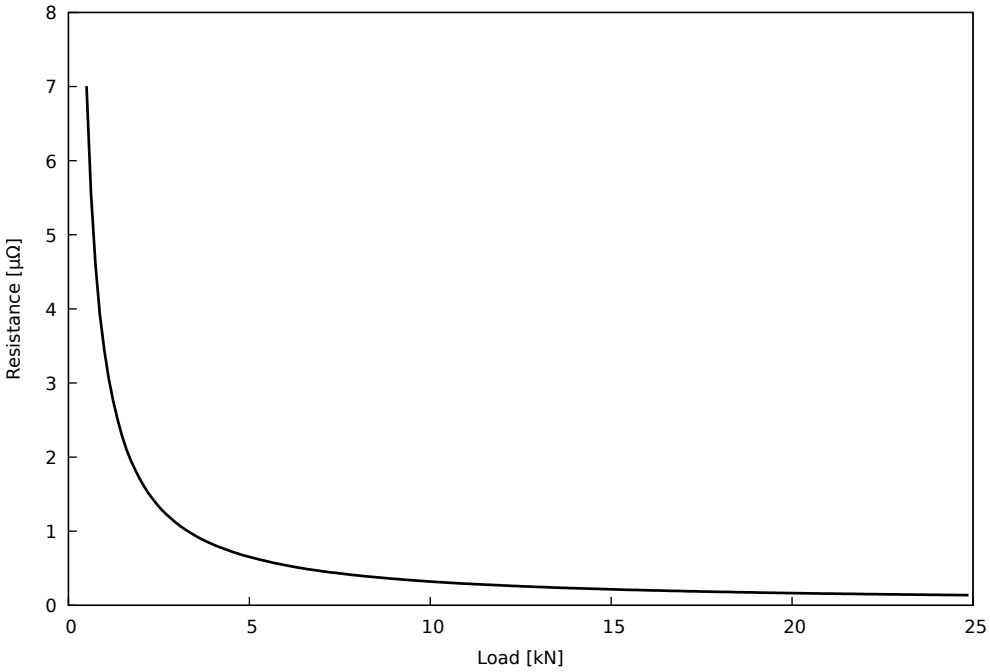


Figure 4.3: Evolution of the contact resistance as a function of the tightening force, for cylindrical aluminium micro-peaks, $R_a = 12.6\,\mu m$, $R_q = 4.1\,\mu m$, $N_s = 38\,000$.

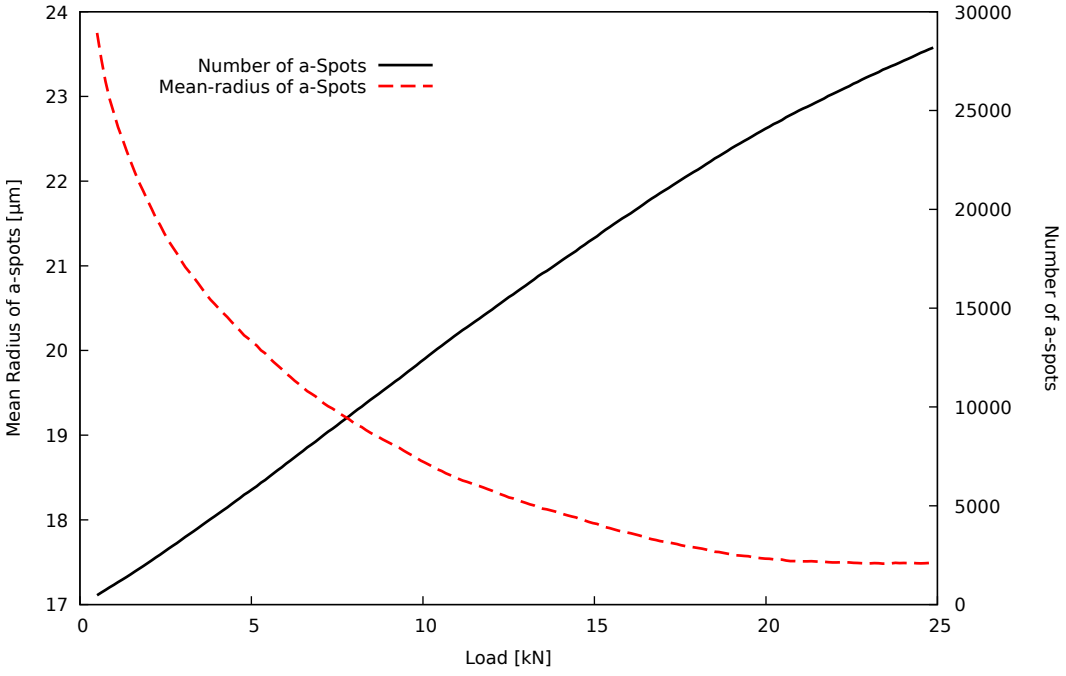


Figure 4.4: Evolution of the number and mean radius of a-spots in a contact as a function of the tightening force, for cylindrical aluminium micro-peaks, $R_a = 12.6\,\mu m$, $R_q = 4.1\,\mu m$, $N_s = 38\,000$.

## 4.3 Realistic multi-spot contact dynamics

The Gaussian surface model previously described is used to simulate the dynamics of a realistic contact subject to a lightning stroke. The main goal in this section is to study the influence of the roughness parameters for a given contact resistance.

At the beginning of this study, it was not clear how the roughness parameters would influence the contact dynamics, and the possibility of a strong dependence with the micro-geometry was not excluded. Such a situation would have been an important pitfall, meaning that the non-linear evolution at high current of a contact strongly depends on inaccessible micro-geometric details. However, it appears that important regularities can be observed in the contact dynamics for different roughness parameters. This observation gives confidence in the usefulness of the modelling strategy adopted.

A surface of $40\,\mathrm{mm}^2$ has been considered, which is approximatively the apparent surface expected for the contact between a screw and a bolt in typical aeronautic fastened assemblies. Different values of the mean value $R_\mathrm{a}$ and the standard deviation $R_\mathrm{q}$ of the Gaussian function are considered, but the number of micro-peaks per unit area is fixed to $26.3\,\mathrm{mm}^{-2}$, based on the measurements performed in [40]. Therefore, the contact has initially around 1000 micro-peaks, with an average distance from each other of $200\,\mu\mathrm{m}$.

Because one of the questions was to answer whether or not the contact resistance is a parameter that is, on its own, enough to predict the evolution of a contact subject to high currents, the initial tightening distance has been determined with the dichotomy algorithm to set the initial contact resistance to $0.1\,\mathrm{m}\Omega$ in all the presented results. Then, the different values of $R_\mathrm{a}$ and $R_\mathrm{q}$ considered correspond to the same initial resistance but to different tightening forces.

Two cases are considered: In the first case, the separating distance between the surfaces is kept constant, which could occur for example if most of the initial load is supported by an interface insulating material such as an oxide layer or sealant. In the second case, the initial load is kept constant and the a-spots support the tightening force, which can lead to flattening dynamics.

Because of the random generation of the micro-peaks from the Gaussian probability law, the results are not deterministic and different seeds for the random number generator may result in different initial a-spots distributions and slightly different results. This uncertainty on the initial micro-geometry is an unavoidable consequence of the statistical description of the surface roughness. Variations in the results were found to fluctuate by 10 % of the mean results, but in order to focus on the most significant tendencies the presented results are the average of 100 simulations performed with different seeds for the random number generator used to determine the initial micro-peak distribution.

### 4.3.1 Multi-spot contact with constant length

Figure 4.5 shows the evolution of the contact resistance subject to a D-wave for five distinct roughness values: $R_a$ is set to 12 µm in all cases, and $R_q$ varies in the range 2 µm to 6 µm. The tightening forces computed to set the initial contact resistance to 0.1 mΩ for the different values of $R_q$ are given in Table 4.1.

The dynamics is very similar to the one obtained with a single a-spot contact with constant separating distance (Figure 2.9). It appears that for all the a-spots, the resistance first increases due to the decreasing conductivity with temperature. As soon as the temperature of the a-spots reaches the boiling point, the time derivative of the resistance suddenly goes down in the bi-phasic liquid-vapour region where the temperature remains constant. Quickly, a vaporization front propagates from the periphery of the a-spots to their center and the total resistance increases exponentially.

Interesting is to notice on Figure 4.5 that the surface parameter $R_q$ seems to have the same influence as the radius of the a-spot in the case of a single a-spot contact: A larger $R_q$ means a longer time to reach the boiling point in the a-spots and a slower increase of the total resistance of the contact. The reason is a larger dispersion of the a-spot radii around the average radius for larger values of $R_q$. Consequently, the probability to have micro-peaks significantly larger than the average radius is higher for larger $R_q$. Because the largest micro-peaks support most of the load during tightening, the contribution of the a-spots with larger radii to the total conductance is dominant over smaller a-spots. Then a larger $R_q$ means larger a-spots in the contact with the same influence on average as a larger radius for a single a-spot contact.

The fact that this multi-spot contact has a dynamics very similar to a single a-spot contact was already observed in Chapter 3 for the case of two a-spots, and is due to the current re-distribution as the temperature of the a-spots rises. According to Equation 3.5, the current density in the $i^{\text{th}}$ a-spot $j_i$ (A m$^{-2}$) and corresponding Joule power density $P_i$ (W/m$^3$) are given by equations 4.5 and 4.6 respectively,

$$j_i = \frac{2\sigma_i U}{2l_i + \pi a_i} \tag{4.5}$$

$$P_i = \frac{4\sigma_i U^2}{(2l_i + \pi a_i)^2} \tag{4.6}$$

where $U$ (V) is the voltage difference applied to the contact, $l_i$ and $a_i$ the length and radius, and $\sigma_i$ (S m$^{-1}$) the temperature decreasing electric conductivity of the a-spot. It can be deduced that, initially, smaller a-spots are subject to larger current densities and larger Joule powers. Small a-spots should reach the boiling point and vaporize much before the largest a-spots, resulting in important modifications of the total resistance dynamics compared to a single a-spot situation. However, if a particular a-spot is smaller

than the others and subject to a more intense Joule power, the faster temperature increase would increase its resistance faster and the current would be redistributed to the other a-spots. In the end, only a small current redistribution between the largest a-spots occurs during the lightning wave that results in the near "single a-spot dynamics" observed.

This is revealed by Figure 4.6, showing the cumulated fraction of the total current in the different a-spots sorted by decreasing size for the case $R_q = 4\,\mu m$. It can be observed that all the lightning current flows into the 100 largest a-spots. The maximum slope is obtained for the first a-spots because they are significantly larger than the average radius and their contribution to the conduction is relatively important. The following a-spots are closer and closer to the average radius value, which leads to an almost linear increase, since each micro-peak has almost the same conducting effect as the previous of this index.

The evolution of the current fractions reveals a moderated redistribution with more and more current flowing through the largest a-spots, due a faster resistance increase and vaporization of the smaller ones.

| $R_q$ (µm) | 2 | 3 | 4 | 5 | 6 |
|---|---|---|---|---|---|
| Tightening Force (N) | 16.37 | 19.03 | 21.87 | 24.84 | 27.84 |

Table 4.1: Tightening forces needed to reach $0.1\,m\Omega$ in a $40\,mm^2$ contact with roughness parameters $N_s = 26.3\,mm^{-2}$, $R_a = 12\,\mu m$ and different values of $R_q$.

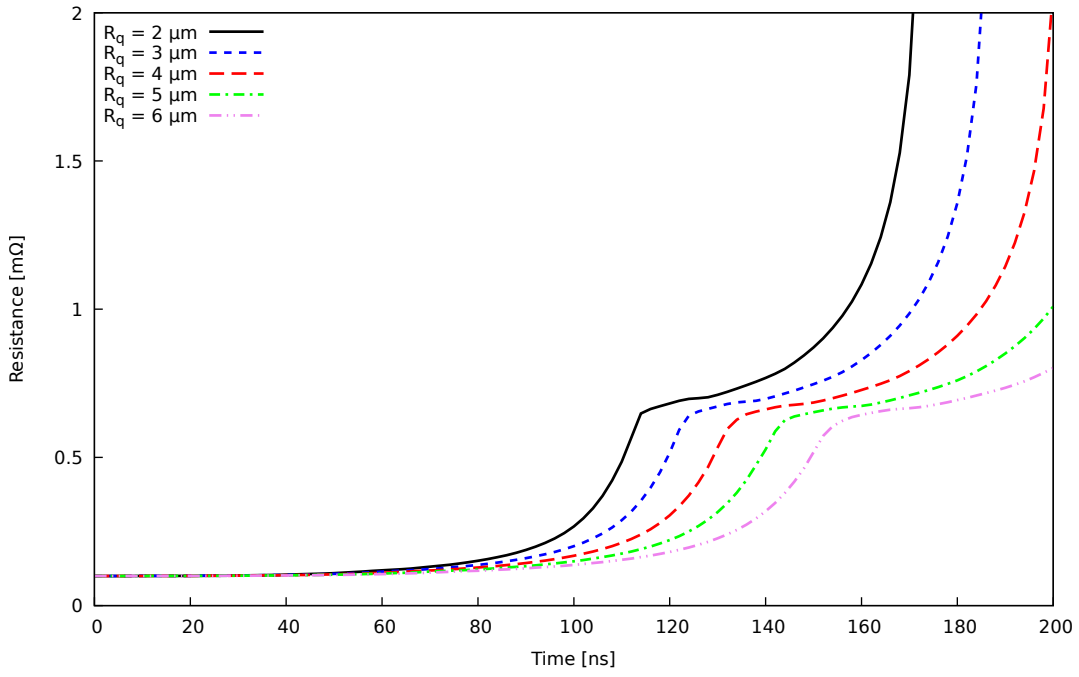


Figure 4.5: Evolution of the resistance of a Gaussian surface at constant separation distance between the surfaces, with time under D-wave, for $R_a = 12\,\mu m$ and for different values of $R_q$. Averaged over 100 different seeds.

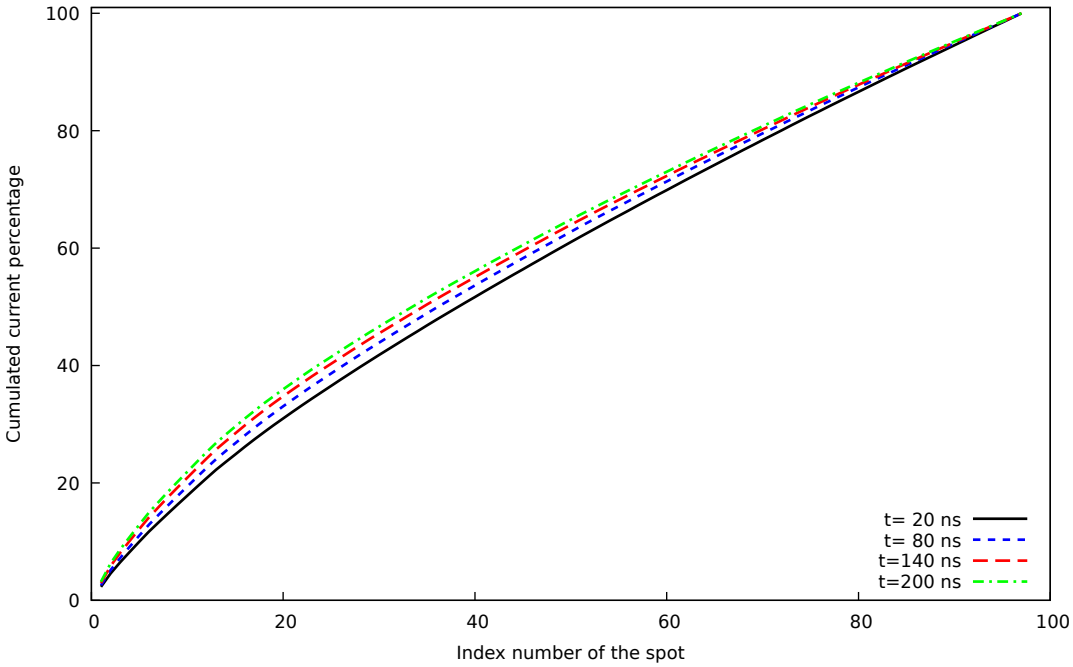


Figure 4.6: Cumulated current percentage in the a-pots sorted by decreasing size in a 0.1 mΩ contact with constant tightening distance ($R_a = 12\,\mu m$, $R_q = 4\,\mu m$).

### 4.3.2 Multi-spot contact under constant load

The same approach is conducted, but this time the mechanical loads of Table 4.1 that correspond to an initial resistance of 0.1 mΩ are kept constant. Figure 4.7 shows the evolution of the cumulated percentage of the total current in the a-spots sorted by decreasing size for $R_a = 12\,\mu m$ and $R_q = 4\,\mu m$.

The initial current distribution between the a-spots is naturally the same as the one obtained with a constant separating distance on Figure 4.6. However, in this case the redistribution of the current between the a-spots is much more pronounced: between $t = 0\,ns$ and $t = 50\,ns$, only the 100 biggest a-spots contribute to the conduction of the lightning current. With time, some of them experience the decrease of their mechanical properties and the tightening distance has to decrease to ensure the mechanical equilibrium. As a consequence more micro-peaks can interfere with the mating surface and new a-spots are created. At $t = 200\,ns$, it can be seen on Figure 4.7 that the number of a-spots has been increased by a factor of four. At $t = 1\,\mu s$, all the micro-peaks in the contact form a-spots, the total number of a-spots has reached its maximum, and the current distribution has evolved to a quasi-parabolic distribution.

The influence of the surface parameter $R_q$ on the micro-geometry is depicted on Figure 4.8, showing the evolution of the number of a-spots, and Figure 4.9, showing the evolution of the average a-spot radius. It can be observed that initially a larger value of $R_q$ means fewer but larger a-spots in the contact. The initial number of a-spots remains

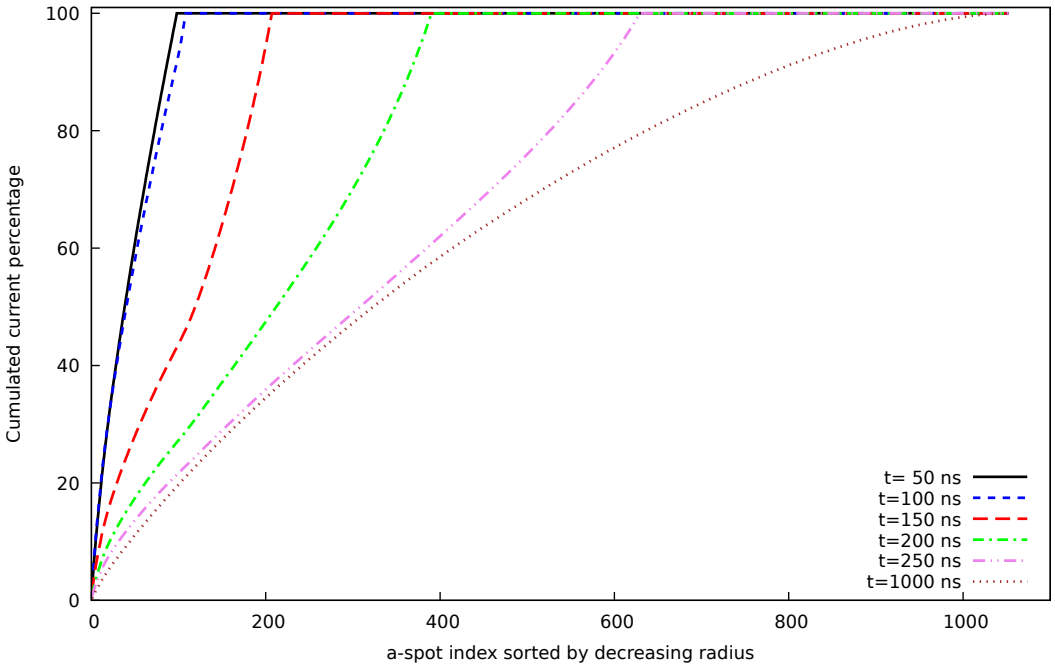


Figure 4.7: Cumulated current percentage in the a-pots sorted by decreasing size in a 0.1 mΩ contact with constant tightening force ($R_a = 12\,\mu m$, $R_q = 4\,\mu m$).

almost unchanged during the first 100 ns. Then, a fast increase associated with the collapse of the mechanical properties is observed that occurs sooner for smaller values of $R_q$.

Interesting is to notice that this fast increase of the number of a-spots first leads to a decreasing a-spot radius, although the radii of the first a-spots increases. This is similar to the electrostatic case of Figure 4.4 under increasing load, and is due to the fact that smaller and smaller a-spots are created. For the case $R_q = 2\,\mu m$, this process stops when all the micro-peaks in the contact interfere and form a-spots.

Then, the mean a-spot radius increases due to mechanical flattening, which is observed when or before all of the micro-peaks are reached. For the case $R_q = 6\,\mu m$, the mean radius even starts to increase before all the micro-peaks have formed a-spots, meaning that the mechanical flattening of the largest a-spots dominates the increasing number of smaller a-spots.

Surprisingly, the mean a-spot radius for the different surface roughness seems to converge to very similar values during this mechanical flattening phase. This behaviour is not intuitive, since initially the a-spot distributions are quite different and because the tightening forces differ by more than 40 %. Simultaneously to the increasing mean a-spot radius, mechanical flattening also induces a decreasing a-spot length. According to equations 2.3, 2.4 and 2.5, for small lengths and large radii the Holm's term dominates the cylindrical term in the expression of the resistance of the a-spots. The convergence

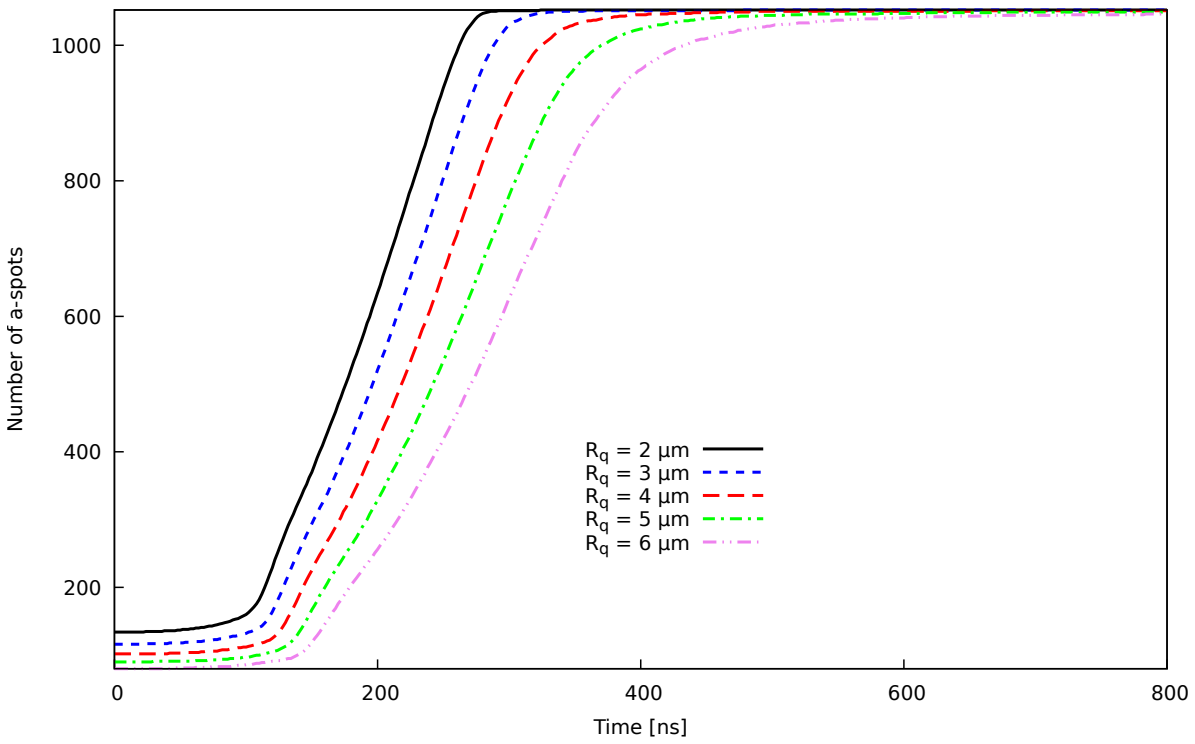


Figure 4.8: Evolution of the number of a-spots in a 0.1 mΩ contact subject to a D-wave under constant tightening force for $R_a = 12\,\mu m$ and different values of $R_q$. Averaged over 100 different seeds.

of the mean a-spot radius for the different surface parameters during flattening is then associated with the convergence of the contact resistance, as can be seen on Figure 4.10.

Notably, the evolution of the contact resistance is weakly influenced by the surface parameter $R_q$, with a first increasing resistance up to a maximum of 0.18 mΩ at $t = 100\,ns$ for $R_q = 2\,\mu m$ and $t = 150\,ns$ for $R_q = 6\,\mu m$, followed by a decreasing phase at almost the same rate for all the cases. A minimum resistance value two orders of magnitude smaller than the initial a-spot resistance is reached a $t = 1\,\mu s$, with 12 µΩ and 13 µΩ for $R_q = 2\,\mu m$ and $R_q = 6\,\mu m$ respectively.

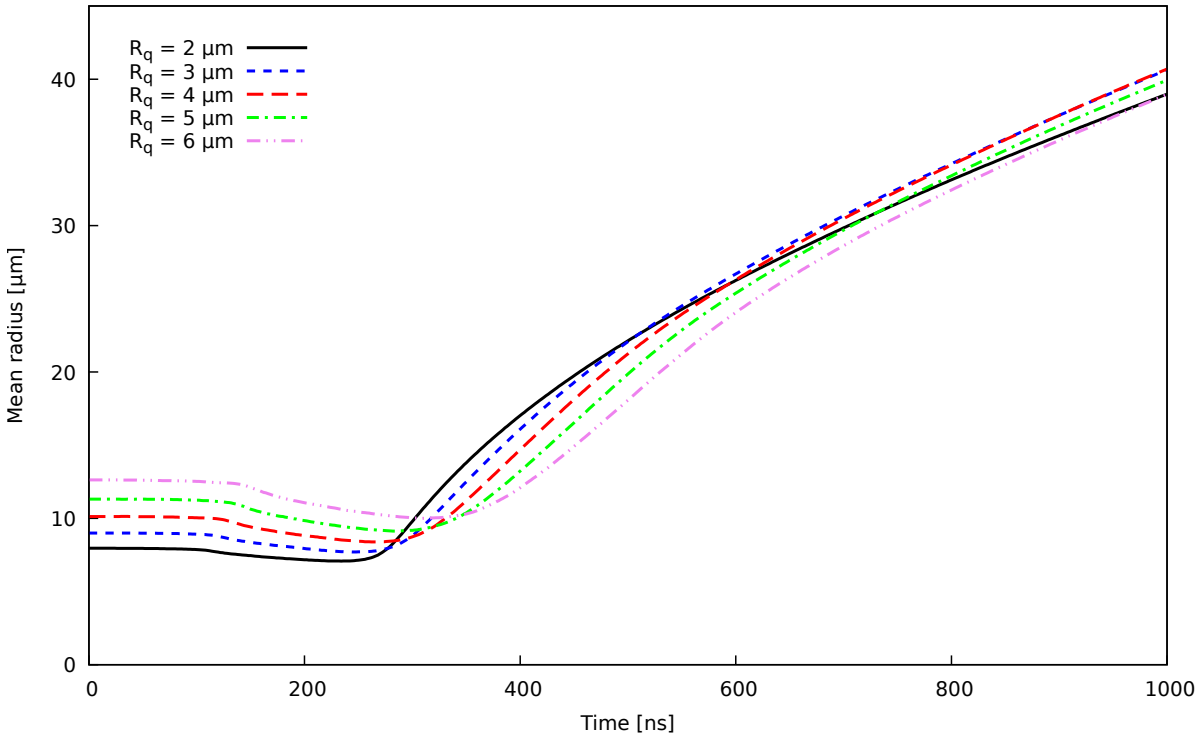


Figure 4.9: Evolution of the mean radius in a 0.1 mΩ contact subject to a D-wave under constant tightening force for $R_a = 12\,\mu m$ and different values of $R_q$. Averaged over 100 different seeds.

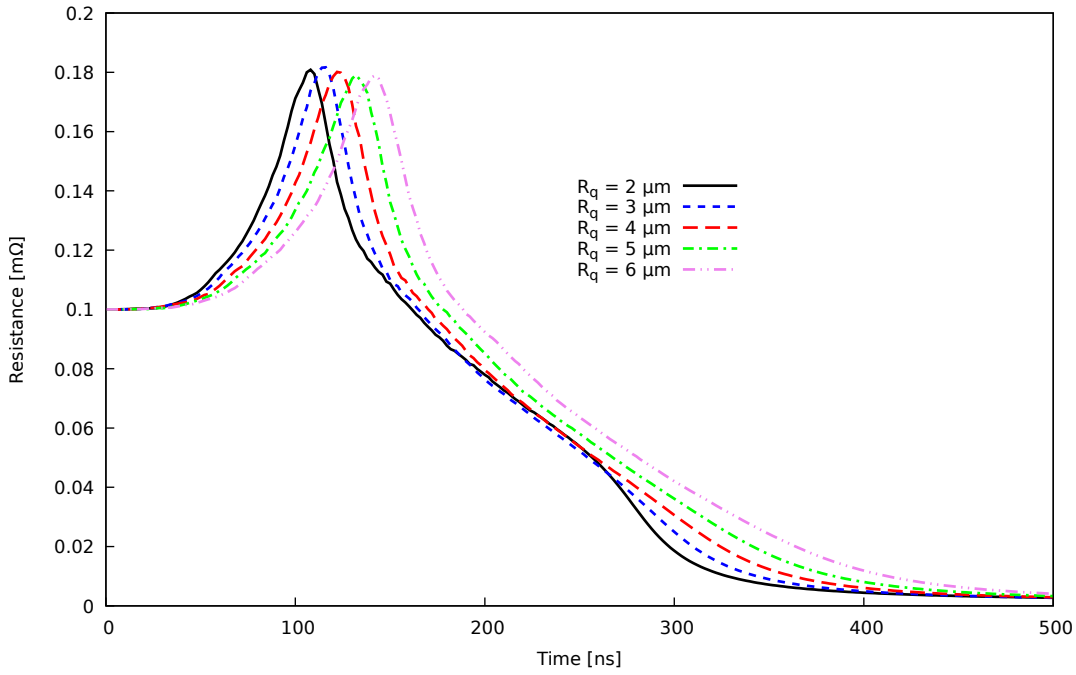


Figure 4.10: Evolution of the resistance of a 0.1 mΩ contact subject to a D-wave under constant tightening force for $R_a = 12\,\mu m$ and different values of $R_q$. Averaged over 100 different seeds.

The influence of $R_q$ appears to be limited in the range of interest. However, all the micro-peak distributions considered are characterized by the same mean a-spot radius $R_a = 12\,\mu m$. To check the influence of this parameter, the same method has been applied keeping same the value of $R_q$ to $4\,\mu m$ and varying $R_a$ in the range $4\,\mu m$ to $20\,\mu m$ with an initial contact resistance of $0.1\,m\Omega$. The tightening forces necessary to impose the initial resistance differ by more than 50 % between $R_a = 4\,\mu m$ and $R_a = 20\,\mu m$ and are given in Table 4.2. The evolution of the contact resistance is presented on Figure 4.11.

Quantitatively, the influence of a larger mean a-spot radius is similar to a larger $R_q$. However, even if the maximum value of the contact resistance remains close to $0.18\,m\Omega$ between 100 ns and 200 ns, the decrease due to mechanical flattening varies strongly with $R_a$. A larger $R_a$ means a later maximum resistance but also a slower decrease of the resistance during flattening. This is due to the larger thermal inertia of the a-spots for large values of $R_a$ that makes the temperature and the mechanical properties evolve slowly compared to a distribution with a smaller mean a-spot radius. At $t = 1\,\mu s$, the resistance is lowered by approximatively two orders of magnitude compared to the initial resistance, but significant differences remain between the different distributions within a factor of two. Moreover, the resistance values at $t = 1\,\mu s$ does not seem to be simply related to the value of $R_a$ and they keep on decreasing at a slower and slower rate.

| $R_a$ (µm) | 4 | 8 | 12 | 16 | 20 |
|---|---|---|---|---|---|
| Tightening Force (N) | 14.34 | 18.04 | 21.87 | 25.92 | 29.34 |

Table 4.2: Tightening forces needed to reach $0.1\,m\Omega$ in a $40\,mm^2$ contact with roughness parameters $N_s = 26.3\,mm^{-2}$, $R_q = 4\,\mu m$ and different values of $R_a$.

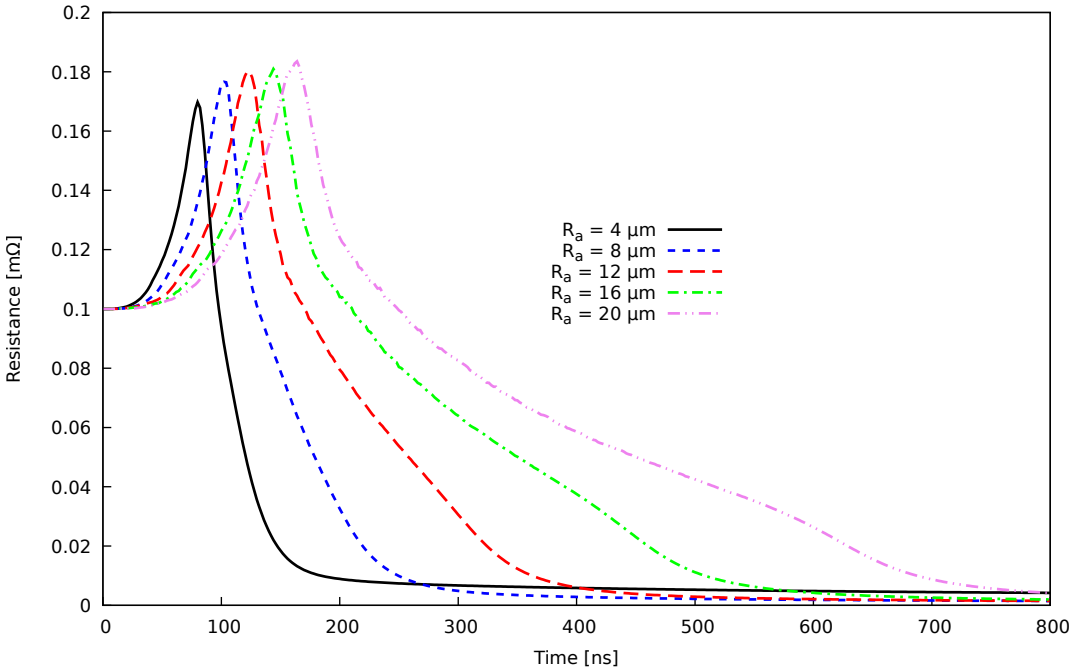


Figure 4.11: Evolution of the resistance of a 0.1 mΩ contact subject to a D-wave lightning current. A constant load is considered, with $R_q = 4\,\mu m$ and different mean a-spot radii. Averaged over 100 different seeds.

## 4.4 Conclusion

A multi-spot contact with a realistic surface micro-geometry has been successfully simulated with the 0D model. The surface is described with a Gaussian distribution for the heights of cylindrical micro-peaks, assuming that each micro-peak's height equals its diameter. The parameters of such distribution are its number of peak by unit of surface, the mean height value and the standard deviation. Taking the values measured by profilometry and used by Schoft [40] allows to recover the decreasing low-level current contact resistance with the tightening force, and gives very similar results to Schofts' spherical micro-peak models for high tightening forces.

A parametric study on the influence of the surface roughness parameters on the behaviour of a contact subject to a D-wave has been conducted, and important regularities, that barely depend on the details of the micro-geometry have been identified:

- When a D-wave current is applied on a metallic contact representative of an aeronautic assembly, current redistributions and important resistance evolutions can be obtained on time-scales lower than 1 µs.

- For contacts with a constant tightening distance, the resistance can only increase, leading to the full vaporization of the a-spots. In this case, the vaporization dynamics is very similar to the one observed with single a-spot contacts: The resistance

of the contact increases monotonously due to the decreasing conductivity with temperature in the first hundreds of nanoseconds, and then increases exponentially due to the vaporisation of the metal as soon as a boiling front appears. Current redistributions between the a-spots are moderate in this case.

- For contacts with a constant tightening force, the resistance first increases due to the decreasing conductivity of the metal with the temperature. When the temperature reaches a critical value close to the melting point, the collapse of the mechanical properties leads to the mechanical flattening of the a-spots and the fast decrease of the contact resistance. No vaporization is therefore observed in this case.

- For contacts with constant tightening force, the final resistance value may be two orders of magnitude lower than the initial contact resistance due the welding of the two parts.

- The root mean square $R_{\mathrm{q}}$ of the height distribution of the micro-peaks has a limited influence on the contact evolution. Increasing $R_{\mathrm{q}}$ increases the average size of the a-spots, and the contact dynamics is in this case a little slower due to thermal inertia.

- Increasing the mean micro-peak height $R_{\mathrm{a}}$ has an influence similar to increasing $R_{\mathrm{q}}$, except that the thermal inertia effect due to larger a-spots is more pronounced during the decreasing resistance phase in contacts subject to a tightening force.

The cases with constant tightening distance or constant mechanical load are limit cases for a wide range of complex mechanical configurations that can be observed in actual assemblies. The developed model does not allow at this stage of the work to directly perform comparisons with current experimental studies conducted for example on GRIFON, the lightning generator of ONERA. However, it can bring useful interpretations of the puzzling measurements that can be performed on the contact resistances in assemblies.

For example, Table 4.3 shows some typical evolution of the measured resistance of a metal-metal contact between a bolt and a locking-cage (see Figure 4.12).

| Shot N° | $I$ (A) | $R_0$ (mΩ) | sparking | $R_f$ (mΩ) |
|---|---|---|---|---|
| 1 | 650 | 8 | + | 450 |
| 2 | 100 | 8 | + | 920 |
| 3 → 11 | 100 → 900 | 920 | - | 48.2 |
| 12 | 1400 | 48.2 | - | 22 |
| 13 | 1800 | 22 | + | 4500 |
| 14 | 1800 | 4500 | ++ | $10^8$ |
| disassembly - assembly: $R_0$=7 mΩ | | | | |
| 15 → 23 | 100 → 900 | 7 | - | x |
| 24 | 1100 | x | + | 290 |
| 25 | 100 | 290 | + | 400 $10^3$ |
| 26 | 100 | 400 $10^3$ | + | 2 $10^3$ |
| 27 | 100 | 2 $10^3$ | + | 260 $10^3$ |
| 28 | 100 | 260 $10^3$ | + | 4.3 $10^3$ |
| 29 | 100 | 4.3 $10^3$ | + | 450 |
| 30 | 100 | 450 | + | 4.4 $10^3$ |

Table 4.3: Experimental measurements of the evolution of the contact resistance between a bolt and a locking cage. Successive shots have been performed on the GRIFON lightning generator with “D-wave-like" current forms of amplitude $I$. $R_0$ and $R_f$ are the contact resistance before and after each shot respectively. “x" means that the measured values are unavailable ; “-" means that no discharge is observed ; “+" means that a discharge is observed ; “++" means that the observed discharge seems particularly energetic from light emission.

30 shots have been performed with the GRIFON generator, with D-wave current waveforms scaled to different current levels, from 100 A to 1.8 kA. After 14 shots, then bolt was disassembled and reassembled. It can be seen from the contact resistances before shot ($R_0$) and after shot $R_f$, that large variations on several orders of magnitude can be obtained. Interesting is to note that in some cases (shots 3 to 11), the contact resistance may decreases by more than one order of magnitude without any observed discharge phenomena. On the other hand, during some series of shots (12 to 14), the resistance increases exponentially and a discharge is ignited systematically. These results can be qualitatively interpreted thanks to the 0D model in the following way: The decreasing resistance phases, not associated with any discharge or vaporization phenomena correspond to a mechanical situation where the a-spots in the contact are crushed due to the tightening force. In return, the increasing resistance phases are associated with a mechanical situation where the contact has a constant tightening distance. In this case the resistance increases due to the vaporization of the totality or part of the a-spots, and discharges are observed.

However, the shots 25 to 30 remain disturbing with this simple interpretation, since there seems to be an alternation between increasing and decreasing resistances, that are always associated with discharge phenomena. One of the possible explanations relies

on a fixed tightening distance, leading to discharge ignitions at each shot. Then it is expected that in some cases, the resistance may decrease thanks to the metallic vapour emitted by the discharge that may be confined inside the contact and may create new a-spots during cooling and condensation. This condensation scenario is given credibility by the observation, during the discharges, of many small, incandescent metallic droplets or particles escaping from the contact (see 4.12).

Considering our lack of understanding on discharges and their possible importance, it seemed necessary to further increase our present understanding of the contact dynamics in order to focus into more details into the metallic vapour generated in a contact and related discharge phenomena. This is the purpose of Chapter 5.

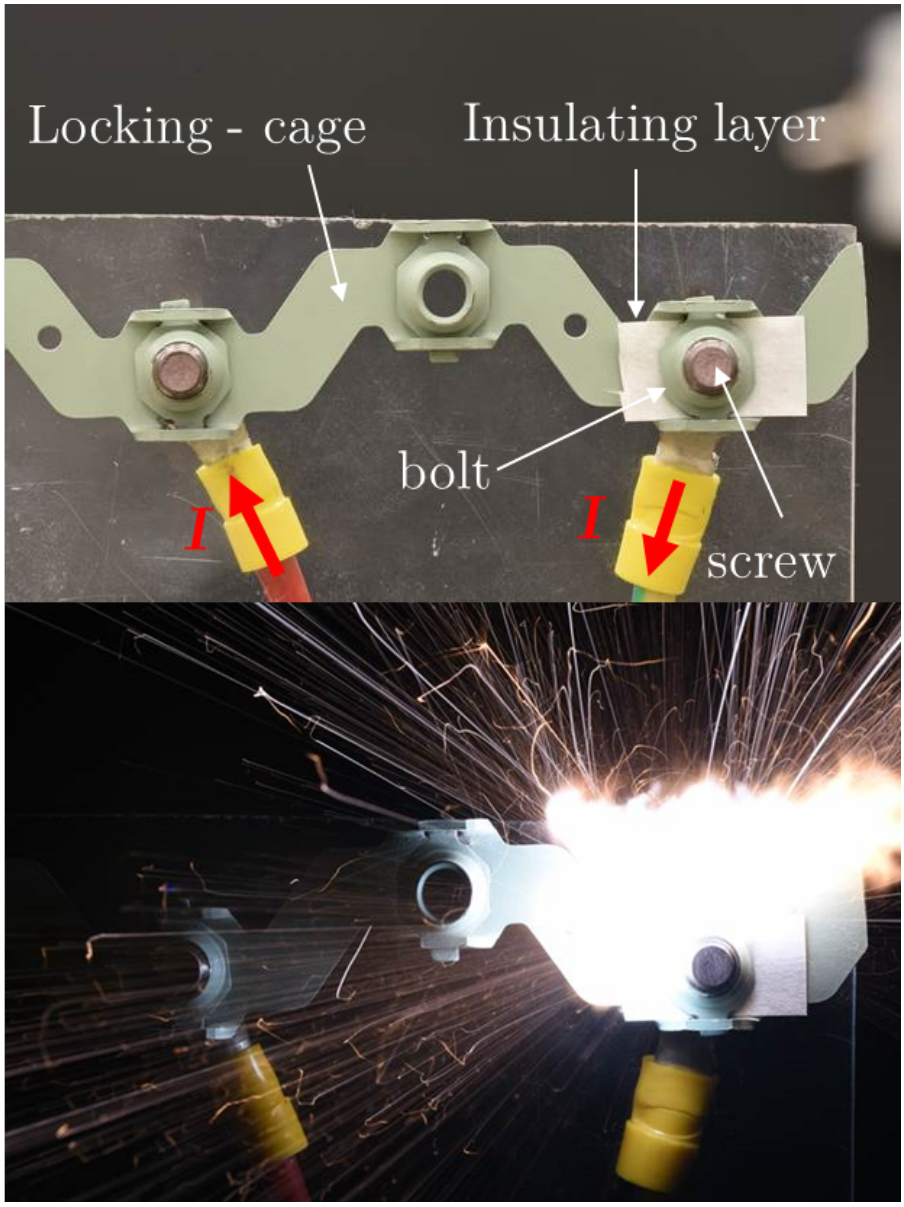


Figure 4.12: Sparking of a metal-metal contact between a locking cage and a bolt for D-wave current of 1800 A.

# Chapter 5

# Sparking model around contacts

The complex multi-physics in metal-metal contacts subject to high current levels is of primary importance regarding the discharge ignition risk in aeronautic assembly during lightning strikes on aircraft.

The model developed in the previous chapters and the parametric studies performed have revealed an important fact: Due to mechanical effects, a contact subject to a constant load, that can freely be crushed when the temperature approaches the melting point, should never give birth to metallic vapour. Because in this case the contact resistance is decreasing, the electric-field never reaches values comparable to the breakdown threshold and field ignited discharges in those conditions are very unlikely. On the other hand, the situation is opposite when considering a contact with a constant separating distance.

In this case the metal of the a-spot may be fully vaporized, leading to a diverging contact resistance and electric-field. This diverging scenario could be attenuated by current redistributions in the assembly: for example current paths in the structure that were initially too resistive to carry a significant current may start to be the preferable path as the contact resistance increases. However, such redistribution phenomena may take time to establish due to inductive effects at the scale of the assembly. Moreover, for some particular geometries the other possible paths are so resistive that an electrical breakdown seems unavoidable.

Then, contacts with constant separating distance seem to be good candidates for discharge ignition and important vapour and energy releases. In this chapter, an attempt is made to go beyond one of the most questionable hypothesis of the 0D model: the zero conductivity of the metallic vapour when a-spots reach the boiling point. Taking into account the vapour's conductivity may lead to three major improvements. First, to avoid the non-physical divergence of the resistance and electric-field in the contacts with constant separating distance. Then, to compute the redistribution of the current between the a-spot and the plasma. Finally, to evaluate the three most important physical parameters for discharge ignition and out-gasing risk in assemblies: the volume of vaporized metal,

the energy dissipated by Joule heating in the discharge, and the over-pressure that can be obtained with such a discharge in a confined media.

Modelling the metallic plasma discharge that may ignite around an a-spot is a challenging issue. Indeed, the plasma is initially very dense and quite cold as it is formed by the vaporization of the solid metal under isochoric heating. On the other hand, the high pressure makes it expand and a fast density decrease is expected. Depending on the confinement of the plasma, the final density can be as low as the order of magnitude of air density. Moreover, the plasma temperature may possibly reach a few tens of thousands of Kelvin, due to the lightning current circulation. The very large range of densities and temperatures that have to be managed by the model, as well as the fast plasma expansion in the confining medium have required a lot of effort during this thesis. There are therefore three main difficulties for the plasma model:

- To be simple to couple with the 0D a-spot model previously derived.
- To describe the expansion dynamics of the high pressure plasma in a confined media.
- To compute the thermodynamic and transport properties of the plasma in a wide range of densities and temperatures.

In order to focus on the effect of the expansion of the metallic vapour, a single a-spot contact have been considered in this chapter, with a radius $a$ and a constant thickness $l$. The obtained conclusions are not restrictive according to the similarities previously observed between several a-spots and a single a-spot contacts for a constant tightening distance. Then, no significant differences between the presented results on a single a-spot contact and a multi-spot contact of equivalent resistance are expected.

## 5.1 Gas expansion model

Following on from the cylindrical a-spot hypothesis, the axial symmetry is preserved in the plasma model with the assumption that the vaporized metal expands radially, as illustrated on Figure 5.1. The expansion front could be affected by the presence of obstacles, such as other a-spots or micro-peaks, or subject to Rayleigh-Taylor instabilities. However, addressing these complex 3D effects is beyond the scope of this model, that have to be simple enough to be fast and easy to use while providing good physical estimates.

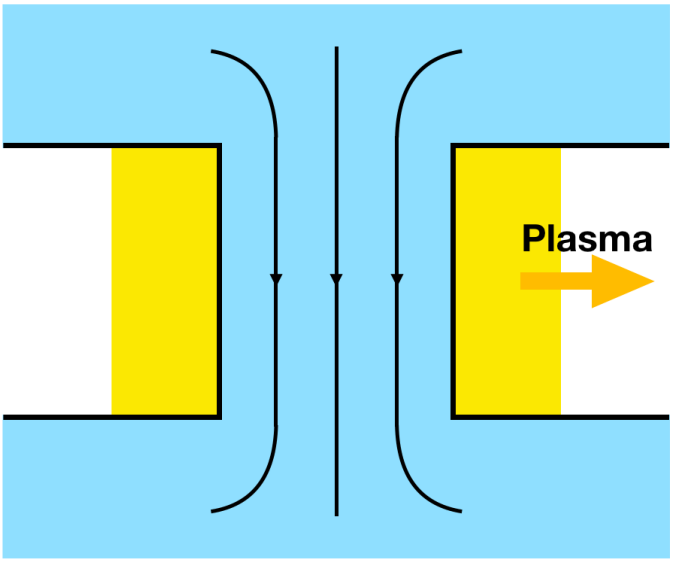


Figure 5.1: Schematics of the vaporized metal expansion.

Keeping unchanged the assumptions made for the physics governing the internal evolution of the a-spot in Chapter 2, the computed vaporized volume of metal is taken as a source term for the plasma expansion model. The output of the expansion model is the evolution of the plasma radius $r_\mathrm{p}$ (m) and its intensive properties, its density $\rho_\mathrm{p}$ ($\mathrm{kg\,m^{-3}}$), its pressure $P_\mathrm{p}$ (Pa) and its specific internal energy $e_\mathrm{p}$ ($\mathrm{J\,kg^{-1}}$), assumed homogeneous.

### 5.1.1 Modelling of the confining media

To model the confining media around the plasma, two situations have been considered: A constant confinement pressure $P_\mathrm{conf}$ (Pa), and a constant confinement volume $V_\mathrm{conf}$ ($\mathrm{m^3}$). The pressure $P_\mathrm{conf}$ is mechanically opposed to the expansion of the gas.

$P_\mathrm{conf}$ can be assumed constant, for example at the atmospheric pressure if the contact is supposed in open air, but it can be much larger, considering for example a contact filled with sealant. $P_\mathrm{conf}$ can also be used as a free parameter to represent the complex confinement by the micro-geometry, since the many a-spots or micro-peaks may be seen as a porous media confining the discharge. In the following, the influence of this parameter is discussed.

Imposing instead a confinement volume $V_\mathrm{conf}$ simply means that the plasma discharge has to expand in a closed volume, whose pressure therefore increases by compression. This volume is representative of the micro gaps that can be found in aeronautic assemblies. For example in fasteners, small volumes of air of a few $\mathrm{mm^3}$ may be present between different parts, such as a screw and a bolt, or a screw and the skin of the aircraft, as represented on Figure 5.2. One of the most important question aircraft manufacturers may have to face is whether or not a given fastener design may mechanically confine an

energetic discharge occurring in those micro-gaps. Some lightning protections consist in a nut-cap (see Figure 5.2), filled with air or sealant, that can be also seen as a fixed expansion volume for a plasma discharge that has to be confined in the vicinity of fuel tanks. The over-pressure generated by a plasma in such small volumes is then of primary importance regarding the discharge risk in aeronautic assemblies and fastener design.

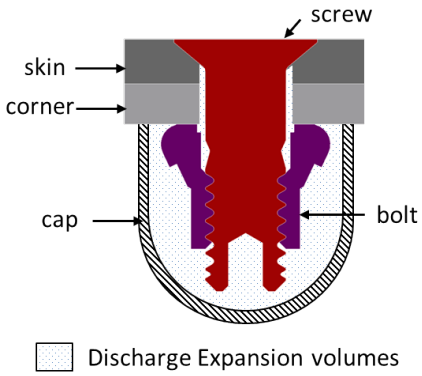


Figure 5.2: Schematics of an aeronautic fastener with internal gaps.

Theoretically, the expansion of a high pressure plasma in a confining medium should follow the compressible Euler equations for a multiphase flow. However, solving Euler equations would require a refined 1D mesh and a computationally limiting CFL condition. The time needed by a finite volume scheme with a Riemann solver would be too large for the 0D model considered in this study.

### 5.1.2 Pressure equilibrium or plasma expansion speed limit

The 0D expansion model presented is an approximate time-explicit solver for the evolution of $r_\mathrm{p}$. If the plasma radius at time $t$, $r_\mathrm{p}^t$, is known, along with the pressure, the energy, and the density, the new radius at time $t + dt$, $r_\mathrm{p}^{t+dt}$ can be computed. The assumption made is that the plasma reaches equilibrium with the confinement media unless its front speed needs to be higher than the speed of sound in the current conditions. Indeed, the plasma at $t + dt$ has more energy and mass than at $t$ because of vaporization and Joule effect, and needs to expand in order to maintain pressure equilibrium.

The confining pressure is either constant, if chosen as a free parameter, or a function of the plasma expansion, if it is the total volume that is chosen constant. In that last case, $P_\mathrm{conf}$ is time-dependent and is given by Equation 5.1

$$P_\mathrm{conf}^t = P_0 \left( \frac{V_\mathrm{conf}}{V_\mathrm{p}^t} \right)^\gamma \tag{5.1}$$

where $P_0$ is the initial pressure inside the confinement volume, $\gamma$ the isentropic coeffi-

cient of the confining medium, and $V_\mathrm{p}$ the plasma volume, given by Equation (5.2)

$$V_\mathrm{p} = l\,\pi(r_\mathrm{p}^2 - a^2) \tag{5.2}$$

With this formulation, the confining medium is supposed to be a perfect gas, subject to an isentropic compression by the plasma.

Given this value of $P_\mathrm{conf}^t$, the plasma radius $r_\mathrm{p}^{t+dt}$ is computed to ensure the mechanical equilibrium following Equation (5.3)

$$P_\mathrm{p} = P_\mathrm{conf} \tag{5.3}$$

This condition is assumed always true unless the expansion is limited by the speed of sound, in which case it remains over-pressurized. Indeed, the plasma expansion velocity is bounded by the speed of sound inside the plasma $c_\mathrm{p}$ ($\mathrm{m\,s^{-1}}$), leading to Equation 5.4. In this case, $c_\mathrm{p}$ controls the plasma expansion, and $P_\mathrm{p}$ remains higher than $P_\mathrm{conf}$.

$$r_\mathrm{p}^{t+dt} = r_\mathrm{p}^t + c_\mathrm{p}\,dt \tag{5.4}$$

The fact that plasma density $\rho_\mathrm{p}$ ($\mathrm{kg\,m^{-3}}$), pressure $P_\mathrm{p}$ (Pa) and temperature $T_\mathrm{p}$ (K) are supposed uniform inside the plasma volume, is actually equivalent to assuming that the speed of sound inside the plasma is high enough compared to the expansion velocity. This hypothesis is quite reasonable when $P_\mathrm{conf}$ dominates the radial expansion, but could be discussed when the expansion speed is bounded by $c_p$.

For this model, it is needed to compute the plasma properties (speed of sound, conductivity and pressure), as well as the Joule effect due to current distribution inside the plasma. The model used to handle the metallic plasma properties will be the purpose of Section 5.2. Assuming these properties are known, the current distribution model is first presented.

### 5.1.3 Current distribution in the plasma

If metallic vapour is generated from an a-spot, the current may be redistributed between the a-spot and the metallic plasma, and generate Joule effect in that plasma. We assume here that the a-spot vaporization started, and that we know the plasma expansion radius $r_\mathrm{p}$, the solid a-spot radius $a$, as well as $\sigma_\mathrm{p}$ and $\sigma_\mathrm{a}$, the conductivity values of the plasma and the a-spot respectively ($\mathrm{S\,m^{-1}}$).

To take into account this current redistribution, the resistance of the a-spot $R_\mathrm{a}$ ($\Omega$) and the resistance of the plasma $R_\mathrm{p}$ ($\Omega$) are assumed to be in parallel. $R_\mathrm{p}$ ($\Omega$) is simply

calculated with the analytical formula for a straight hollow cylindrical conductor (5.6).

$$R_{\mathrm{a}} = \frac{l}{\sigma_{\mathrm{a}} \pi a^2} \tag{5.5}$$

$$R_{\mathrm{p}} = \frac{l}{\sigma_{\mathrm{p}} \pi \left(r_{\mathrm{p}}^2 - a^2\right)} \tag{5.6}$$

A constriction resistance $R_{\mathrm{c}}$ has to be added in the model, placed in series with $R_{\mathrm{p}}$ and $R_{\mathrm{a}}$, in order to compute the total resistance $R$. Holm's formula is used to provide an estimate of this constriction resistance, even though the applicability of this formula could be discussed: As shown in Chapter 1, Holm's analytical model relies on the hypothesis of a uniform conductivity in the constriction region. It is clearly not the case in the presence of the plasma, and a choice has to be maid if the radius taken into account in Holm's formula should rather be $a$, the radius of the a-spot, or $r_{\mathrm{p}}$, the expansion radius of the plasma. In this study, the choice has been maid to consider $r_{\mathrm{p}}$ as the constriction radius, since in the situation of the complete vaporization of the a-spot $a$ tends to zero and the corresponding constriction resistance would diverge. Therefore we have:

$$R_{\mathrm{c}} = \frac{1}{2\sigma_{\mathrm{b}} r_{\mathrm{p}}} \tag{5.7}$$

$$R = R_{\mathrm{c}} + \frac{R_{\mathrm{a}} R_{\mathrm{p}}}{R_{\mathrm{a}} + R_{\mathrm{p}}} \tag{5.8}$$

where $\sigma_{\mathrm{b}}$ ($\mathrm{S\,m^{-1}}$) is the electric conductivity of the bulk material, and $R$ ($\Omega$) the total resistance of the contact with the plasma discharge.

Imposing a current $I$ (A) through this contact, the currents going through the solid metal $I_{\mathrm{a}}$ and through the plasma $I_{\mathrm{p}}$ are given by Equation 5.9, and is assumed homogeneous inside the solid a-spot and inside the plasma.

$$I_a = \frac{R_{\mathrm{p}}}{R_{\mathrm{a}} + R_{\mathrm{p}}} \cdot I \quad \text{and} \quad I_p = \frac{R_{\mathrm{a}}}{R_{\mathrm{a}} + R_{\mathrm{p}}} \cdot I \tag{5.9}$$

### 5.1.4 Dichotomy method to solve the plasma expansion

Assuming again that plasma properties can be computed with the knowledge of its composition, density and internal energy (basing on the model presented in Section 5.2), the current distribution model allows to simulate a complex coupling of a-spot vaporization and plasma expansion. Assuming $r_{\mathrm{p}}^t$ is known, a dichotomy method is used in order to compute $r_{\mathrm{p}}^{t+dt}$. Its boundaries are limited by the speed of sound as given by Equation 5.4. Within these boundaries, guessing $r_{\mathrm{p}}^{t+dt}$ leads to guessing the new plasma volume $V_{\mathrm{p}}^{t+dt}$ and all other properties.

- During expansion, the total plasma energy $E_\mathrm{p}$ (J) evolves due to the Joule heating, the work of the confining pressure forces, and the production of plasma from the vaporization of the a-spot. The time discretization of this equation solved by the model is given by Equation 5.10, where $R_\mathrm{p}$ ($\Omega$) and $I_\mathrm{p}$ (A) are the plasma resistance and the current flowing in the plasma respectively, and $e_\mathrm{vap}$ ($\mathrm{J\,m^{-3}}$) is the volumic vaporization energy of the metal.

$$E_\mathrm{p}^{t+dt} = E_\mathrm{p}^{t} + R_\mathrm{p}^{t}\left(I_\mathrm{p}^{t}\right)^2 dt - P_\mathrm{conf}\left(V_\mathrm{p}^{t+dt} - V_\mathrm{p}^{t}\right) + e_{vap}\pi\, l((a^{t+dt})^2 - (a^{t})^2) \quad (5.10)$$

- The internal energy of the plasma $U_\mathrm{p}$ (J) is given by Equation 5.11, where $E_\mathrm{c}$ (J) is the kinetic energy of the plasma.

$$U_\mathrm{p} = E_\mathrm{p} - E_\mathrm{c} \quad (5.11)$$

$E_\mathrm{c}$ (J) is obtained by the spatial integration of the specific kinetic energy following Equation 5.12.

$$E_\mathrm{c} = \frac{1}{2}\int_a^{r_\mathrm{g}} \rho_\mathrm{g}\cdot 2\pi\cdot r\cdot l\cdot v^2\left(r\right)\cdot \mathrm{d}r = \pi\rho_\mathrm{g}{v_\mathrm{g}}^2 l\left[\frac{\left(r_\mathrm{g}-a\right)^2}{4} + \frac{a\left(r_\mathrm{g}-a\right)}{3}\right] \quad (5.12)$$

For this integration, the plasma velocity $u_\mathrm{p}$ is asuumed to be null close to the a-spot, and to evolve linearly in the radial direction until $r = r_\mathrm{p}$ and $u_\mathrm{p} = u_\mathrm{exp}$ (Equation 5.13). This hypothesis have been made based on 1D simulation results for the velocity profile in free burning arc columns subject to a pulsed arc phase [77].

$$u_\mathrm{p}(r) = \frac{r-a}{r_\mathrm{p}-a}\,u_\mathrm{exp} \quad \text{for } a \le r \le r_\mathrm{p} \quad (5.13)$$

Finally, the new properties induced by the guess $r_\mathrm{p}^{t+dt}$ either lead to a plasma pressure lower (resp. higher) than $P_\mathrm{conf}$, in which case the real expansion must be lower (resp. higher). The dichotomy ends as soon as the pressure equilibrium, Equation 5.3, is ensured within the desired precision, or that $r_\mathrm{p}^{t+dt}$ is sufficiently close to the boundaries given by the speed of sound.

The presented expansion model relies on the knowledge of the pressure, the temperature, the speed of sound, and the electric conductivity in the plasma as a function of the specific internal energy and density. An equation of state (EOS) and a plasma conductiv-

ity model for metallic plasmas are then needed that should be able to deal with a large range of densities and temperatures.

## 5.2 Quotidian equation of state for metals

To compute the plasma properties from the solid density to the density of a kinetic plasma at atmosphereic pressure, a Quotidian Equation of State, mainly taken from [78] and [79] has been used. It was developed at Onera to model the explosion under high, transient current levels, of thin conductors such as thin wires or lightning protections.

This method relies on the description of the plasma thermodynamic properties as the sum of three components: the contribution of the electrons, the contribution of the ions, and a bounding term related to quantum effects at high density and bounding interactions. A Thomas-Fermi ionization model is added to provide the ionisation degree of the plasma as a function of density and temperature. For example, the internal energy and the pressure are given by Equations 5.14 and 5.15, where subscripts “e", “i" and “b" stand for “electrons", “ions", and “bounding".

$$E_{\mathrm{p}} = E_{\mathrm{e}} + E_{\mathrm{i}} + E_{\mathrm{b}} \tag{5.14}$$

$$P_{\mathrm{p}} = P_{\mathrm{e}} + P_{\mathrm{i}} + P_{\mathrm{b}} \tag{5.15}$$

The contributions of the electrons and the ions follow equations of state representative of dense plasmas, that may depend on the temperature and the density. Most of the time, ions and electrons EOS are similar to a perfect gas law with additional terms to take into account the non-ideality of the plasma at high density, and Coulomb interactions when the average distance between the charged particles is lower than the Debye length, such as the Debye-Hükel model [80]. In this work, the ion EOS is based on a modification of the widely known Cowan model [78], while the electron EOS is given by the semi-empirical model of McClosekey [81]. The bounding terms are modelled with a Lennard-Jones potential, with parameters taken from [79].

While relying on important simplifications and semi-empirical formulas, the QEOS is able to give good qualitative estimates for the properties of a metal in a very wide range of temperatures and densities. Recently, more precise descriptions have proven successful by the use of Quantum Molecuar Dynamic simulations (QMD), as in [82] and [83], and Density Functional Theory (DFT) [84]. However, such ab-initio calculations are very complex and time consuming, and the QEOS model offers a good fisrt order approximate EOS [85] and seems adequate for the simple plasma model derived in this study.

As an example, Figure 5.3 shows the phase diagram for iron that has been computed

thanks to the QEOS model, along with a Maxwell algorithm to remove the so-called Van-der-Waals loops and compute the bi-phasic regions. This plot shows the isotherms of iron between 300 K and $10^4$ K in the $P$-$\rho_s/\rho$ plan, where $\rho_s$ is the solid density in standard conditions. It can be clearly seen that the density range goes from solid to a thousandth of solid density. The black curve represents the “droplet" saturation curve while the red curve is the “bubble" saturation curve, both computed with Maxwell's algorithm. This phase diagram has been tabulated, and plasma properties are obtained by linear interpolation between the temperature points and logarithmic interpolation between the density points. As the solid phase is described by the 0D a-spot model, this EOS is only used for the plasma.

To compute the transports properties, a modified Lee-More model has been implemented in the plasma model [86], that is able to predict the evolution of the conductivity of the metal from the solid to the plasma state. For example, Figure 5.4 shows the conductivity ($\mathrm{S\,m^{-1}}$ ) of the iron plasma in a wide range of densities and temperatures. It can be seen that for the solid density, the decreasing conductivity with temperature is obtained by the model along with a small discontinuity near the melting point. For plasma densities, the conductivity is very small when the temperature is below 8000 K, and is around $10^4\,\mathrm{S\,m^{-1}}$ for typical thermal plasmas. The fast conductivity decrease with density observed for temperatures close to the boiling point ($\simeq$ 3000 K) is the widely known conductor-insulator transition for metals, that is of primary importance in the context of the explosion of conductors subject to important and transient pulsed currents [87][65].

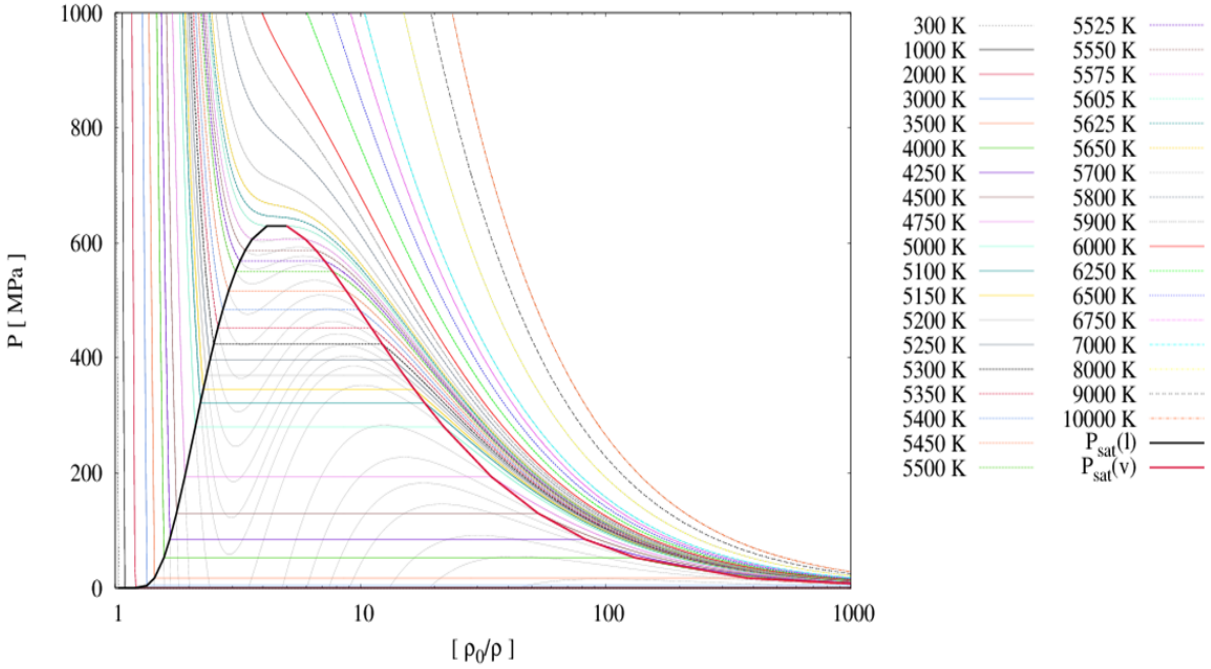


Figure 5.3: Quotidian Equation OF State (QEOS) for iron.

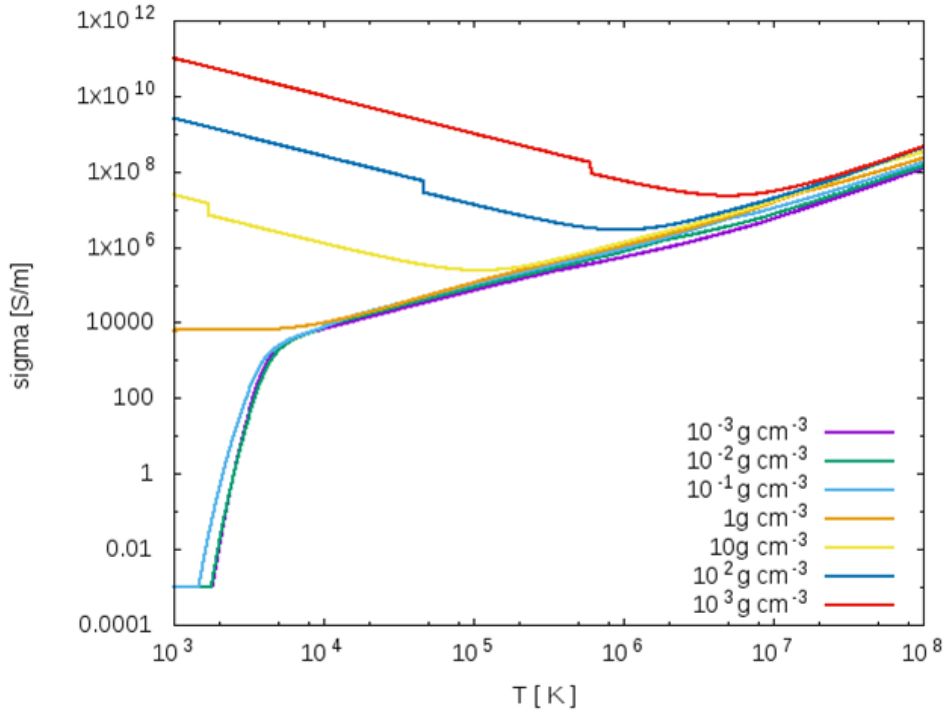


Figure 5.4: Modified Lee-More conductivity model for iron.

## 5.3 Effect of the plasma expansion on the resistance

With the decrease of the solid a-spot radius $a$, and the increasing mass of vaporized metal, a redistribution of the current is expected. As shown by Figure 5.4, the conductivity of the plasma can vary with density and temperature by orders of magnitude and in a non-linear way . As a consequence, it is not straightforward to know if, for a given vaporised mass, the resistance of the plasma region is increasing or decreasing during expansion.

If no Joule heating in the plasma is accounted for, the plasma temperature remains close to the boiling temperature of the metal. Then, it is expected that the plasma conductivity should decrease with decreasing density during plasma expansion. However, $r_\mathrm{p}$ being increased during expansion, the plasma section increases. Following Equation 5.6, the evolution of the plasma resistance $R_\mathrm{p}$ results from the competition between the decreasing conductivity and the increasing $r_\mathrm{p}$.

To focus on the dynamics of $R_\mathrm{p}$ during plasma expansion, Figure 5.5 shows the resistance of a cylindrical plasma with constant mass, a constant internal energy and for different radii, obtained with the QEOS and Lee-More models. The total mass and internal energy of the iron plasma correspond to a cylindrical a-spot of radius $a = 400\,\mu\mathrm{m}$ that has been fully vaporized. The plasma expansion radius varies in the range $500\,\mu\mathrm{m}$ to $4000\,\mu\mathrm{m}$. It can be observed that the resistance first increases due to the decrease of the plasma conductivity when the density decreases. However, the resistance reaches a maxi-

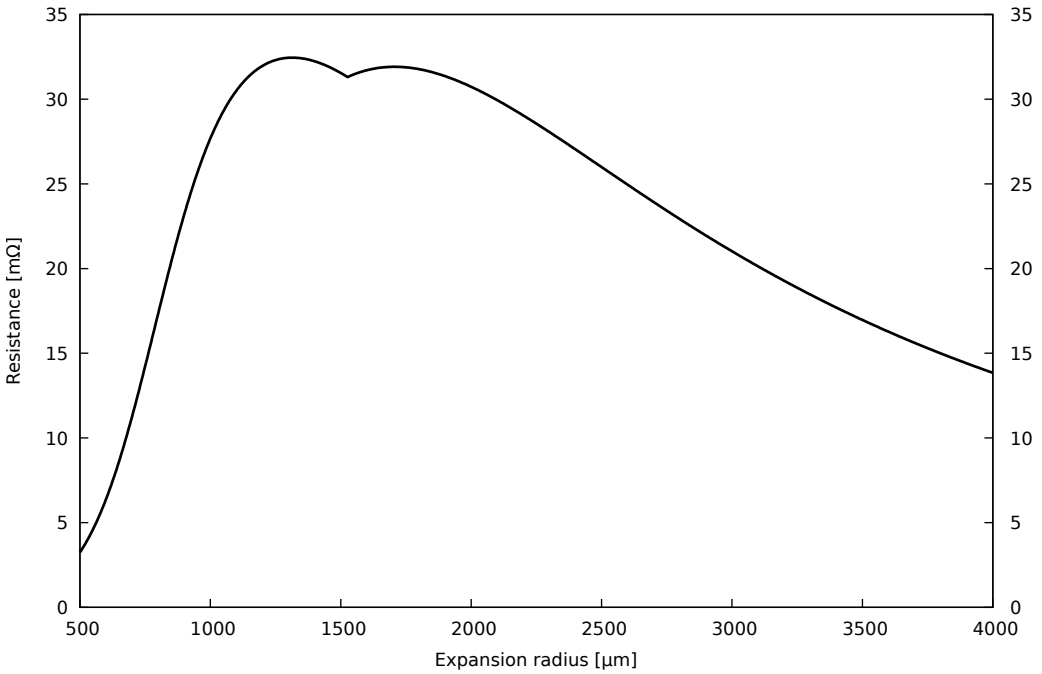


Figure 5.5: Resistance of a cylindrical iron plasma region for different radii and for a constant length $l = 800\,\mu\text{m}$. The iron mass is taken equal to the mass corresponding to a solid cylinder of radius $a = 400\,\mu\text{m}$, and the plasma internal energy is taken equal to the energy required for this mass to be fully vaporised at atmospheric pressure.

mum value before decreasing: The decrease in conductivity is non linear, and it decreases less and less for lower densities. In this case, there is a critical expansion radius from which the decrease of the conductivity can not balance the increase of the plasma section, and the total resistance decreases with the plasma expansion. This simple example shows the importance of taking into account the non-linearity of the plasma properties with density. In the following section, this non-linearity will be coupled with thermal aspects, including the Joule power dissipated in the plasma as the current starts to flow through it.

## 5.4 A-spot subject to a D-wave for a constant confinement pressure

The plasma expansion model is used to observe the current re-distribution when a single iron a-spot contact is subject to a D-wave and a plasma is formed around the a-spot. The considered a-spot has initially a radius $a = 400\,\mu\text{m}$, a constant thickness $l = 800\,\mu\text{m}$, and the confinement pressure has been chosen equal to 50 bar. Figure 5.6 shows the evolution of the radius of the a-spot and the expansion radius of the plasma (left part), and the evolution of the expansion velocity $v_{\text{exp}}$ along with the speed of sound in the plasma $c_{\text{p}}$

(right part).

The first phase of the simulation exactly follows the evolution of the a-spot's temperature and physical properties as in Chapter 2, until the vaporization at the periphery of the a-spot begins at 1.4 µs. Then, the a-spot radius starts decreasing while the radius of the vaporized metal radially expands. The expansion of the plasma increases sharply between 2 and 2.2 µs, due to the fast collapse of $a$ and the current redistribution from the a-spot to the plasma. From the evolution of the expansion velocity, it can be observed that $v_{\text{exp}}$ progressively increases until it reaches the speed of sound in the plasma. During the first 2 µs, the expansion is driven by the vaporization rate and $r_{\text{p}}$ is constrained by the pressure equilibrium condition (5.3). However, the energy deposited in the plasma increases so fast that as soon as $v_{\text{exp}} = c_{\text{p}}$, the plasma can not expand fast enough to maintain the pressure equilibrium with the confining medium and becomes over-pressurised.

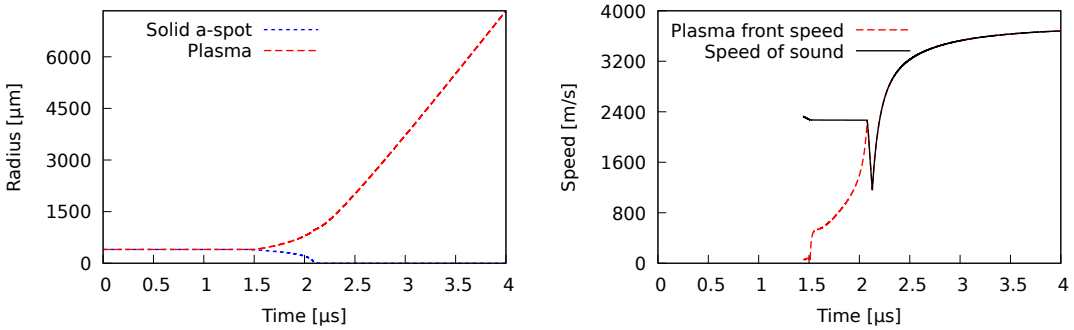


Figure 5.6: A-spot subject to a D-wave, $a = 400\,\mu\text{m}$, $l = 800\,\mu\text{m}$. Left: Decrease of the a-spot's radius and increase of the expansion radius of the plasma. Right: Comparison of the expansion speed with the speed of sound in the plasma.

Figure 5.7 shows the evolution of the plasma pressure: The pressure rises up to a peak value of 35 000 bar at $t = 2.4$ µs, when the solid a-spot is fully vaporised and no more iron mass can be added to the plasma region. Then the plasma pressure decreases due to expansion, despite the important Joule heating. This plasma pressure being much higher than $P_{\text{conf}}$, it expands radially with a dynamics that barely depends on the confinement pressure until the conditions for pressure equilibrium are fulfilled again.

An important observation with this model is that the pressure equilibrium condition is fulfilled only during a rather small duration. This gives confidence in the fact that the chosen confinement pressure $P_{\text{conf}}$ is not a crucial parameter, the expansion being quickly limited by the speed of sound in the metallic plasma. This conclusion remains true even in the case of a constant expansion volume: if the expansion volume is not too small compared to the volume of the a-spot, the first stage of the plasma dynamics is driven by the over-pressure and speed of sound in the plasma.

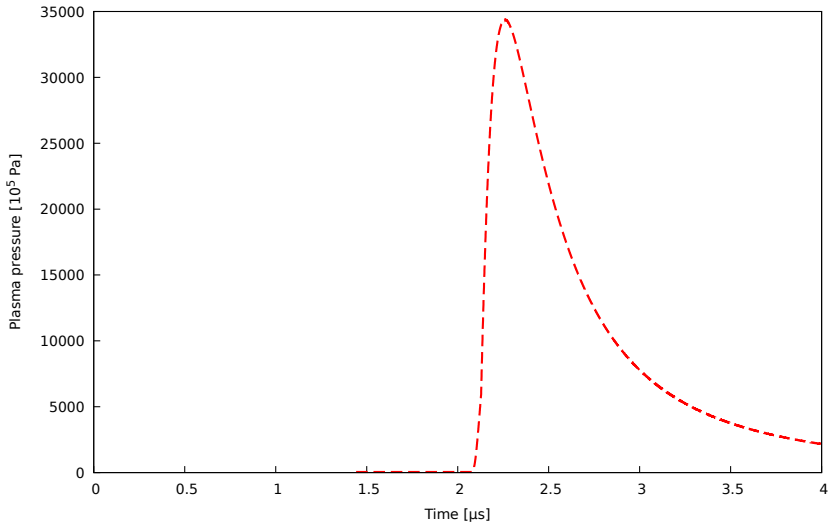


Figure 5.7: A-spot subject to a D-wave, $a = 400\,\mu\text{m}$, $l = 800\,\mu\text{m}$. Evolution of the pressure in the plasma formed by the vaporization of the a-spot.

One could think that the plasma density could increase due to the mass source term induced by the vaporization of the a-spot. However, Figure 5.8 shows that the density in the plasma continuously decreases due to expansion, despite the formation of plasma. The plasma density decreases sharply between 1.4 µs and 2.4 µs at the beginning of the plasma expansion, but then this decrease rate is much lower. Indeed, the propagation front being limited by the speed of sound, a higher plasma radius means a proportionally lower volume decrease. The vaporization rate $-\partial_t a$ ($\text{m}\,\text{s}^{-1}$) is then much lower than the expansion velocity $v_{\text{exp}}$ of the plasma.

The same figure shows the evolution of the total specific energy of the plasma as well as the specific kinetic energy. The total specific energy increases with time, particularly as soon as the a-spot is fully vaporized. During this phase, all the D-wave current flows through the plasma, and the total energy increases due to the Joule power. The kinetic energy is around 20 % of the total energy, the remaining 80 % being representative of the internal energy of the plasma $U_{\text{p}}$. The only energy loss for the plasma is the work of the hydrodynamic forces due to the confinement pressure $P_{\text{conf}}$, but it has been checked that it never exceeds 10 % of the energy deposited by Joule effect. This observation is consistent with the observed dynamics that barely depends on the confinement pressure.

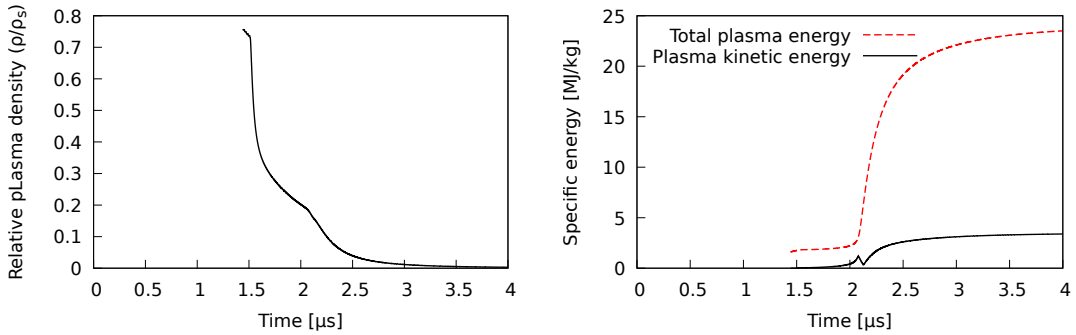


Figure 5.8: A-spot subject to a D-wave, $a = 400\,\mu m$ and length $l = 800\,\mu m$. Gas density relatively to the solid metal (left), and increasing energy plasma (right).

Figure 5.9 shows the evolution of the plasma temperature and ionization degree during the vaporization of the a-spots and the plasma expansion. The plasma temperature is given by the QEOS model from the density and the specific internal energy of the plasma. The temperature of the a-spot increases up to the vaporisation threshold $T_{vap} = 3150\,K$ and the beginning of the biphasic liquid-vapor region at $t = 1.4\,\mu s$. The plasma generated by vaporization has initially the same temperature, but slightly cools down during the first expansion between 1.4 and 2.1 µs. When the radius of the a-spot becomes so small that most of the current flows into the plasma, a large temperature increase can be observed, with an asymptotic convergence to a maximum value of about 20 000 K.

The ionization degree $Z$ of the plasma, which means the average number of free electrons per atom, reveals an interesting evolution: during the first microseconds, $Z$ seems directly related to the density: the fast density decrease at the beginning of the vaporization induces a fast decrease of the ionization degree from $Z = 3.5$, which is representative of the solid metal in standard conditions, to a minimum value of $Z \simeq 1$ at $t = 2.5\,\mu s$. This evolution of $Z$ with density while the temperature remains almost unchanged is predicted by the Thomas-Fermi ionization model implemented in the QEOS method, and representative of the conductor-insulator transition. This evolution of the ionization degree has a direct repercussion on the plasma conductivity, represented on Figure 5.10. Due to the intense Joule heating and the temperature increase in the plasma, thermal ionization takes place and $Z$ increases slightly after 3 µs. The conductivity then reaches a value around $10^4\ S\,m^{-1}$, representative of thermal, ideal metallic plasmas at thermodynamic equilibrium [66].

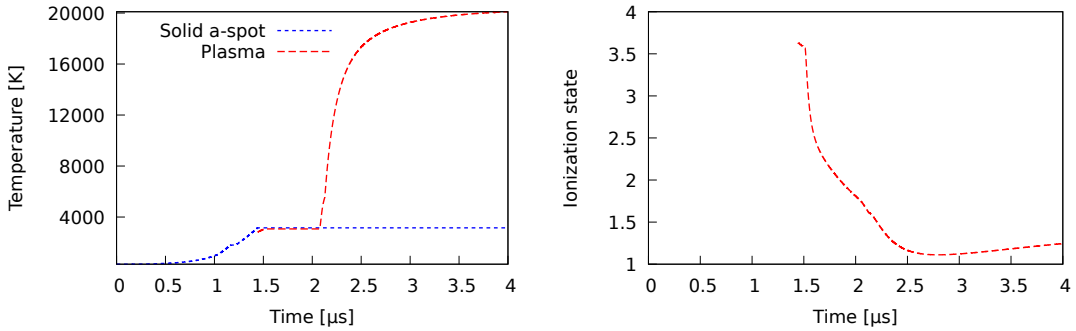


Figure 5.9: A-spot subject to a D-wave, $a = 400\,\mu m$ and length $l = 800\,\mu m$. Gas temperature (left), and ionization degree (right).

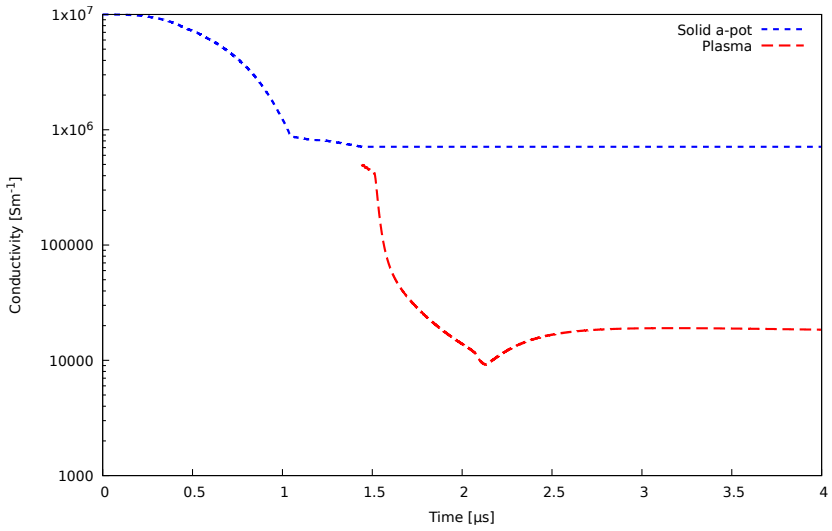


Figure 5.10: A-spot subject to a D-wave, $a = 400\,\mu m$ and length $l = 800\,\mu m$. Plasma and solid conductivities.

The vaporization of the a-spot, the plasma expansion and conductivity evolution lead to the resistance values and current distributions represented on Figure 5.11. It can be observed that the plasma progressively becomes the preferential path for the total imposed current. The a-spot resistance goes to infinity as it is fully vaporized, but the total resistance, represented by a black line, remains lower than $30\,m\Omega$. The Holm constriction resistance has a negligible contribution in this particular situation. The first requirement for the plasma model, that should prevent the divergence of the contact resistance when a-spots are fully vaporized, is respected.

The corresponding electric-field is represented on Figure 5.12. The evolution is very similar to the total resistance, and the electric field reaches a maximum value of $3.3\,MV\,m^{-1}$ at $2.2\,\mu s$, which is comparable to the breakdown field in air at atmospheric pressure. Then discharge phenomena induced by the field in the contact may ignite and propagate. The formation of such a plasma discharge is rather complex to address since it is concomitant

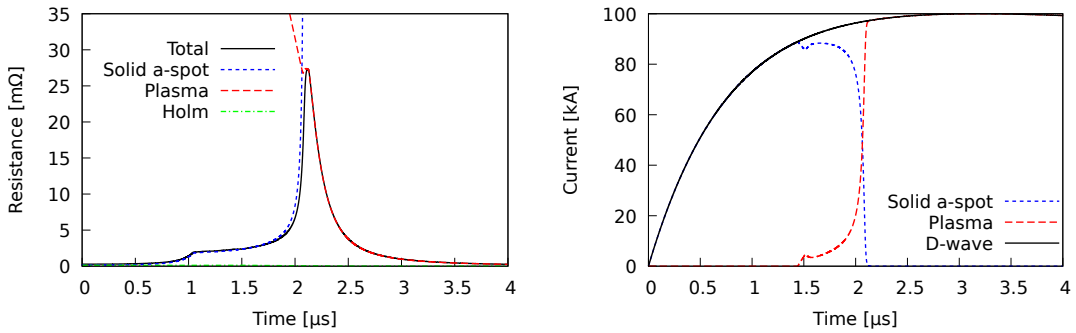


Figure 5.11: A-spot subject to a D-wave, $a = 400\,\mu m$ and length $l = 800\,\mu m$. Gas and a-spot resistance (left), current distribution (right).

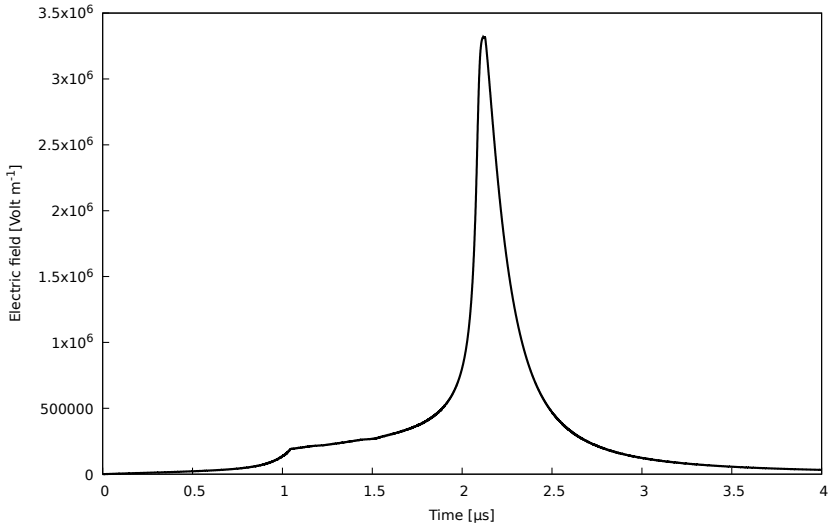


Figure 5.12: Evolution of the electric field at the border of an a-spot subject to a D-wave, $a = 400\,\mu m$, $l = 800\,\mu m$.

to the formation of significant volumes of metallic plasma. As a first step, only the metallic plasma generated by the vaporization of the a-spot will be considered as a source for critical discharges.

## 5.5 A-spot subject to a D-wave with constant expansion volume: parametric study

In this part, a single a-spot contact is still considered, but the plasma is assumed to expand in a constant expansion volume of $15\,mm^3$. This value is well representative of the internal gaps in aeronautic assemblies, as represented on Figure 5.2. A parametric study is conducted on the initial contact resistance, ranging from $0.1\,m\Omega$ to $0.5\,m\Omega$. This initial resistance is directly related to the a-spot radius according to Equation 5.16, such

that larger initial resistances mean a smaller a-spot radius.

$$R = \frac{1}{2a\sigma} + \frac{l}{\sigma\pi a^2} = \frac{1}{a\sigma}\left[\frac{1}{2} + \frac{2}{\pi}\right] \tag{5.16}$$

The final plasma pressure and internal energy have been computed in each case to compare the criticity of the different discharges to the initial contact resistance. One could naively think that a higher initial resistance would necessarily lead to a higher dissipated Joule power in the plasma. Figure 5.13 shows that it is not the case.

The same conclusions are obtained when considering the total vaporized volume or the pressure in the confinement volume at the end of the wave: Figure 5.14 represents the volume of vaporized metal as a function of the initial resistance. From 0.1 mΩ to 0.146 mΩ, the corresponding a-spots are too big for the vaporization to occur: the temperature of the a-spot rises but never reaches the boiling threshold because the volume has a too large thermal capacity. From 0.146 mΩ to 0.183 mΩ, the total energy dissipated in the plasma increases, reaches a peak, and then decreases again. From the value of 0.183 mΩ to 0.5 mΩ, the a-spot is small enough to be fully vaporised by the D-wave. Then its resistance has a behaviour similar to the evolution of the resistance presented on Figure 5.11.

However, the peak occurs faster in the case of a small a-spot. Considering the total energy dissipated in the plasma, it means that the contact spends less time at high resistance. When the peak of the D-wave current occurs at 3 µs, the resistance peak is already past for smaller a-spots. The integral of the Joule power is therefore lower for smaller a-spots, even if they correspond to higher initial and resistances. The final pressure in the cavity is depicted on Figure 5.15. The maximal pressure is obtained for $R = 0.2\,\mathrm{m\Omega}$, and is close to 40 000 bar.

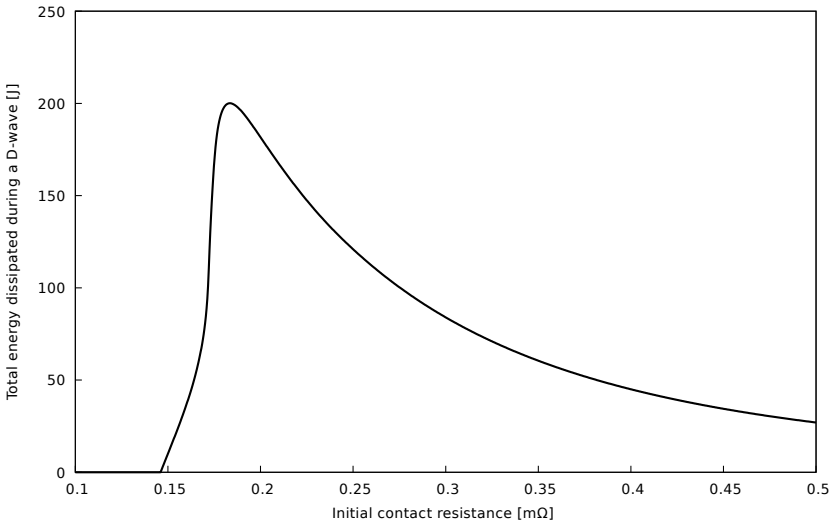


Figure 5.13: Total energy dissipated in the plasma by Joule effect as a function of the initial resistance of a single a-spot contact subject to a D-wave.

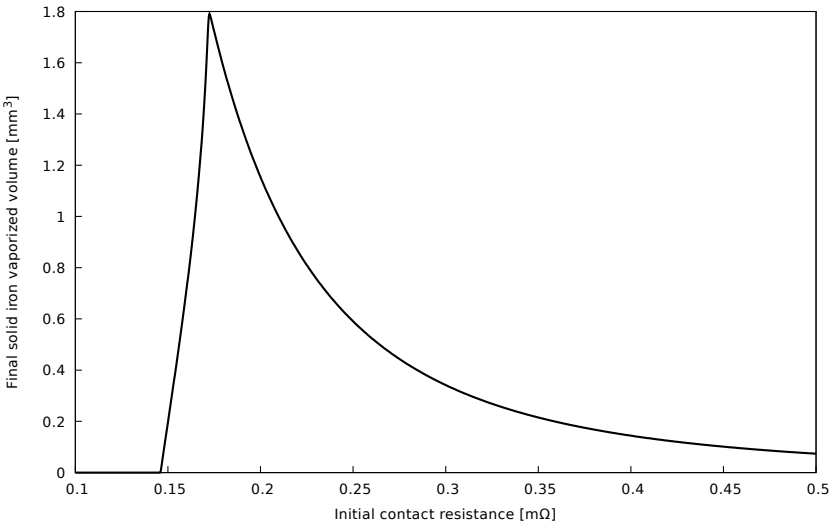


Figure 5.14: Volume of vaporized metal as a function of the initial resistance of a single a-spot contact subject to a D-wave.

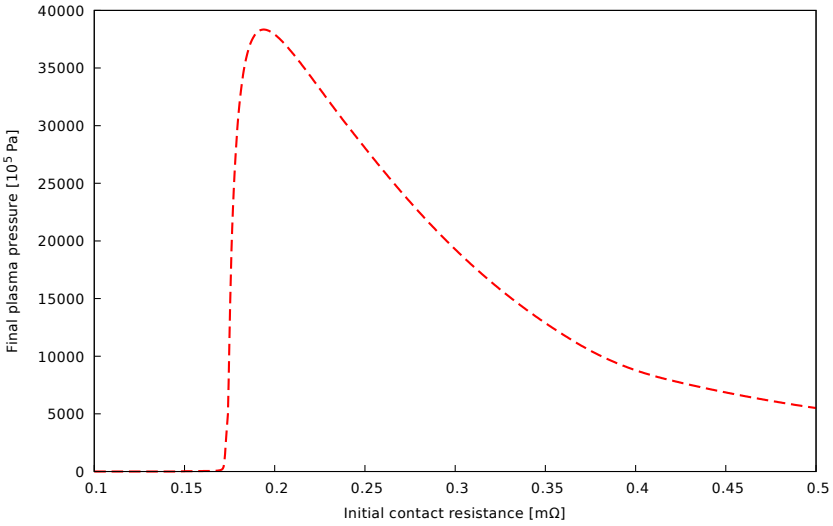


Figure 5.15: Final plasma pressure in a confinement volume of 15 mm$^3$ as a function of the resistance of a single a-spot contact subject to a D-wave.

## 5.6 Conclusion

The plasma expansion model developed in this chapter makes it possible to compute the final pressure, vaporized volume, and energy release in a plasma discharge ignited in a contact subject to a lightning current. Due to the complex evolution of plasma properties with density and temperature, the discharge characteristics may evolve non-linearly with the “low-level" contact resistance. This non linear behaviour has non intuitive consequences regarding the sparking risk in aeronautic contacts. Then, the simple plasma

model could be used to perform comparisons with experimental measurements, first and foremost on the sparking ignition threshold in assemblies subject to lightning currents. It could also be used to estimate the maximum pressure that may be encountered in a given geometry, and evaluate the design of a fastener regarding the constraints induced by lightning strikes to aircraft.

# Chapter 6

# Conclusion

This PhD project intended to develop a simple model for the the non-linear evolution of metal-metal contacts in aeronautic assemblies subject to lightning stroke conditions. The main goals for such a model should be:

- To predict the observed non linear evolution of the contact resistance for high current levels. The assessment of this non-linear evolution on microsecond time-scales is crucial for the prediction of current distributions in assemblies and aeronautic structures.
- To be fast and simple enough to couple as an interface model in 3D finite volume numerical codes and large-scale electromagnetic simulations.
- To predict the conditions for the ignition of critical energetic discharges in assemblies subject to lightning stroke. *Inter alia*, it should be able to reckon the risk of “sparking" and “outgasing" in fastened assemblies.
- To provide insight into the fundamental physical processes occurring at the microscopic scale in contacts. The model should be able to perform parametric studies to evaluate the influence of the micro-geometry and the material properties on the contact dynamics.

In the first chapter, a general overview of lightning strikes to aircraft was conducted, and the most relevant experimental results were highlighted: The contact resistance in assemblies may vary by orders of magnitude on microsecond time-scales, and such variations can be associated in some cases to the ignition of discharges. Then, after a brief overview of the science of electric contacts, some approximative estimates revealed that electromigration and electronic emission can be neglected in metal-metal contacts subject to the pulsed arc phase of lightning strokes.

In the second chapter, the main geometric hypothesis performed in this work were presented: a-spots were assumed to be small cylinders joining the two parts in a contact,

characterized by a radius $a$, and a thickness $l$. Then the multi-physical modelling of a single a-spot contact was emphasized:

- A 2D axisymmetric finite volume code have been developed to solve the complex thermo-electric coupling in a-spots subject to lightning currents.
- The current conservation equation with Seebeck effect was solved, together with the unsteady Fourier's equation with thermal conduction and Joule effect taken into account.
- The material properties vary with the temperature, and phase transitions are taken into account when melting and boiling points are reached.
- The main outputs of this model are the evolution of the contact electrical resistance and the a-spot's vaporization dynamics.

Meaningful conclusions are the significant decrease of the electric conductivity with temperature, that promotes alongside with thermal conduction a uniform heating of the a-spot up to the boiling point. Then, it has been observed that as soon as boiling starts, a fast vaporization front ignites at the rim of the a-spot and propagates to the axis, resulting in the collapse of the radius and the exponential increase of the contact resistance.

Based on these results, a simple 0D thermo-electric model for an a-spot has been derived that is able to reproduce the vaporization dynamics observed with 2D simulations for similar conditions. Furthermore, a crucial physical phenomena came into view that needed to be added to the model: the mechanical crushing of the a-spot due to the presence of a tightening force in the contact. The 0D model has been enriched with a simple elasto-plastic mechanical model with temperature dependant Young modulus and yield strength. A critical result consists in the very different dynamics observed between contacts with constant tightening force and contacts with constant tightening distance:

- For a constant tightening distance, the temperature increases and the electric resistance of the a-spot can only increase due to the temperature decreasing conductivity of the metal. If the boiling point is reached, the vaporization of the a-spot is unavoidable and the resistance is diverging.
- For a constant tightening force, the resistance first increases due to temperature decreasing conductivity. However, when the temperature reaches a critical value close to the melting point, the mechanical properties of the metal collapse leading to a fast flattening dynamics of the a-spot. In this case the electrical resistance decreases down to values that can be one or two orders of magnitude lower than the initial resistance. No vaporization takes place, and the two parts are partially welded together.

- Mechanical situations in-between constant tightening force or distance may lead to hybrid scenarios that could explain some of the puzzling measurements of the evolution of the contact resistance in aeronautic assemblies subject to high current values.

After this first work on a single a-spot contact, the modelling of multi-spot contacts have required a particular effort. The difficulty relied on two points:

- To describe the physical interactions between the a-spots in a contact: The many a-spots in a contact may interact mechanically and electrically, resulting on different load and current distributions between them, that can modify the overall contact dynamics.

- To provide a description of a the micro-geometry of the surfaces in a contact: It is mandatory to be able to predict a realistic a-spot distribution in a contact for given roughness parameters, tightening load, and “low level" contact resistance.

To address these difficult points, 3D electrostatic simulations have been performed to study the electrostatic interactions between several a-spots in a contact, leading to the conclusion that the “Greenwood" interaction could be ignored as a first approximation, as long as a-spots are separated by at least 20 times their radii. Then the influence of capacitive and inductive effects on the current distribution between the a-spots has been highlighted. The former is largely negligible for the time-scales of interest, while the latter has to be considered for contacts with large a-spots and large separating distances higher than 1 mm. This situation has been avoided for all the contacts considered in this work, and the inductive effects neglected. Then the interaction between the a-spots is modelled with a simple current divider approach.

To tackle the geometric complexity of the surfaces in a contact, an approach very similar to Schoft's [40] has been considered:

- Surfaces are described with the roughness parameters $R_\mathrm{a}$, $R_\mathrm{q}$ and $N_\mathrm{s}$, that can be measured by surface profilometry.

- A Gaussian distribution for the height $l$ of the $N_\mathrm{s}$ micro-peaks on a surface is considered, with $R_\mathrm{a}$ and $R_\mathrm{q}$ as the mean height and height deviation.

- A cylindrical shape is assumed for the different micro-peaks, with same height $l$ and with an aspect ratio $l/(2a)$ equal to unity.

- The cylindrical micropeaks may form cylindrical a-spots in a contact.

- A dichotomy algorithm has been developed to find the proper tightening distance between the surfaces that ensure a given load or a given contact resistance.

This model has been validated by simulating the typical contact resistance decrease when the tightening force increases. Then multi-spot contacts have been studied into details, and particularly the influence of the surface micro-geometry on the contact dynamics:

- First it has been observed that multi-spot contacts with constant tightening distance have a vaporization dynamics very similar to single a-spot contacts. In this case the current redistribution between the a-spots is moderated, but allows an almost simultaneous vaporization of the a-spots despite their different sizes. Indeed, small a-spots were expected to vaporize before the bigger ones, but the decreasing conductivity with temperature strongly mitigates this effect.

- For multi-spot contacts with constant tightening forces, important current redistributions take place: Due to the flattening dynamics of the a-spots, new a-spots are created since more and more micro-peaks may interfere with the mating surface.

- Due to the complex interactions and current redistributions between the a-spots, $R_{\mathrm{q}}$ and $R_{\mathrm{a}}$ have a limited impact on the contact dynamics. Only a larger $R_{\mathrm{a}}$ value seems to significantly modify the decreasing rate of the contact resistance during mechanical flattening, but the overall dynamics seem quite universal and barely depend on the detailed microgeometry.

Finally, it appears from this work that contacts with constant tightening distance are the most favorable locations for discharge ignition due to the high electric-fields and a-spot vaporization. To tackle the complex problem of discharge ignition in contacts with constant tightening distance, a simple plasma model have been derived. There were basically three main goals for this model:

- To prevent the non-physical diverging contact resistance and electric-field during the full vaporization of the a-spots in contacts with a constant tightening distance.

- To compute the current redistribution from the a-spots to the plasma that may occur due to vaporization.

- To evaluate physical parameters that are useful in the context of the discharge risk in aeronautic assemblies: the plasma discharge energy, the total vaporized volume of metal, the final over-pressure in the plasma after its expansion in some confining volume.

To match these requirements, the description of the plasma relied on two models:

- An expansion model: The plasma is assumed axisymmetric around the a-spot with an expansion radius $r_{\mathrm{p}}$. $r_{\mathrm{p}}$ is computed assuming a pressure equilibrium with the

confining media, and its variation is limited by the speed of sound in the plasma. The total energy in the plasma is conserved, and two source terms are taken into account: the formation of plasma due to the vaporization of the a-spot, and the Joule heating in the plasma. The only energy loss taken into account in this model is the work of the hydrodynamic pressure forces due to the confining media.

- A QEOS (Quotidian Equation of State) and a Lee-More conductivity model to compute the thermodynamic and transport properties of the plasma in a wide range of temperatures, from solid density to kinetic thermal plasmas at atmospheric pressure.

This model has been used on a single a-spot, and the plasma expansion have been successfully simulated for a constant confining pressure of 50 bar. The electric conductivity of the plasma evolves in a highly non-linear way, with a first decrease due to expansion and the widely known conductor-insulator transition, followed by an increase due to the thermal ionization as soon as a significant current flows through the plasma. The resulting contact resistance is then characterized by a peak value and a fast decrease due to the increasing section of the plasma during expansion.

Then, a parametric study has been conducted considering different initial contact resistances and a given confinement volume of $15\,\mathrm{mm}^3$. At first, the vaporized volume, the final energy released in the discharge and the final over-pressure increase with the initial contact resistance. Surprisingly, it finally reaches a maximum followed by a slow decrease. In this case a higher initial contact resistance means a less energetic discharge. Those interesting and non-intuitive results prove the utility of such discharge model, and represent a first step to a better understanding of the discharge phenomena in the confined media of aeronautic assemblies.

For future works, three important steps should be considered:

- Quantitative comparisons with experimental studies an a single a-spot contact: An experimental set-up should be specifically designed to ensure a controlled geometry, tightening force or distance, and current. High speed electrical diagnostics would be needed to follow the potentially fast evolution of the contact resistance.

- Experimental characterization of the discharges in a contact: It seems important to use emission spectroscopy to identify unequivocally if a given discharge is an air plasma, related to a field induced breakdown, or an outgasing phenomena, involving a metallic plasma generated by the vaporization of the a-spots.

- The 0D contact model with plasma should be coupled as an interface model in the 3D finite volume codes of unit FPA, such as *Taranis*, to study into details complex geometries with many contacts. Such an approach would make it possible to take into account the current redistributions between contacts in fastened assemblies together with inductive effects.

- Improve the 0D model to be able to take into account contacts made of different metallic materials, and the presence of film layers and coatings.
- This PhD project was dedicated to metal-metal contacts, and some efforts would be needed to adapt it for carbon-metal or carbon-carbon contacts. The plasma model could be used with minor modifications, but the thermo-electric and the mechanical models should be thought over in this case.

# Bibliography


[1] A. Watts. *The Weather Handbook*. Bloomsbury USA, 2015.

[2] C.D. Ahrens and P.J. Samson. *Extreme Weather and Climate*. Cengage Learning, 2010.

[3] D. Müller-Hillebrand. Charge generation in thunderstorms by collision of ice crystals with graupel, falling through a vertical electric field. *Tellus*, 6(4):367–381, 1954.

[4] M.A. Uman. *The Lightning Discharge*. Dover Books on Physics. Dover Publications, 2012.

[5] E.M. Bazelyan and Y.P. Raizer. *Lightning Physics and Lightning Protection*. CRC Press, 2000.

[6] Earle R. Williams. The global electrical circuit: A review. *Atmospheric Research*, 91(2):140 – 152, 2009. 13th International Conference on Atmospheric Electricity.

[7] Walter A. Lyons. *the meteorology of transient luminous events-an introduction and overview*. Springer Netherlands, Dordrecht, 2006.

[8] R G Harrison. Fair weather atmospheric electricity. *Journal of Physics: Conference Series*, 301:012001, jun 2011.

[9] J. R. Dwyer. The initiation of lightning by runaway air breakdown. *Geophysical Research Letters*, 32(20), 2005.

[10] Danyal Petersen, Matthew Bailey, William H. Beasley, and John Hallett. A brief review of the problem of lightning initiation and a hypothesis of initial lightning leader formation. *Journal of Geophysical Research: Atmospheres*, 113(D17), 2008.

[11] A.V. Gurevich, K.P. Zybin, and R.A. Roussel-Dupre. Lightning initiation by simultaneous effect of runaway breakdown and cosmic ray showers. *Physics Letters A*, 254(1):79 – 87, 1999.

[12] Gennady Milikh and Robert Roussel-Dupre. Runaway breakdown and electrical discharges in thunderstorms. *Journal of Geophysical Research*, 115, 12 2010.

[13] Vladislav Mazur and Lothar H. Ruhnke. Model of electric charges in thunderstorms and associated lightning. *Journal of Geophysical Research: Atmospheres*, 103(D18):23299–23308.

[14] Gallimberti, I. The mechanism of the long spark formation. *J. Phys. Colloques*, 40:C7–193–C7–250, 1979.

[15] Vernon Cooray and Vladimir Rakov. On the upper and lower limits of peak current of first return strokes in negative lightning flashes. *Atmospheric Research*, 117:12 – 17, 2012. Special Issue dedicated to the 30th International Conference on Lightning Protection (ICLP).

[16] Jean-François Ripoll, John Zinn, Christopher A. Jeffery, and Patrick L. Colestock. On the dynamics of hot air plasmas related to lightning discharges: 1. gas dynamics. *Journal of Geophysical Research: Atmospheres*, 119(15):9196–9217.

[17] Vladimir A. Rakov and Martin A. Uman. *Lightning: Physics and Effects*. Cambridge University Press, 2003.

[18] Vladislav Mazur. Physical processes during development of lightning flashes. *Comptes Rendus Physique*, 3(10):1393 – 1409, 2002.

[19] Franklin A. Fisher and Anderson J. Plurner. *Lightning Protection of Aircraft*. NASA, 1979.

[20] Ch. Jones, D. Rowse, and G. Odam. Evaluation of nugget formation in resistance spot welding of dissimilar materials. In *Conference on Lightning and Static Electricity*, Seattle, 2001.

[21] D. Morgan, C.J. Hardwick, S.J. Haigh, and A.J. Meakins. The Interaction of Lightning with Aircraft and the Challenges of Lightning Testing. *AerospaceLab*, (5):p. 1–10, December 2012.

[22] Aircraft lightning environment and related test waveforms. Technical report, SAE Aerospace, 2005.

[23] Anders Larsson. The interaction between a lightning flash and an aircraft in flight. *Comptes Rendus Physique*, 3(10):1423 – 1444, 2002.

[24] Laurent Chemartin. *Modélisation des arcs électriques dans le contexte du Foudroiement des aéronefs*. PhD thesis, Université de Rouen, 2008.

[25] P. Lalande, A. Bondiou-Clergerie, and P. Laroche. Analysis of available in-flight measurements of lightning strikes to aircraft. In *SAE Technical Paper*. SAE International, 06 1999.

[26] B.A. Whiting, A.C. Day, Q.N. Le, C.E. Anway, and R.B. Greegor. Finite element simulation and experimental analysis of edge glow for a generic, 16-ply carbon fiber reinforced plastic composite laminate. In *ICOLSE 2015 Conference Proceedings*, pages 9 .–9 ., September 2015.

[27] http://www.stuff.co.nz.

[28] http://www.code-saturne.org.

[29] L. Chemartin, Philippe Lalande, Bruno Peyrou, Arnaud Chazottes, P. Q. Elias, Clarisse Delalondre, B. G. Chéron, and Frederic Lago. Lightning hazards to aircraft and launchers direct effects of lightning on aircraft structure : Analysis of the thermal , electrical and mechanical constraints. 2012.

[30] F Lago. Lightning in aeronautics. *Journal of Physics: Conference Series*, 550(1):012001, 2014.

[31] Aircraft lightning zoning. Technical report, SAE Aerospace, 2005.

[32] G. Sweers, B. Birch, and J. Gokcen. Lightning strikes: protection, inspection and repair. *Boeing Aero Magazine*, 2012.

[33] Aircraft lightning test methods. Technical report, SAE Aerospace, 2005.

[34] Rafael Sousa Martins. *Etude expérimentale et théorique d'un arc de foudre et son interaction avec un matériau aéronautique*. PhD thesis, Ecole Centrale Paris, 2017.

[35] *Bibliography and Adstract on Electrical Contacts 1835-1951*. ASTM International.

[36] *Electrical Contacts - 2017: Proceedings of the Sixty-third IEEE Holm Conference on Electrical Contacts : Held 10-13 September 2017, the Brown Palace Hotel and Spa, Denver, CO, USA*. IEEE, 2017.

[37] G. Windred. *Electrical Contacts, by G. Windred, ...* Macmillan, 1940.

[38] R. Holm. *Electric contacts: theory and applications*. Springer Verlag GmbH, fourth edition, 1967.

[39] P.G. Slade. *Electrical Contacts: Principles and Applications*. Electrical and Computer Engineering. Taylor & Francis, 1999.

[40] S. Schoft. Joint resistance depending on joint force of high current aluminum joints. In *Proceedings of the 50th IEEE Holm Conference on Electrical Contacts and the 22nd International Conference on Electrical Contacts Electrical Contacts, 2004.*, pages 502–510, September 2004.

[41] P.-Y. Duvivier. *Etude expérimentale et modélisation du contact électrique et mécanique quasi statique entre surfaces rugueuses d'or : application aux micro-relais.* PhD thesis, École Nationale Supérieure des Mines de Saint-Étienne, Octobre 2012.

[42] R. A. Coutu Jr., J. W. McBride, and L. A. Starman. Improved micro-contact resistance model that considers material deformation, electron transport and thin film characteristics. In *2009 Proceedings of the 55th IEEE Holm Conference on Electrical Contacts*, pages 298–302, September 2009.

[43] S. Majumder, N. E. McGruer, and G. G. Adams. Adhesion and contact resistance in an electrostatic mems microswitch. In *18th IEEE International Conference on Micro Electro Mechanical Systems, 2005. MEMS 2005.*, pages 215–218, January 2005.

[44] Y. Liu, G. Zhang, H. Qin, Y. Geng, J. Wang, J. Yang, and K. Zhao. Prediction of the dynamic contact resistance of circuit breaker based on the kernel partial least squares. *IET Generation, Transmission Distribution*, 12(8):1815–1821, 2018.

[45] Bok-Ki Kim, Kuo-Ta Hsieh, and F. X. Bostick. A three-dimensional finite element model for thermal effect of imperfect electric contacts. *IEEE Transactions on Magnetics*, 35(1):170–174, January 1999.

[46] Takaya Kobayashi and Yasuko Mihara. Evaluation of nugget formation in resistance spot welding of dissimilar materials. In *SIMULIA Community Conference*, November 2014.

[47] G.M. Rebeiz. *RF MEMS: Theory, Design, and Technology.* Wiley, 2004.

[48] R. D. Malucci. The impact of spot size and location on current density. In *2009 Proceedings of the 55th IEEE Holm Conference on Electrical Contacts*, pages 208–213, September 2009.

[49] J. R. Black. Electromigration—a brief survey and some recent results. *IEEE Transactions on Electron Devices*, 16(4):338–347, April 1969.

[50] E. L. Murphy and R. H. Good. Thermionic emission, field emission, and the transition region. *Phys. Rev.*, 102:1464–1473, Jun 1956.

[51] V. Semet, Ch. Adessi, T. Capron, R. Mouton, and Vu Thien Binh. Low work-function cathodes from schottky to field-induced ballistic electron emission: Self-consistent numerical approach. *Phys. Rev. B*, 75:045430, Jan 2007.

[52] W. Kim and Q. J. Wang. Numerical computation of surface melting at imperfect electrical contact between rough surfaces. In *Electrical Contacts - 2006. Proceedings of the 52nd IEEE Holm Conference on Electrical Contacts*, pages 81–88, September 2006.

[53] F. Spayth and S. East. Sliding contacts — a review of the literature. *Electrical Engineering*, 72(10):912–917, October 1953.

[54] Longqiu Li, Wenping Song, Guangyu Zhang, and Dan Jia. An electrical contact resistance model including roughness effect for a rough MEMS switch. *Journal of Micromechanics and Microengineering*, 22(11):115023, oct 2012.

[55] H. Ghaednia, A. Rostami, and R. L. Jackson. The influence of thermal expansion and plastic deformation on a thermo-electro mechanical spherical asperity contact. In *2012 IEEE 58th Holm Conference on Electrical Contacts (Holm)*, pages 1–7, September 2012.

[56] S S Wadwalkar, R L Jackson, and L Kogut. A study of the elastic—plastic deformation of heavily deformed spherical contacts. *Proceedings of the Institution of Mechanical Engineers, Part J: Journal of Engineering Tribology*, 224(10):1091–1102, 2010.

[57] James W. Demmel, Stanley C. Eisenstat, John R. Gilbert, Xiaoye S. Li, and Joseph W.H. Liu. A supernodal approach to sparse partial pivoting. Technical report, SIAM, Berkeley, CA, USA, 1995.

[58] W.M. Haynes. *CRC Handbook of Chemistry and Physics: A Ready-reference Book of Chemical and Physical Data*. CRC-Press, 2009.

[59] http://www.matweb.com.

[60] A. E. Barysevich and S. L. Cherkas. Testing the equation of state and electrical conductivity of copper by the electrical wire explosion in air: Experiment and magnetohydrodynamic simulation. *Physics of Plasmas*, 18(5):052703, 2011.

[61] A. E. Barysevich and S. L. Cherkas. Testing the equation of state and electrical conductivity of copper by the electrical wire explosion in air: Experiment and magnetohydrodynamic simulation. *Physics of Plasmas*, 18(5):052703, 2011.

[62] A. L. Efros and B. I. Shklovskii. Critical behaviour of conductivity and dielectric constant near the metal-non-metal transition threshold. *physica status solidi (b)*, 76(2):475–485, 1976.

[63] Jean-Pierre Clerc, G Giraud, jm Laugier, and Jean-Marc Luck. The electrical conductivity of binary disordered systems, percolation clusters, fractals and related models. *Advances in Physics - ADVAN PHYS*, 39:191–309, 06 1990.

[64] D. Sheftman and Ya. E. Krasik. Evaluation of electrical conductivity and equations of state of non-ideal plasma through microsecond timescale underwater electrical wire explosion. *Physics of Plasmas*, 18(9), September 2011.

[65] G. S. Sarkisov, S. E. Rosenthal, K. R. Cochrane, K. W. Struve, C. Deeney, and D. H. McDaniel. Nanosecond electrical explosion of thin aluminum wires in a vacuum: Experimental and computational investigations. *Phys. Rev. E*, 71:046404, April 2005.

[66] Y Cressault, R Hannachi, Ph Teulet, A Gleizes, J-P Gonnet, and J-Y Battandier. Influence of metallic vapours on the properties of air thermal plasmas. *Plasma Sources Science and Technology*, 17(3):035016, 2008.

[67] Y. P. Varshni. Temperature dependence of the elastic constants. *Phys. Rev. B*, 2:3952–3958, November 1970.

[68] Hayden A. Burgoyne and Chiara Daraio. Strain-rate-dependent model for the dynamic compression of elastoplastic spheres. *Phys. Rev. E*, 89:032203, March 2014.

[69] Gordon R. Johnson and William H. Cook. Fracture characteristics of three metals subjected to various strains, strain rates, temperatures and pressures. *Engineering Fracture Mechanics*, 21(1):31 – 48, 1985.

[70] Mina S. Seif, William E. Luecke, Lisa Y. Choe, Joseph A. Main, Joseph D. McColskey, Chao Zhang, Jonathan M. Weigand, John L. Grossa, and Fahim Sadek. Temperature-dependent material modeling for structural steel: Formulation and application. Technical Report 1907, NIST, April 2016.

[71] O. M. Pavleino, V. A. Pavlov, and M. A. Pavleino. Effect of the spreading of the contact spot on the pulsed heating of electrodes. *Surface Engineering and Applied Electrochemistry*, 47(4):362, September 2011.

[72] J.A. Greenwood. Constriction resistance and the real area of contact. *British Journal of Applied Physics*, 17(12):1621, 1966.

[73] M. Braunovic, N.K. Myshkin, and V.V. Konchits. *Electrical Contacts: Fundamentals, Applications and Technology*. Electrical and Computer Engineering. CRC Press, 2017.

[74] W. Yan and K. Komvopoulos. Contact analysis of elastic-plastic fractal surfaces. *Journal of Applied Physics*, 84(7):3617–3624, 1998.

[75] Prasanta Sahoo and Niloy Ghosh. Finite element contact analysis of fractal surfaces. *Journal of Physics D: Applied Physics*, 40(14):4245, 2007.

[76] Mitutoyo. *Quick guide to surface roughness measurement*, December 2006.

[77] B Peyrou, L Chemartin, Ph Lalande, B G Chéron, Ph Rivière, M-Y Perrin, and A Soufiani. Radiative properties and radiative transfer in high pressure thermal air plasmas. *Journal of Physics D: Applied Physics*, 45(45):455203, 2012.

[78] R M. More, K H. Warren, D A. Young, and G B. Zimmerman. A new quotidian equation of state (qeos) for hot dense matter. *Physics of Fluids*, 31, 10 1988.

[79] A. Ray, M.K. Srivastava, G Kondayya, and S. V. G. Menon. Improved equation of state of metals in the liquid-vapor region. *Laser and Particle Beams*, 24:437 – 445, 09 2006.

[80] E Hückel and P Debye. The theory of electrolytes: I. lowering of freezing point and related phenomena. *Phys. Z*, 24:185–206, 1923.

[81] D. J. McCloskey. An analytic formulation of equations of state. 1964.

[82] Zhi-Guo Li, Yan Cheng, Qi-Feng Chen, and Xiang-Rong Chen. Equation of state and transport properties of warm dense helium via quantum molecular dynamics simulations. *Physics of Plasmas*, 23(5):052701, 2016.

[83] Zhijian Fu, Weilong Quan, Wei Zhang, Zhiguo Li, Jun Zheng, Yunjun Gu, and Qifeng Chen. Equation of state and transport properties of warm dense aluminum by ab initio and chemical model simulations. *Physics of Plasmas*, 24(1):013303, 2017.

[84] Travis Sjostrom, Scott Crockett, and Sven Rudin. Multiphase aluminum equations of state via density functional theory. *Phys. Rev. B*, 94:144101, Oct 2016.

[85] V Mishra, C D Sijoy, P Pahari, and S Chaturvedi. A comparison of quotidian equation of state of aluminium with ab-initio calculations. *Journal of Physics: Conference Series*, 377:012105, jul 2012.

[86] Y. T. Lee and R. M. More. An electron conductivity model for dense plasmas. *The Physics of Fluids*, 27(5):1273–1286, 1984.

[87] Vladimir Oreshkin, R B. Baksht, NA Ratakhin, Alexander Shishlov, Konstantin Khishchenko, P Levashov, and I I. Beilis. Wire explosion in vacuum: Simulation of a striation appearance. *Physics of Plasmas*, 11:4771–4776, 09 2004.

[88] W.R. Smythe. *Static and dynamic electricity*. International series in pure and applied physics. Edwards Brothers Inc., 1936.

# Appendix A

# Holm's formula mathematical steps

This appendix is aimed at developping the mathematical steps that lead to the obtention of Holm's formula, corresponding to the problem of the resistance of a flat contact. It appeared difficult to find the demonstration in the literature, the formula being so widely used that it became unquestioned, as references always point to the important book written by Holm [38]. However, we found Holm's demonstration to be not completely satifying, himself quoting another author, Smythe [88], that developed the mathematical steps in his book, even though they were not specifically aimed at solving the precise problem of conduction through a flat constriction.

The present appendix comprehensively gathers the hypotheses and mathematical steps that lead to Holm's formula. We found this demonstration to be helpful in the understanding of problems that differ somewhat from the ideal case of a single flat a-spot, when borders effect come into play, for instance considering a cylindrical a-spot with a given length, or several a-spots in parallel.

## A.1 When can a set of surfaces be equipotentials

Smythe first exhibits very general conditions required by the structure of a set of regular surfaces to be equipotential surfaces that satisfies the Laplacian equation. These conditions will later be used to find equipotential surfaces that are candidates for the solution regarding a flat constriction. Let us consider the surfaces defined by the set of equations:

$$F(x, y, z) = C \tag{A.1}$$

Each surface of this family corresponds to a given value of $C$. Assuming they are equipotentials, there must be a unique value of the potential $\varphi$ for each surface, and therefore by injection, for each value of $C$. There must exist a function $f$ so that:

$$\varphi = f(C) \tag{A.2}$$

$\varphi$ also remains a function of the space position by $\varphi(x,y,z) = f \circ F(x,y,z)$. The spatial derivatives of the potential are then:

$$\frac{\partial \varphi}{\partial x} = f' \circ F \cdot \frac{\partial F}{\partial x}, \text{ etc.} \qquad \frac{\partial^2 \varphi}{\partial x^2} = f'' \circ F \cdot \left(\frac{\partial F}{\partial x}\right)^2 + f' \circ F \cdot \frac{\partial^2 F}{\partial x^2}, \text{ etc.} \tag{A.3}$$

and the Laplacian of the potential is given by:

$$\Delta \varphi = \frac{\partial^2 \varphi}{\partial x^2} + \frac{\partial^2 \varphi}{\partial y^2} + \frac{\partial^2 \varphi}{\partial z^2} = f'' \circ F \cdot \left(\overrightarrow{\text{grad}}\, F\right)^2 + f' \circ F \cdot \Delta F \tag{A.4}$$

Finally, a function $f$ for the potential distribution would be suitable if and only if:

$$\Delta \varphi(x,y,z) = f''(C) \cdot \left(\overrightarrow{\text{grad}}\, F(x,y,z)\right)^2 + f'(C) \cdot \Delta F(x,y,z) = 0 \tag{A.5}$$

Since the surfaces are regular, $\overrightarrow{\text{grad}}\, F$ is never null. The previous equation implies $f'$ cannot take a value equal to zero either. Therefore, the Laplacian equation is satisfied if and only if:

$$\frac{\Delta F}{\left(\overrightarrow{\text{grad}}\, F\right)^2} = -\frac{f''(C)}{f'(C)} \tag{A.6}$$

If the set of equations given by A.1 are equipotentials, then $\frac{\Delta F}{\left(\overrightarrow{\text{grad}}\, F\right)^2}$ is a function of $C$ only. Reciprocally, if the surfaces are equipotential and $\Phi(C) = -\frac{\Delta F}{\left(\overrightarrow{\text{grad}}\, F\right)^2}$ is a function of $C$ only, the function $f$ can be integrated on any path through the surfaces and:

$$f'(C) = A \exp^{\int \Phi} \tag{A.7}$$

$$f(C) = A \int \exp^{\int \Phi} + B \tag{A.8}$$

The constants $A$ and $B$ can be determined by fixing the boundaries of the integral for two values of $C$, and imposing the potential on the corresponding surfaces.

Equations A.1, A.2 and A.8 are very general conditions for surfaces and potential distributions so that the Laplacian equation be satisfied. In the following, such formal conditions are applied in order to exhibit surfaces that satisfy both the Laplacian equation and the border conditions of Holm's problem of a flat constriction.

## A.2 Semi-ellipsoids equipotentials

Smythe exhibits a set of semi-ellipsoid surfaces as candidates to be equipotentials, in a case of flat constriction as presented in Figure A.1. For a circular contact, these surfaces

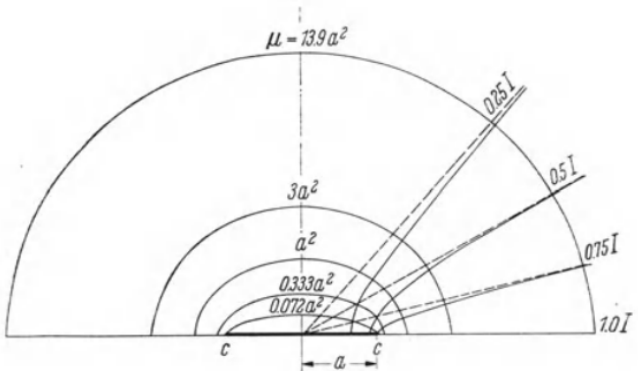


Figure A.1: Plot of the ellipsoids given by Equation A.9 for different values of $\mu$. Taken from [38].

are given by the set of equations A.9

$$\boxed{\frac{x^2}{a^2+\mu}+\frac{y^2}{a^2+\mu}+\frac{z^2}{\mu}=1} \tag{A.9}$$

where any value of the parameter $\mu$ defines a 3D surface of axis of symmetry $z$ in the semi-infinite space $z > 0$. Let's call such a surface $S_\mu$. The height of $S_\mu$ is $\sqrt{\mu}$, and the radius of its $z = 0$ section is $\sqrt{a^2+\mu}$. For a great value of $\mu$, neglecting $a$ in A.9 reduces $S_\mu$ to a sphere or radius $\sqrt{\mu}$. On the opposite, $\lim_{\mu\to 0} S_\mu = A_c$, the circular contact area at $z = 0$. Figure A.1 shows sections of the ellipsoids in the plane $y = 0$, for different values of the parameter $\mu$.

We now want to prove that the set of $S_\mu$ is a good candidate to represent equipotential surfaces, i.e. that they satisfy the condition given by Equation A.6. The main steps are clearly given by Smythe [88] and presented here.

First, we consider the domain of the space situated above the contact, in the $z > 0$ region, swept by the set of $S_\mu$ while $\mu > 0$. Equation A.9 can be rewritten as:

$$\mu^2 + (a^2 - x^2 - y^2 - z^2)\mu - a^2z^2 = 0 \tag{A.10}$$

The discriminant of this polynomial equation of order 2 is strictly positive for any point of the $z > 0$ region, so there is a unique solution $\mu$. Therefore there exists a function $F$ so that

$$\boxed{F(x, y, z) = \mu} \tag{A.11}$$

For the following, the parameter $\mu$ will be abusively confused with the function $F$ in order to simplify the writing of the partial derivatives. Let us define

$$M_n = \frac{x^2}{(a^2+\mu)^n}+\frac{y^2}{(a^2+\mu)^n}+\frac{z^2}{\mu^n} \tag{A.12}$$

and

$$N = \frac{1}{a^2+\mu} + \frac{1}{a^2+\mu} + \frac{1}{\mu} \tag{A.13}$$

With these notations, Equation A.9 becomes $M_1 = 1$ and differentiating it we find

$$\frac{2x}{a^2+\mu} - M_2 \cdot \frac{\partial \mu}{\partial x} = 0, \text{ etc.} \qquad \frac{\partial \mu}{\partial x} = \frac{2x}{M_2\left(a^2+\mu\right)}, \text{ etc.} \tag{A.14}$$

so

$$\boxed{\left(\overrightarrow{\text{grad}}\,\mu\right)^2 = \left(\frac{\partial \mu}{\partial x}\right)^2 + \left(\frac{\partial \mu}{\partial y}\right)^2 + \left(\frac{\partial \mu}{\partial z}\right)^2 = \frac{4M_2}{M_2^2} = 4M_2} \tag{A.15}$$

Differentiating again gives:

$$\frac{\partial^2 \mu}{\partial x^2} = \frac{2}{M_2\left(a^2+\mu\right)} - \frac{2x}{M_2\left(a^2+\mu\right)^2}\frac{\partial \mu}{\partial x} - \frac{2x}{\left(a^2+\mu\right)}\frac{1}{M_2^2}\left[\frac{2x}{\left(a^2+\mu\right)^2} - 2M_3\frac{\partial \mu}{\partial x}\right] \tag{A.16}$$

and using A.14:

$$\frac{\partial^2 \mu}{\partial x^2} = \frac{2}{M_2\left(a^2+\mu\right)} - \frac{8x^2}{M_2^2\left(a^2+\mu\right)^3} + \frac{8x^2}{M_3\left(a^2+\mu\right)^2 M_2^3}, \text{ etc.} \tag{A.17}$$

Summing the expressions for $x$, $y$, and $z$ gives:

$$\boxed{\Delta\,\mu = \frac{2N}{M_2} - \frac{8M_3}{M_2^2} + \frac{8M_2M_3}{M_2^3} = \frac{2N}{M_2}} \tag{A.18}$$

We can finally evaluate the ratio

$$\boxed{\frac{\Delta\,\mu}{\left(\overrightarrow{\text{grad}}\,\mu\right)^2} = \frac{N}{2}} \tag{A.19}$$

Equivalently to Equation A.6, this ratio is found to be a function of $\mu$ only, noting

$$\Phi\left(\mu\right) = -\frac{1}{2}\left(\frac{2}{a^2+\mu} + \frac{1}{\mu}\right) \tag{A.20}$$

This proves that such surfaces can be equipotential surfaces that satisfy the Laplacian equation. Besides, we have:

$$\exp^{\int \Phi(\mu)} = \exp^{-\frac{1}{2}\left[2\ln\left(a^2+\mu\right)+\ln(\mu)\right]} = \left(a^2+\mu\right)^{-1}\mu^{-1/2} \tag{A.21}$$

And, according to Equation A.8, the potential is then given by:

$$\varphi\left(\mu\right) = A\int_{\mu_0}^{\mu}\left(a^2+\theta\right)^{-1}\theta^{-1/2}\mathrm{d}\theta + B \tag{A.22}$$

where the constants $A$ and $B$ are determined with the boundary conditions.

## A.3 Current density on the constriction

The aim is now the determine the constants $A$ and $B$ as well as the total current going through the circular contact at $z = 0$. For reasons of symmetry, the potential is taken null on the contact area, so

$$\varphi(\mu) = A \int_0^{\mu} \left(a^2 + \theta\right)^{-1} \theta^{-1/2} \mathrm{d}\theta \tag{A.23}$$

Rather than imposing the potential on a second boundary surface, we would like to express $A$ as a function of the current going through the constriction. Using Ohm's law, A.7, A.14 and A.21, the $z$ component of this current is equal to:

$$j_z(x, y, 0) = -\lim_{z\to 0} \sigma \frac{\partial \varphi}{\partial z} = -\lim_{z\to 0} \sigma \frac{\partial \varphi}{\partial \mu} \cdot \frac{\partial \mu}{\partial z} = -\lim_{z\to 0} \frac{\sigma A}{(a^2+\mu)\sqrt{\mu}} \cdot \frac{2z}{M_2 \mu} \tag{A.24}$$

Substituting $M_2$ and then using the semi-ellipsoids equation to replace $\frac{z^2}{\mu}$ and $\frac{z}{\sqrt{\mu}}$ leads to

$$j_z(x, y, 0) = -\lim_{z\to 0} \frac{2\sigma A}{(a^2+\mu)} \cdot \frac{z}{\sqrt{\mu}} \cdot \frac{1}{\frac{(x^2+y^2)\mu}{(a^2+\mu)^2} + \frac{z^2}{\mu}} = -\lim_{z\to 0} \frac{2\sigma A}{(a^2+\mu)} \cdot \frac{\sqrt{1 - \frac{x^2+y^2}{a^2+\mu}}}{\frac{(x^2+y^2)\mu}{(a^2+\mu)^2} + 1 - \frac{x^2+y^2}{a^2+\mu}} \tag{A.25}$$

The equation of the semi-ellipsoids A.9 implies that $\lim_{z\to 0} \mu = 0$. So neglecting $\mu$ in front of $a$ near $z = 0$, and since we have $x^2 + y^2 < a^2 + \mu$

$$j_z(x, y, 0) = -\frac{2\sigma A}{a^2} \cdot \frac{1}{\sqrt{1 - \frac{x^2+y^2}{a^2}}} \tag{A.26}$$

Finally, the expression of the current density on the contact can be integrated to express the total currant as a function of the constant $A$

$$I = \iint_{A_c} j_z(x, y, 0) \mathrm{d}x\mathrm{d}y = \frac{2\sigma A}{a^2} \cdot \iint_{\substack{0<\theta<2\pi \\ 0<r<a}} \frac{r \mathrm{d}r\mathrm{d}\theta}{\sqrt{1 - \frac{r^2}{a^2}}} = \frac{2\sigma A}{a^2} \cdot 2\pi a^2 = 4\pi\sigma A \tag{A.27}$$

## A.4 Holm's formula

The calculations developed in the previous section show that for a given size of the contact $a$, and if the semi-ellipsoids are considered equipotential, then the current density through

the spot is a function of the distance to the axis:

$$j(r) = \frac{I}{2\pi a^2} \cdot \frac{1}{\sqrt{1 - \frac{r^2}{a^2}}} \tag{A.28}$$

and Equation A.23 can be rewritten as

$$\varphi(\mu) = \frac{I}{4\pi\sigma} \int_0^{\mu} \frac{\mathrm{d}\theta}{(a^2 + \theta)\sqrt{\theta}} \tag{A.29}$$

The resistance $R_\mu$ of conductor delimited by the lower boundary $A_c$ and the upper boundary $S_\mu$ is given by the ratio between the potential drop and the total current $I$.

$$R_\mu = \frac{I}{4\pi\sigma} \int_0^{\mu} \frac{\mathrm{d}\theta}{(a^2 + \theta)\sqrt{\theta}} = \frac{I}{2\pi\sigma} \int_0^{\sqrt{z}} \frac{\mathrm{d}z}{(a^2 + z^2)} = \frac{I}{2\pi\sigma} \arctan \frac{\sqrt{\mu}}{a} \tag{A.30}$$

We can now observe that the value of $R_\mu$ converges to a finite value $R_\infty$ when $\mu$ increases, and that this value is only a function of the radius of the spot $a$ and of the conductivity. On Figure A.1, the ellipsoids have been chosen so that the resistance between two consecutive equipotentials be 1/6 of $R_\infty$. We can deduce that when a current is imposed through such a spot, the voltage drop is mostly concentrated near the contact. From a distance of 20 times the radius of $A_c$, the resistance observed is already 96.8 % of $R_\infty$.

The very famous Holm's Equation is found by considering two times $R_\infty$, that is

$$R_\mathrm{c} = \frac{1}{2a\sigma} \tag{A.31}$$

To conclude, is is important to keep in mind that this formula is valid if the contact area can be seen from far enough. Holm's resistance is in fact reflecting a limitation to the admitted current, if a potential drop is imposed between the constriction section and another surface surrounding it. From far enough, it does not matter if the potential is imposed on a semi-ellipsoid surface or on another surface, but this surface needs to close the domain.

# Appendix B

# Résumé en Français

Un avion de ligne est statistiquement touché par la foudre une fois toutes les 1500 heures de vol, soit environ une fois par an. La foudre peut représenter une menace pour les systèmes et l'intégrité des aéronefs, soit par le biais d'effets indirects comme des interférences électromagnétiques avec les systèmes électriques de l'avion, soit par ses effets directs sur les structures aéronautiques, telles que les contraintes thermo-mécaniques induites par le passage de forts courants, .

Les effets directs impliquent notamment pour les avionneurs tout un processus de certification des assemblages aéronautiques à la fois long et coûteux. Ceux-ci sont testés expérimentalement sur des bancs d'essai, capables de reproduire des ondes de courant normatives représentatives du risque foudre. Un enjeu majeur de l'unité FPA est de proposer des modèles ayant le double objectif d'améliorer les connaissances fondamentales sur la réaction des assemblages soumis à la foudre, mais aussi de guider les avionneurs dans leur démarche de certification.

## Contacts soumis à de forts courants et risque de décharge

Les contacts mécaniques dans les assemblages aéronautiques se comportent comme des résistances électriques au passage du courant, pouvant induire toute une phénoménologie de décharges électriques encore mal comprises, et particulièrement contraignantes dans les zones carburant. Ces résistances sont la conséquence de l'état de surface des pièces en contact, le courant étant contraint de passer à travers des petits ponts conducteurs microscopiques, appelés “a-spots", comme représentés sur la Figure B.1. Il est observé en pratique que ces résistances peuvent varier de plusieurs ordres de grandeur en quelques micro-secondes pendant le passage d'un fort courant, mais ce phénomène est mal compris.

Ces variations rapides des résistances de contact à fort courants sont pourtant cruciales car elles pilotent les distributions de courant dans les assemblages foudroyés, ainsi que l'énergie dissipée par effet Joule et l'amplitude des champs électriques pouvant être atteints. Le but de la thèse est de développer une modélisation d'un tel contact et de sa

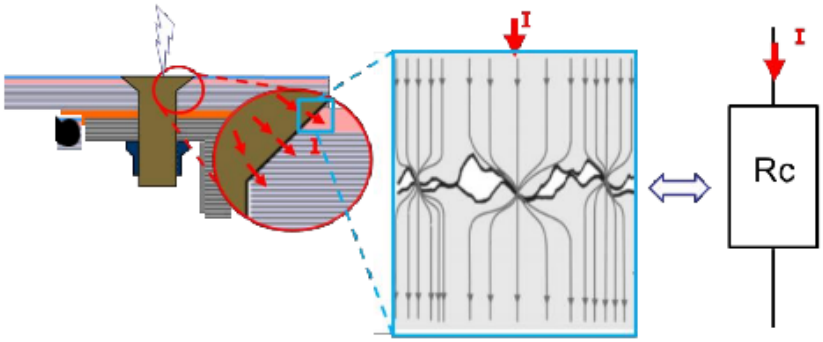


Figure B.1: Résistance éléctrique de contact entre deux conducteurs

réaction au passage d'un courant de type foudre. La difficulté réside aussi bien dans la modélisation géométrique de l'état de surface, que dans le fort couplage multi-physique du problème : distribution du potentiel électrique, chauffage par effet Joule, vaporisation du métal conducteur, écrasement mécanique et formation de décharges plasma.

## Plan du manuscrit

Le premier chapitre présente le contexte du problème. La physique de l'initiation de la foudre et l'attachement du canal sur l'avion sont présentés brièvement. Les ondes de courant normalisées, servant de majoration de l'effet du passage de courants de type foudre sur les différentes zones d'un aéronef, sont introduites, notamment l'onde D qui sera le profil de courant type utilisé dans les simulations numériques des chapitres suivants. L'accent est mis sur le risque de décharges au niveau des assemblages aéronautiques soumis à de forts courants. Ces phénomènes sont très bien observés sur des bancs expérimentaux reproduisant les ondes de courant de foudre, mais sont encore mal compris. La dernière partie de ce premier chapitre présente la terminologie et la bibliographie concernant les contacts électriques, qui sont le cœur du sujet. Les limites des modèles existants justifient le besoin de développer un nouveau modèle multi-physique, afin de répondre aux questions soulevées par le comportement d'assemblages soumis à des courants de type foudre.

Dans le deuxième chapitre, le choix est fait de se concentrer sur un modèle de contact à un seul a-spot. Le choix est fait de modéliser un tel a-spot par un canal de contact cylindrique, entre deux conducteurs, par ailleurs séparés par un gap d'air supposé isolant. Un modèle en volumes finis 2D axisymétrique est développé, prenant pour axe de symétrie l'axe du cylindre. En électrostatique, imposer le potentiel aux bornes des conducteurs et calculer le courant induit passant d'un conducteur à l'autre, par l'intermédiaire du a-spot, permet de déduire la résistance électrique de ce contact. Un très bon accord est trouvé entre les résultats de ces simulations et des valeurs analytiques obtenues dans la littérature. On remarque également que le courant se concentre principalement en périphérie du cylindre.

Ce modèle en volumes finis est ensuite enrichi par des considérations thermiques : avec l'effet Joule induit par le passage du courant, le métal chauffe, sa conductivité diminuant jusqu'à atteindre les points de fusion et de vaporisation. Le métal vaporisé est considéré comme isolant dans ce modèle, ce qui correspond à supposer qu'il est immédiatement évacué hors du contact. Puisque le courant est originellement concentré en périphérie du a-spot, c'est en périphérie que le métal chauffe en premier. Par une redistribution du courant due à la diminution de conductivité, cet effet est homogénéisé, et la cylindre monte presque uniformément en température jusqu'à atteindre le seuil de vaporisation. Dès cette température atteinte, la vaporisation complète se fait rapidement, de la périphérie vers le centre. Il y a donc un fort couplage thermo-électrique, une diminution de la conductivité du cylindre puis une diminution de son rayon effectif, ce qui conduit à une augmentation de la résistance de ce contact.

Cette modélisation apporte des informations intéressantes concernant l'évolution possible d'un contact soumis à une onde D, mais est bien trop coûteuse en calcul pour envisager l'étude d'un contact plus réaliste fait de milliers d'aspérités et de a-spots. Pour cette raison, un modèle simplifié a été développé, appelé "modèle 0D", ayant comme paramètres la hauteur $l$ du cylindre et son rayon $a$, pouvant varier dans le temps, ainsi que sa température $T$, supposée homogène, et les propriétés du métal correspondantes. Les observations apportées par le modèle en volumes finis servent alors d'hypothèses pour ce modèle simplifié, afin de calculer l'effet Joule dissipé dans le a-spot et se répartition. Cette simplification permet de reproduire très fidèlement les résultats observés avec le modèles en volumes finis, mais avec un coût en calcul bien plus faible.

En outre la considération des aspects mécaniques, composante importance du problème, a pu être implémentée dans ce modèle 0D. En imposant une force d'écrasement sur le contact, le cylindre doit être compressé jusqu'à ce que la force de réaction mécanique soit opposée à la force imposée. Alors, la résistance initiale d'un contact diminue avec la force, puisque la longueur du a-spot diminue et sa longueur augmente. Cette réaction élasto-plastique se révèle encore plus importante lorsqu'elle est couplée à l'évolution thermique du métal : plus il chauffe, plus il devient ductile, et plus le contact s'écrase. L'augmentation de la résistance est donc largement freinée par ce phénomène lorsqu'une force d'écrasement constante est imposée sur le contact pendant le passage d'une onde D. En fait, le métal n'atteint plus sa température de vaporisation dans les cas observés, et la résistance passe par un pic avant de décroître.

Le troisième chapitre est un chapitre de transition, qui a pour but d'élargir le champs d'application du modèle précédent au cas d'un contact formés par de nombreux a-spots en parallèle. Deux types d'interactions entre a-spots sont étudiés.

Le premier est une interaction électrique : lorsque des a-spots en parallèles sont suffisamment proches, les lignes de courants ne se répartissent par entre eux de la même manière que s'ils étaient suffisamment isolés. Pour une même différence de potentiel

entre les bornes du contact, le courant le traversant est plus faible lorsque les a-spots sont proches. De plus, la symétrie axiale est dans ce cas perdue en ce qui concerne la distribution du courant dans chaque a-spot cylindrique. Le choix est alors fait, et justifié, de négliger cette interaction en supposant que les a-spots sont toujours suffisamment éloignées les uns des autres pour pouvoir faire cette approximation.

Le deuxième type d'interaction est un effet de groupe qui peut s'observer dans le comportement mécanique du contact. Si l'on impose une force d'écrasement, l'équilibre mécanique n'est plus assuré par un seul a-spot, mais la somme des réactions elasto-plastique doit être opposée à l'écrasement. Alors, augmenter cette force permet d'atteindre des aspérités plus petites qui ne participaient pas au contact pour une force plus faible, et donc d'augmenter le nombre de a-spots tout en diminuant la résistance globale du contact. De façon similaire, maintenir une force constante pendant le passage d'une onde D permet de faire apparaître de nouveaux a-spots lorsque les propriétés mécaniques de ceux qui soutenaient initialement la force chutent.

Le quatrième chapitre utilise le modèle précédent, à fort couplage multiphysique et adapté à un contact ayant de nombreuses aspérités, pour étudier le comportement de contacts plus réalistes. Dans la réalité, en effet, le nombre, la géométrie et la taille des aspérités sont aléatoires. Des outils statistiques peuvent cependant être utilisés pour caractériser l'état d'une surfaces, qui sont un résultat des matériaux concernés, de la formation et de l'historique de cette surface. Les paramètres de rugosité, tels que la moyenne de la variation de la hauteur d'une surface autour d'une hauteur moyenne, ou l'écart type de ces variations, peuvent être mesurés par profilométrie. Dans ce chapitre, ces paramètres de surface ont été pris de la littérature ([40]) et utilisé pour générer des distributions aléatoires d'aspérités. Ces aspérités sont toujours supposées cylindriques, mais leur nombre est fixé pour une unité de surface et leur hauteur suit une loi Gaussienne dont la moyenne et l'écart type sont les deux paramètres.

La réaction d'un tel contact à une onde D est très proche de celle observée dans les chapitres précédents. Sans force de serrage, le nombre de a-spots est fixé, et ceux-ci augmentent en température presque uniformément jusqu'à vaporisation. La résistance du contact augmente, puis diverge lorsque la vaporisation devient totale. Avec une force de serrage imposée constante, au contraire, la vaporisation ne se fait jamais. Dès que les a-spots soutenant la force mécanique deviennent ductiles, ils sont écrasés jusqu'à ce que de nouveaux a-spots se forment. La résistance augmente initialement par une baisse de la conductivité des premiers a-spots, atteint un pic, puis diminue par effet d'écrasement.

Puisque de nombreuses aspérités entrent en jeux, jusqu'à plusieurs milliers, ces variations de la résistance sont beaucoup plus lissés que dans le cas d'un contact formé par deux aspérités. Alors, l'effet des paramètres de rugosité est étudié. Il est montré en particulier que pour une même résistance initiale, un contact peut avoir un comportement différent, bien que similaire, en fonction de son état de surface.

Le dernier chapitre propose un modèle d'expansion du métal vaporisé en périphérie d'un a-spot. Les contacts étudiés et soumis à une onde D le sont à distance de serrage constante, et non à force de serrage constante, puisqu'il a été observé que dans ce cas le métal ne vaporise jamais. L'accent a été mis sur le cas d'un modèle de contact à un seul a-spot afin d'exhiber la dynamique possible de redistribution du courant dans un canal de plasma. L'hypothèse que ce plasma avait une conductivité négligeable avait été faite dans les premiers chapitres, mais celui-ci permet d'avoir une approche plus réaliste.

La symétrie axiale est conservée, l'hypothèse étant faite que le métal vaporisé se propage radialement. Il se détend en conservant l'équilibre avec une pression extérieure de confinement, sauf lorsque la propagation est limitée par la vitesse du son dans le plasma. Les propriétés du plasma (conductivité électrique, vitesse du son, pression) sont calculées grâce à un modèle QEOS, en fonction de l'énergie interne et de la densité. Un bilan d'énergie interne est effectué en prenant en compte l'énergie dissipée par effet Joule, le travail de la force de pression de confinement, l'énergie cinétique du plasma, et le débit de masse vaporisée par le a-spot solide.

Ce modèle permet d'observer une redistribution du courant du a-spot solide vers le plasma. Les premiers instants de la simulation, tant qu'il n'y a aucune vaporisation, sont strictement similaires à ceux observés au Chapitre 2 : le métal chauffe, sa conductivité diminue et la résistance augmente. Cette fois en revanche, la résistance ne diverge plus lorsque la vaporisation démarre. Elle continue d'augmenter tant que le a-spot n'est pas complètement vaporisé, mais diminue ensuite fortement lorsque le courant passe intégralement par le plasma et que celui-ci chauffe et devient plus conducteur.

Un critère utile pour estimer l'importance d'une décharge, et le risque qu'elle représente dans un assemblage aéronautique, est celui de l'énergie totale dissipée par effet Joule dans le plasma formé par vaporisation. Le modèle permet de calculer cette énergie, pour une géométrie donnée d'un a-spot (cylindrique, et tel que sa longueur est égale à son diamètre), et pour des résistances initiales du contact différentes. On pourrait s'attendre à ce que l'énergie dissipée pendant le passage d'une onde D augmente lorsque la résistance initiale augmente, mais le résultat n'est pas si trivial. Celle-ci passe par un maximum. En effet, pour une résistance initiale trop faible, il n'y a pas ou peu de vaporisation car le a-spot est trop gros. A l'inverse, s'il est trop petit, il est vaporisé plus tôt, et puisque la montée du plasma en température fait décroître la résistance du contact, l'ensemble chauffe globalement moins sur la durée d'une onde D.

# Conclusion

Un modèle multiphysique de contacts électriques soumis à de forts courants à été développé. Étant donnée la complexité du problème, de nombreuses hypothèses ont été faites, et le modèle proposé peut être amélioré. Il a cependant permis de mettre en évidence

des comportements possibles, attendus ou au contraire contre-intuitifs, et de répondre à des questions posées par les observations expérimentales. De nombreuses questions restent néanmoins en suspens, et ce travail aura notamment permis de définir les contours d'expériences qui devraient être réalisées sur un banc expérimental pour confirmer ou infirmer certaines interprétations de ce modèle.

**Titre :** Contacts électriques soumis à de forts courant : processus fondamentaux et application à l'interaction entre la foudre et des structures aéronautiques.

**Mots clés :** Plasma, foudre, décharge, contact électrique, simulation numérique

**Résumé :** La foudre est un phénomène naturel aléatoire impactant un avion de transport civil en moyenne une fois toutes les 1500 heures de vol. Les courants forts et impulsionnels pouvant parcourir la structure d'un aéronef peuvent induire des contraintes physiques aux conséquences sérieuses en ce qui concerne la sûreté. En particulier, quand un assemblage est parcouru par un courant de type foudre, des champs électriques ainsi que des densités d'effet Joule importants peuvent engendrer différents phénomènes de décharge. Le risque d'étincelage est particulièrement critique au niveau des réservoirs de carburant, et différentes technologies de protection et procédures de certification sont employées pour maîtriser ce risque. Les résultats expérimentaux laissent penser que la formation de ces décharges est due aux résistances électriques localisées aux interfaces entre les différentes pièces des assemblages. Le but de cette thèse a été de modéliser les phénomènes qui se produisent à une échelle microscopique au niveau de telles résistances de contact soumises à de forts courants impulsionnels de type foudre.

**Title :** Electric contacts subject to high current: Fundamental processes and application to the interaction between lightning and aeronautical structures

**Keywords :** Plasma, lightning, discharge, electrical contact, numerical simulation

**Abstract :** Lightning is a natural hazardous event that strikes a civil aircraft on average once per 1500 hours of flight. The corresponding high and impulsive currents that may flow along the structure of the aircraft can generate physical constraints with major consequences regarding safety. In particular, when a fastened assembly is crossed by a lightning current, important electric fields and Joule power densities may give birth to a variety of discharge phenomena. The sparking risk is particularly critical in fuel tanks, and different lightning protection technologies and certification procedures are employed to face it. The ignition of discharges is believed to be mostly due to the local electrical resistance at the interfaces between the parts of the assemblies. The aim of this thesis was to model to phenomena that occur at a microscopic scale of such contact resistances subject to high and impulsive currents.